HEPL-246

Copy No. 181

PHOTOPROTONS FROM OXYGEN, FLUORINE, NEON, AND OTHER LIGHT ELEMENTS

By
William R. Dodge

Technical Report
Linear Electron Accelerator Project
Contract N6onr-25116

HEPL Report No. 246
October 1961

High-Energy Physics Laboratory
W. W. Hansen Laboratories of Physics
Stanford University
Stanford, California

HEPL-246

PHOTOPROTONS FROM OXYGEN, FLUORINE, NEON, AND OTHER LIGHT ELEMENTS

By

William R. Dodge

Technical Report
Linear Electron Accelerator Project
Contract N6onr-25116

HEPL Report No. 246
October 1961

High-Energy Physics Laboratory
W. W. HANSEN LABORATORIES OF PHYSICS
Stanford University
Stanford, California

An account of the research reported here was submitted to the Department of Physics and the Committee on Graduate Study of Stanford University in partial fulfillment of the requirements for the degree of Doctor of Philosophy.

ABSTRACT

The (γ,p) reaction in O, F, Ne, and C has been studied with electrons of energies up to 36 Mev. Survey studies were made of the Al, A, and B (γ,p) energy spectra. The reactions were initiated by electrons, and not real photons; but it has been theoretically predicted and received partial experimental verification that there is a one to one correspondence between electron- and photon-induced reactions, and that one can assume, when analyzing electron-production yields, that the electron has associated with it a virtual-photon spectrum, similar to the real-photon bremsstrahlung spectrum. The virtual and bremsstrahlung spectra differ, however, in that the virtual-photon spectrum depends on the multipolarity of the induced transition and the angle between the incident electron beam and the emitted disintegration product, while the bremsstrahlung spectrum does not. The electron production yields were analyzed with the use of the E-1 virtual-photon spectrum to obtain $\sigma(\gamma,p)$. The proton yields and corresponding cross sections of O, F, and Ne contain more than two peaks or resonances. Neon exhibits the most interesting spectrum. It has a series of well-resolved, evenly-spaced peaks whose envelope has the usual giant-resonance shape. The peaks occur at laboratory proton energies of 3.20, 3.70, 4.58, 5.80, 6.65, 7.75, 8.65, 9.40, and 11.40 Mev. The final-state properties of the Ne protons from 4 to 10 Mev and the O protons from 9.2 to 12.4 Mev were determined to within 20% by excitation experiments. Angular distribution measurements over a considerable region of the giant resonances are presented for O, F, Ne, and C. The following integrated cross-section

estimates and limits were obtained:

$O^{16} \int_{16.6}^{27} \sigma(\gamma,p)dE_\gamma = 56 \pm 11$ Mev-mb; $F^{19} \int_{10.5}^{23} \sigma(\gamma,p)dE_\gamma = 29^{+9}_{-3}$ Mev-mb;

$Ne \int_{16}^{27} \sigma(\gamma,p)dE_\gamma = 65^{+13}_{-10}$ Mev-mb; $C^{12} \int_{20.3}^{29.3} \sigma(\gamma,p)dE_\gamma = 50 \pm 8$ Mev-mb;

$Al^{27} \int_{18.5}^{29} \sigma(\gamma,p)dE_\gamma = 94 \pm 19$ Mev-mb; 62 Mev-mb $\leq A^{40} \int \sigma(\gamma,p)dE_\gamma \leq 100$ Mev-mb;

and

$$25 \text{ Mev-mb} \leq B \int_{13.8}^{27} \sigma(\gamma,p)dE_\gamma \leq 42 \text{ Mev-mb}.$$

ACKNOWLEDGMENTS

The author wishes to express his appreciation and indebtedness to Professor W. C. Barber for his help, encouragement, and catalytic, incisive criticism.

Many other people made contributions to this work. Foremost among those who made important technical contributions was William Ewing of the High-Energy Physics Laboratory Tube Shop, who skillfully fabricated the gas target chambers and faithfully repaired the Mark II Linac electron guns. Edward Pathaway, research machinist, also made sizable contributions.

CONTENTS

LIST OF TABLES

APPENDIX II.

LIST OF FIGURES

CHAPTER I

INTRODUCTION

It is generally conceded that the mechanism of photonuclear reactions is essentially understood, yet a number of important facets of these reactions still await experimental confirmation and quantitative theoretical explanation. Among the unexplained facets is the "contentious" subject[1] of gross structure in the giant resonance in light nuclei, as conjectured from the γ-nucleon cross sections. This subject is nontrivial since the occurrence of gross structure other than that attributable to a deformation of the nuclear shape from sphericity, as evidenced by large quadrupole moments, is embarrassing to the collective models of the nuclear photoeffect; while the independent-particle models contain an inherent mechanism for the production of structure.[2] While, in general, the two models have mutually exclusive domains of validity, regions do exist where both models claim applicability. As Spicer[3] has pointed out, since the properties of the low-lying states of elements in the region of $9 < Z < 30$ are successfully described by the collective or strong interaction models, the Danos-Okamoto long-range correlation model[4] of the photonuclear effect must be applicable to these elements. If the collective model description is correct in this region, the giant resonance should be split into two peaks occurring at photon energies ω_a and ω_b whose ratio is given by $\omega_a/\omega_b = .911(a/b) + .089$, where the ratio a/b (a and b are the lengths of the semi-major and semi-minor axis of the assumed spheroidally shaped nucleus) can be determined

from the intrinsic quadrupole moment. In particular, using values for the intrinsic quadrupole moments derived from low-lying E-2 transitions,[5] the collective model predicts ω_a/ω_b values of 1.3 and 1.4 for F and Ne, respectively; hence the predicted giant-resonance splitting should be easily resolved. On the other hand, recent theoretical studies show that Wilkinson's theory[6] of the photonuclear effect with detailed shell-model initial and excited states[7,8] can well parody the gross structure previously seen in the O $\sigma(\gamma,p)$. Furthermore, although detailed photonuclear calculations have not been made for F and Ne, the excited states of F^{19} have been calculated with the shell model using configuration mixing.[9] These elements should clearly be within the domain of the shell model.[10] Thus both models claim to be applicable to the photonuclear effect in F and Ne. Therefore the occurrence of more than two or, if the improbable assumption of non-axial nuclear symmetry[11] is made, three relatively large peaks in $\sigma(\gamma,p)$ would confirm the independent-particle-model description of the nuclear photoeffect while providing a severe censure of the collective-model description. Noncommittal results might give some insight into the coupling mechanism between the single-particle states and collective-model states in the nuclear-model transition region. However, except for the O $\sigma(\gamma,p)$, experimental evidence for the gross (γ,p) energy structure has been statistically inconclusive.[12,13,14,15]

Consequently, a search for (γ,p) energy structure with which the predictions of the collective and independent particle models could be compared was made in O, F, and Ne. In addition, survey searches were

made for (γ,p) energy structure in A and B; and a C energy spectrum, needed in the CF_2 target F experiments for C background subtraction, was obtained. Angular distributions of the protons from the prominent peaks in O, F, Ne, and C were measured. The relationship between photon and proton energy was determined for the major O and Ne peaks by excitation of the protons as a function of electron energy. All target elements contained the naturally occurring ratios of isotopes.

In these experiments the direct effect of the electron's transition electromagnetic field produced the reaction and not real photons. However, a direct correspondence between electron- and photon-induced reactions has been predicted by calculations that employ the Møller potential[16,17] to describe the electron's transition electromagnetic field. According to virtual-photon theory, the direct effect of the electron's transition field may be considered as spectra of virtual photons which depend on the multipolarity of the induced reaction. The electron-production yields may be analyzed with these virtual-photon spectra in analogy to the analysis of photoproduction yields with a real bremsstrahlung spectrum. The virtual photon hypothesis and spectra have received partial experimental confirmation.[18,19] Therefore, we describe the electron production process as a (γ,p) reaction even though the square of the four-vector momentum transferred to the nucleus may be different than zero, as in the real-photon case. Furthermore, since the three-momentum transfer may be in other than incident-beam directions, although nearly forward directions predominate, the virtual-photon spectra are expected to have a slight dependence on the angle between the emitted

disintegration product and the primary electron beam; and consequently, electron-induced angular disintegrations are expected to be slightly more isotropic than real-photon-induced reactions. This effect for E-1 transitions has been examined theoretically by Bosco and Fubini.[20] They assume explicitly the classical E-1 approximation ($kR \ll 1$, where k is subsequently defined and R is the radius of the interaction region) and implicitly the equality of the matrix elements of the current operator between initial nuclear and final nuclear-nucleon states which are perpendicular and parallel to the three-vector momentum transfer. Their result, which contained several printing errors, was not integrated over the scattered electron directions. They showed essentially that the E-1 differential electron disintegration cross section is given by

$$\frac{d^2\sigma}{d\Omega_q d\Omega_{e'}} = \frac{2\pi}{v_e} \rho_{e'} \rho_q \left[\frac{1}{2} \alpha(E) N_{ii} + \frac{\beta(E)}{q^2} N_{ij} q_i q_j \right] , \qquad (1)$$

if the E-1 photodisintegration cross sections is given by

$$\frac{d\sigma_{ph}}{d\Omega_q} = \frac{2\pi}{c} \rho_q \left[\alpha(E) + \beta(E) \sin^2 \theta_q \right] , \qquad (2)$$

where

$$N_{ij} = \frac{e^2}{2m^2(k_0^2 - \vec{k}^2)^2} \left\{ 2p_i p_j + \frac{1}{2}(\vec{k}^2 - k_0^2)\delta_{ij} + (k_i k_j - p_i k_j - p_j k_i) \left(1 - \frac{\vec{k}^2}{k_0^2} + \frac{2\vec{p}\cdot\vec{k}}{k_0^2} \right) + \right.$$

$$+ \frac{k_i k_j}{k_0^2} [2(\vec{p}\cdot\vec{k})^2 - 2\vec{k}^2(\vec{p}\cdot\vec{k}) + \frac{1}{2}(\vec{k}^2 - k_0^2)\vec{k}^2] \Bigg\} ,$$

and θ_q is the angle between the real-photon direction and the relative momentum of the emitted particle $\vec{q}$. This is equivalent to

$$\frac{d^2\sigma}{d\Omega_q d\Omega_{e'}} = \pi \frac{\rho_{e'}\ \rho_q}{v_e} \frac{e^2}{m^2 k_0^2} \left\{ \frac{1}{2}\alpha(E) \left[-\frac{1}{2} - \frac{\omega^2 + \omega'^2}{k_0^2 - \vec{k}^2} - \frac{2m^2 k_0^2}{(k_0^2 - \vec{k}^2)^2} \right] + \frac{\beta(E)}{q^2} \left[\frac{2[\omega'\vec{p} - \omega\vec{p}')\cdot q]^2}{(k_0^2 - \vec{k}^2)^2} + \frac{1}{2} \frac{(\vec{k}\cdot\vec{q})^2 - k_0^2 \vec{q}^2}{(k_0^2 - \vec{k}^2)} \right] \right\} , \qquad (3)$$

where $k_0 = \omega - \omega'$ is the energy and $\vec{k} = \vec{p} - \vec{p}'$ is the momentum transferred to the disintegrating system; the unprimed quantities refer to initial- and the primed quantities to final-state electron variables. Upon integration over scattered-electron directions, we obtain

$$\frac{d\sigma}{d\Omega_q} = \pi^2 \frac{e^2}{m^2 k_0^2} \frac{\rho_{e'}\ \rho_q}{v_e} \left[\left(\frac{\omega^2 + \omega'^2}{\omega\omega'} \lambda - 2 \right) \alpha(E) + \frac{\omega'}{\omega} \beta(E) + \left(\frac{\omega^2 + \omega'^2}{\omega\omega'} \lambda - 2 - \frac{3}{2}\frac{\omega'}{\omega} \right) \beta(E) \sin^2 \theta_q \right], \qquad (4)$$

where

$$\lambda = \ln \frac{\omega\omega' + pp' - m^2}{m(\omega - \omega')} .$$

The electron-beam monitoring system, proton spectrometer, gaseous target-chamber, as well as other experimental details are discussed in Chapter II, Experimental Appartus and Methods. In Chapter III, Experimental Results and Discussions, the proton energy distributions,

excitation functions, and angular distributions are presented and compared with other experiments. In Chapter IV, Conclusions, the implications of the observed structure are discussed.

CHAPTER II

EXPERIMENTAL APPARATUS AND METHODS

A. Description of the Experimental Arrangement

Electrons, accelerated by the Stanford Mark II 49-Mev Linear Accelerator and momentum-analyzed into a momentum band of variable width by two 30° wedge magnets and a slit system located at the first horizontal spacial focus of the magnet system,[21] traversed only 0.00075 in. of Al, which constituted the three-foil, secondary-emission electron-beam-current monitor (SEM),[22] and a 0.001-in. Al window between the accelerator and spectrometer vacuum systems before entering the scattering chamber. The electrons were then incident on the target elements which were contained in a thin-walled stainless-steel cylinder, in the case of gaseous targets, or which were in the form of polystyrene (CH) or teflon (CF_2) foils, in the case of C or F. The protons emitted from the target into the solid angle subtended by the spectrometer were momentum-analyzed by an 18-in. radius, 120° double-focusing magnet and then detected by a counter system located in the focal surface of the magnet. The counter system consisted of eight channels, each with an RCA6810 photomultiplier tube with vacuum seal at the projecting metal ring on the tube base, which permitted the photocathode of the PMT and the 1.125 × 2 × .010 in. Pilot-B scintillators on which were evaporated approximately 10^{-5} in. of Al for optical isolation of the counters to be in the spectrometer vacuum system. Since it was experimentally

determined that the pulse-height distribution of the counter array was narrowest when the scintillator was approximately 0.06 in. from the photocathode with no light pipe between, this arrangement was used. The outputs of the tubes were fed directly to fast integral discriminators of the Moody type. The counter system resolving time was considerably shorter than the average time interval between background electron pulses, which eliminated, to a large degree, the pile-up of these small electron-induced pulses and allowed the maximum electron-beam intensity to be used. Calibration and design motivation for the various components are discussed in greater detail below.

B. Detailed Description of the Calibration and Performance of the Experimental Components

2.1 Energy calibration and stability of the primary electron beam. The currents through the achromatic beam-translation system[21] were monitored and not the fields themselves during most of the energy and angular distribution runs. Diurnal drifts in the field values, allegedly due to long relaxation times of the magnet iron domains, have been observed in this laboratory by other experimenters using similar magnets, even though the magnetizing currents were kept constant. These effects were minimized in this experiment by turning on all equipment at least half an hour before the start of data runs. Since each datum point consists, in general, of an average of information from three different counters taken at random times relative to daily data-run starting times, electron-energy errors are further minimized by the method of data

combination. Fortunately, the proton yield, for transitions initiated by photons whose energies are not near the virtual-photon endpoint, is not especially sensitive to fluctuations in electron energy. Figure 1 shows the relative change of the virtual-photon intensity as a function of the transition energy k for an initial electron energy $E_0 = 30$ Mev.

The current through the beam translation system was cycled in a standardized manner whenever the electron energy was decreased to minimize field and hence electron energy errors due to hysteresis. Power supply limitations did not permit high enough currents to saturate the magnets, but elastic electron scattering measurements showed that the recycling procedure used gave reproducible energies to within .2%.

The initial electron energy was calibrated both by (γ,n) threshold measurements,[23] and by Cm^{244} α-particle measurements (Fig. 2) with the use of the proton spectrometer and elastic electron scattering. The latter method involves extrapolating from the α-particle $H\rho$ values to electron $H\rho$ values, and assumes the field configurations are the same for both cases, differing only in magnitude. The threshold measurements gave $E_0 = 1.2\,X - 1.7$ and the α-particle and elastic electron scattering measurements gave $E_0 = 1.135\,X - 1.18$, where X is the analyzing-magnet-shunt voltage in millivolts. The proton endpoint for the 24.5-Mev C data seemed to indicate an E_0 midway between these values, after allowance was made for the finite energy spread of the initial electron beam. (More precise α-particle and field measurements support the latter value[24] of E_0.) Although the relationship $E_0 = 1.135\,X - 1.18$ was assumed in all cross-section calculations, the more correct electron

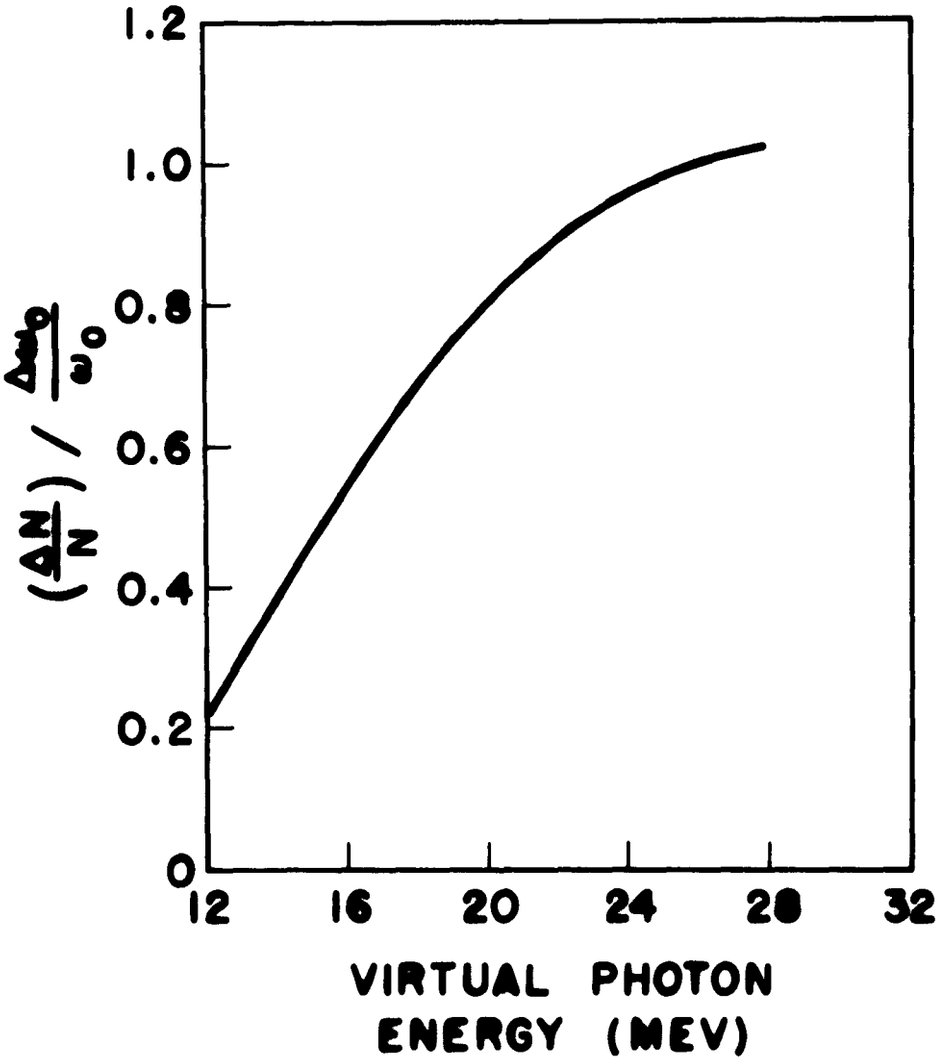

FIGURE 1

Ratio of the fractional change in the E-1 virtual-photon intensity spectrum to the fractional change in the primary electron electron energy as a function of the virtual-photon energy.

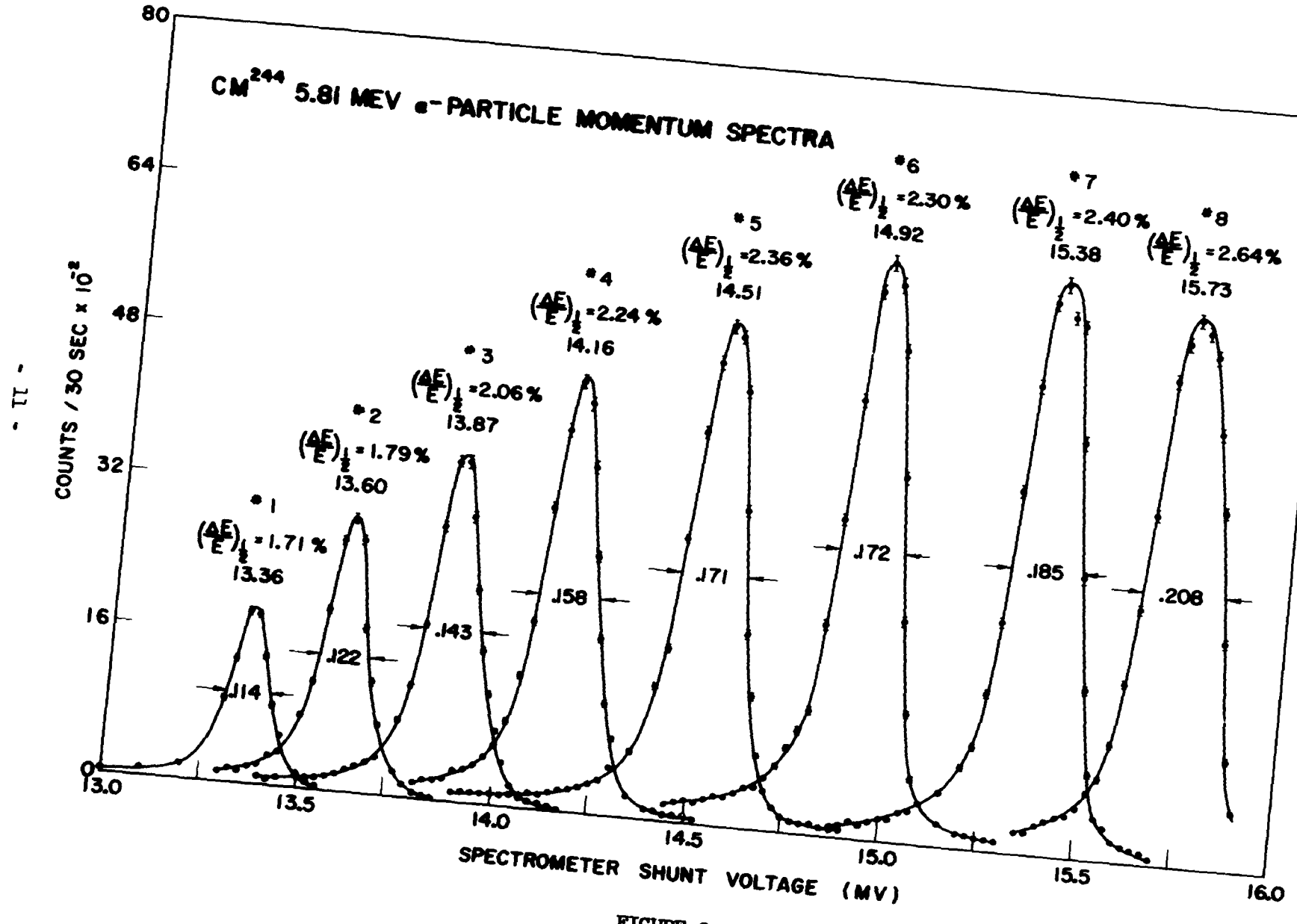
CM^244 5.81 MEV α-PARTICLE MOMENTUM SPECTRA
COUNTS / 30 SEC x 10^-2
80
64
48
32
16
0
13.0
13.5
14.0
14.5
15.0
15.5
16.0
SPECTROMETER SHUNT VOLTAGE (MV)
*1 (ΔE/E)½ = 1.71 % 13.36
*2 (ΔE/E)½ = 1.79 % 13.60
*3 (ΔE/E)½ = 2.06 % 13.87
*4 (ΔE/E)½ = 2.24 % 14.16
*5 (ΔE/E)½ = 2.36 % 14.51
*6 (ΔE/E)½ = 2.30 % 14.92
*7 (ΔE/E)½ = 2.40 % 15.38
*8 (ΔE/E)½ = 2.64 % 15.73
.114
.122
.143
.158
.171
.172
.185
.208

FIGURE 2

energies obtained from the C^{12} proton endpoint at 24.5 Mev were used in plotting the data from the excitation experiments.

2.2 Calibration and performance of the SEM. Other experimenters working on the Mark III linac at Stanford have observed large deviations in the response of their SEM's in the course of a few hours' running time; consequently, the reliability of these beam-current monitors has long been suspect. In order to check the performance of the SEM and the stability and reliability of the counting equipment, signal runs were intersticed with 0.003-in. Al-target runs which yielded, in the energy range of interest, around 3000 counts in the eight counter channels in a standard 272-μcoul run. Since the target was relatively thick for protons ($\overline{\Delta E} \cong .8$ Mev for $E_p \cong 3.5$ Mev), any structure in the Al energy spectrum would have been smoothed by straggling in the target, so that any deviation from a monotonic yield of Al protons could have been interpreted as a malfunction of an experimental component. The Al data were also subsequently used to evaluate the relative efficiencies $(\Delta p/p)\Delta\Omega$ of the various counters. These Al measurements indicated no statistically significant deviation of the experimental components' performance for the energy- and excitation-function measurements in which the SEM position, relative to the beam, remained constant. Two absolute calibrations of the SEM response with a Faraday cup were made 71 days apart: the efficiency at $E_0 = 30$ Mev (0.0294% for three foils) was the same within .3%. The method of data-combination tended to minimize fluctuations in the counting efficiency of the various counters and in SEM response.

In experiments where large deviations in SEM efficiency have been observed, the SEM was portable and consequently the beam-spot traversed the SEM foils in different spots in each calibration run. This variation in SEM position has been alleged to explain the observed deviations. This effect was probably observed during our angular distribution runs. These runs necessitated a repositioning of SEM at each angle although with good position reproducibility. After completion of the angular distribution measurements Al runs were taken over a sizable energy range and yield decreases of 7.5% were observed on all counters. Since the yield decrease was noted on all counters, it is likely that the SEM was the offending component. Concurrently with these Al calibration measurements the O energy spectrum below the 9.2-Mev peak was measured and these data subsequently normalized to the previous SEM calibration.

The response of the SEM relative to the Faraday cup was measured as a function of electron energy E_0 for use in the excitation experiments. The relationship $R = -.092\ E_0 + 36.77$ (Fig. 3), where R is the ratio of Faraday-cup response to SEM response, was found. However, since the distance between SEM and Faraday cup was 32 in.— a more intimate arrangement being prohibited by the spectrometer base and scattering chamber — the measured ratio R should have been corrected for multiple scattering in the $.495 \times 10^{-3}$ radiation length of Al the beam traversed before entering the 4-in.-diameter mouth of the Faraday cup. If the assumptions of a uniform intensity distribution of the electron beam (width ~ 0.50 in.), perfect alignment of Faraday cup and SEM, and a Gaussian distribution of multiple scattering angles[25] with rms angle

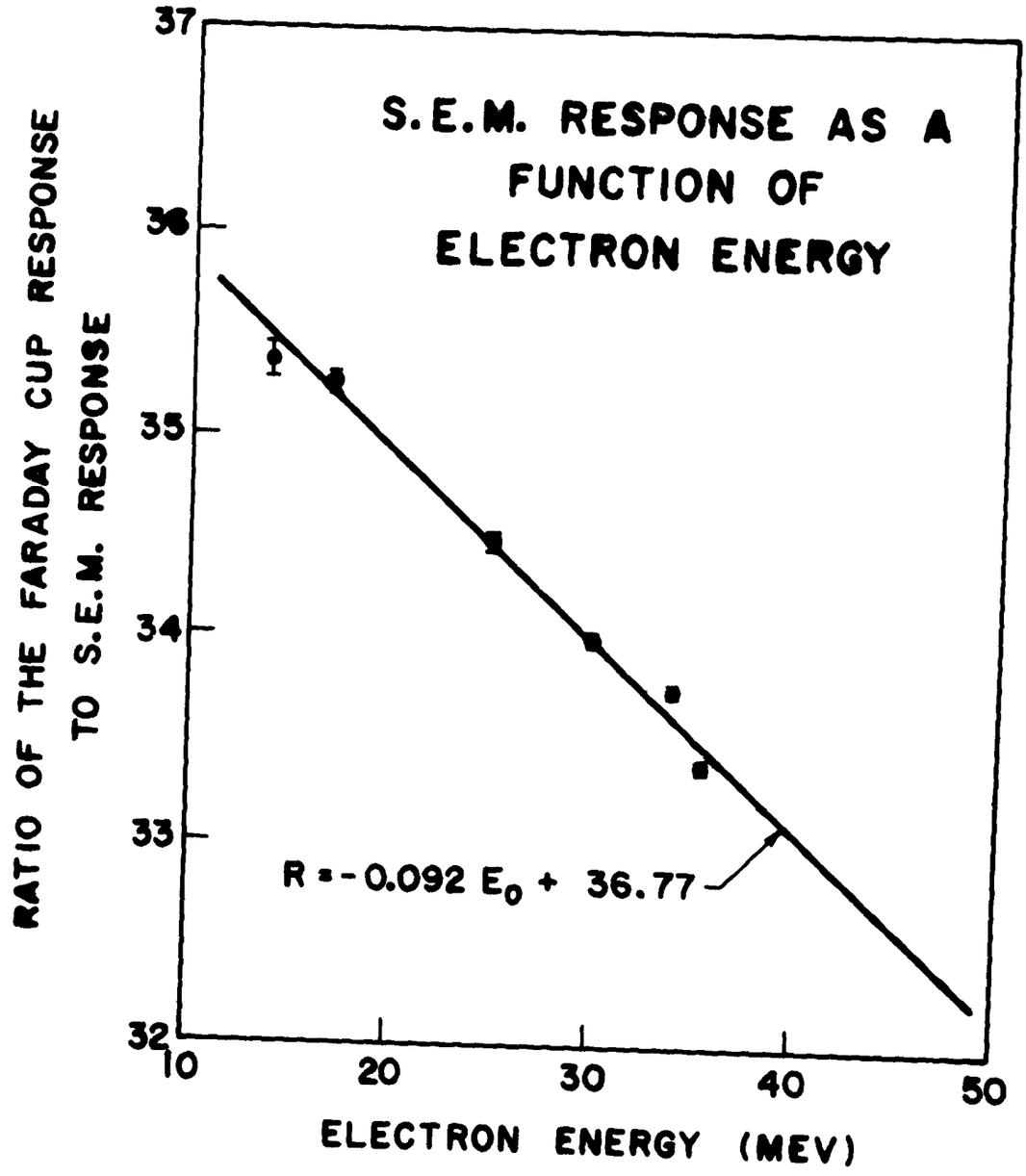
S.E.M. RESPONSE AS A FUNCTION OF ELECTRON ENERGY
RATIO OF THE FARADAY CUP RESPONSE TO S.E.M. RESPONSE
37
36
35
34
33
32
10
20
30
40
50
ELECTRON ENERGY (MEV)
R = - 0.092 E0 + 36.77

FIGURE 3

$$\sigma = (21.2/E_0)\sqrt{t}\ C(Z,t)\ , \qquad (5)$$

where t is the thickness of the scattering material in radiation lengths, and $C(Z,t)$ is a correction factor which depends on the atomic number Z and the thickness t of the scattering material [$C(Z,t) = .64$ for $t = 5 \times 10^{-4}$ radiation lengths and $Z = 13$] are made, then 99.5% of the beam at 16 Mev and essentially 100% of the beam at 30 Mev passed through the Faraday-cup opening. The measured response curve, however, was used to correct excitation data for the E_0 dependence of the SEM; and neither the counting statistics near threshold nor machine energy stability justified a further concern over the small additional correction necessitated by multiple scattering of the beam in the window ahead of the Faraday cup.

2.3 Spectrometer energy and solid-angle calibration. The energy calibration of the spectrometer was accomplished with the use of a Cm^{244} α-particle source as described previously.[23] The same median-field measurements versus magnet-shunt current were used as in reference 23; but the experimental points were fitted by an algebraic expression of third degree, which was subsequently solved for the field values, thus resulting in automatically smoothed field values. The field values in gauss as a function of the magnet-shunt current X were $H = 501\ X$, $0 \leq X \leq 15.10$; $H = -.2667\ X^3 + 9.818\ X^2 + 386.7\ X + 404.4$, $15.10 \leq X \leq 23.18$; $H = .3518\ X^3 - 36.91\ X^2 + 1555.9\ X - 9287.1$, $23 \leq X \leq 29.85$. In the proton-energy range of interest the relationship between current and field was essentially linear. The proton energies were computed

using the first order relationship

$$E_p = E_p^0[1 - \tfrac{1}{2}(E_p^0/M_p c^2)] , \qquad (6)$$

where E_p^0 is the nonrelativistic proton kinetic energy $(eH\rho)^2/2M_p c^2$. The $H\rho$ value was calibrated by masking the α-particle source in such a way as to duplicate the beam contour as well as possible and then carefully placing the α-particle source at the experimentally determined beam height. Alpha-particle-source resolution curves (Fig. 2) were then measured, and the center of the curves assumed to correspond to an α and hence a proton energy of 5.81 Mev. Then

$$E_p^0 = \frac{(eH\rho)^2}{2M_p c^2} = \frac{M_\alpha}{4M_p} E_\alpha \left(\frac{H}{H_\alpha} \right)^2 , \qquad (7)$$

where H_α is the field corresponding to the center of the resolution curve. The shunt current corresponding to the center of the α-particle resolution curve for counter 7 was reproducible to within .7%. While it is well-known that diffusion of the atoms upon which the source is plated can cause an effective thickening of the source and consequently a reduction in the mean α-particle energy, the unattenuated energy of the strongest line, 5.81 Mev, was used in the calibration.

The fractional change in the energy $\Delta E/E$ for a given spectrometer field produced by a fractional change in the source height is given by $\Delta E/E = .515\ \delta S_r/S_r$ according to Judd,[26] where S_r is the source height corresponding to an energy E and coefficient .515 is a characteristic of the spectrometer (S_r = 28 in., field index $n = 1/2$, average radius

of curvature r_0 = 18 in., and the angle of deflection θ = 120°). During data runs frequent beam-spot pictures were taken to check vertical and horizontal alignment of the beam. These beam alignment checks ensured that excessive vertical deflections did not broaden the effective energy resolution or shift the energy calibration.

The spectrometer solid angle was measured with the use of Cm^{244} α-particle source and a movable system of baffles whose dimensions were 2/3, 1/2, and 1/3 of the spectrometer aperture dimensions. The effective source strength was determined by placing baffles of successively smaller area in front of the magnet aperture until the counting rate was proportional to the baffle area. The counting rate with the 1/2-size baffle was 9/4 that with the 1/3-size baffle; so it was assumed the spectrometer solid angle was the ratio of the unbaffled α-counting rate to the 1/2-size baffled α-counting rate, times the solid angle defined by the 1/2-size baffle, 2.99×10^{-3} sr. This method assumes that the source emits α-particles isotropically into a solid angle at least as big as the spectrometer solid angle. The alteration of the spectrometer resolution by reducing the effective solid angle should not invalidate this procedure if areas under the differently baffled resolution curves are used. In practice, since the ratios of the ordinates of the resolution curves under differently baffled conditions were constant to within statistics, only the counting rates at the peaks were used. Although all counters should subtend the same spectrometer solid angle, the most reliable measurements would be expected for counters near the central ray.

In order to compute absolute cross sections the value of the spectrometer energy acceptance $\Delta E/E$ must be known. If the spectrometer aberrations and α-particle-source-line shape are known, then $\Delta E/E$ can be calculated directly by unfolding the α-particle resolution curves. However, since detailed knowledge of these parameters is not available the values of $\Delta E/E$ for the various counters were calculated by means of the proton-energy calibration formula [Eq. (6)], written in the form

$$E_i = k_i H^2 [1 - (k_i H^2 / 2M_p c^2)] , \qquad (8)$$

and by means of the scintillator width and average counter separation. The spectrometer energy acceptance $\Delta E/E$ for the i-th counter was obtained by averaging the energy difference of the (i + 1)th and (i - 1)th counters, dividing by the energy of the i-th counter, and multiplying by the ratio of the scintillator width W_s to average counter separation W_c . Thus,

$$\left(\frac{\Delta E}{E}\right)_i = \frac{W_s}{W_c} \frac{k_{i-1} - k_{i+1}}{2k_i} \left(1 - \frac{k_{i-1} + k_{i+1} - k_i}{2M_p c^2} H^2\right) , \qquad (9)$$

where

$$k_i = \frac{M_\alpha}{4M_p} E_\alpha \frac{1}{(H_\alpha)_i^2} ,$$

$$W_s = 1.187 \text{ in.} ,$$

and

$$\bar{W}_c = 3.56 \text{ in.}$$

For counters 1-8, the k_i values were 1.2868, 1.2429, 1.1951, 1.1465, 1.0919, 1.0328, 0.9719, and 0.9292. These values were obtained without recycling the magnet and during a short time interval; so the true ΔE values should have been preserved. [The calculation of $(\Delta E/E)_7$ was modified by counter 8's forward location.] The solid angle with the lead baffle used with the gas targets was related to the solid angle without lead baffle by comparing the ratios of the Al data at one proton energy. Table I lists the values of $\Delta\Omega$ obtained from α-particle measurements with each counter. Using the magnet-face target distance minus half the gap distance for the source distance, an equilibrium-orbit radius of 18 in., and an accessible magnet-vacuum-chamber area of 14.1 in.^{2}, the first order theory predicts[26] $\Delta\Omega = 1.03 \times 10^{-2}$ sr.

In order to determine absolute cross sections, the quantity $(\Delta E/E)\Delta\Omega C$ must be evaluated.[23] This quantity [$(\Delta E/E)\Delta\Omega C$], where C is the number of electrons per unit monitor response [$C = R\, C_I(Q_I/q_e)$, where R is the reciprocal of the SEM efficiency, C_I is the capacity of the integrator capacitor in farads, Q_I is the charge accumulated on the integrator capacitor per monitor response, and q_e is the electronic charge in coulombs], was obtained by synthesis of the directly measured values of $\Delta\Omega$, $\Delta E/E$ and C, and also by the virtual photo-disintegration of D, using the gas target. The D (e,pe') data used in the calibration are shown in Fig. 4. The total cross section $\sigma_T = 1.1 \pm .10$ mb and angular distribution $d\sigma/d\Omega = .11(.093 + \sin^2\theta)$ mb/sr, measured by Whetstone and Halpern[27] at a photon energy of k = 12.5 Mev, were assumed as was the validity of the virtual-photon formulism

TABLE I. Solid angle and $\Delta E_p/E_p$ determinations.

Counter	$\Delta E_p/E_p$ (%)	$\Delta\Omega \times 10^3$ with Pb baffle	$\frac{\Delta E_p}{E_p}\Delta\Omega \times 10^5$	$\frac{\Delta E_p}{E_p}\Delta\Omega \times 10^3$ Norm. to no.7	$\frac{\Delta E_p}{E_p}\Delta\Omega \times 10^3$ From Al data	$\Delta\Omega$ ratio with and without Pb baffle	Unbaffled $\Delta\Omega \times 10^{-2}$
2	1.23	8.1	10.0	0.59	0.45	.80 ± .06	1.01 ± .06
3	1.34	8.5	11.4	0.67	0.57	.78 ± .05	1.09 ± .06
4	1.50	8.7	13.1	0.77	0.74	.75 ± .05	1.16 ± .06
5	1.74	8.7	15.1	0.90	0.90	.80 ± .04	1.09 ± .05
6	1.94	8.7	16.9	1.00	1.00	.71 ± .04	1.22 ± .06
7	1.89	9.5	17.9	1.06	1.06	.83 ± .04	1.16 ± .05
Mean Values	——	8.7 ± .4	——	——	——	.78 ± .04	1.11 ± .08

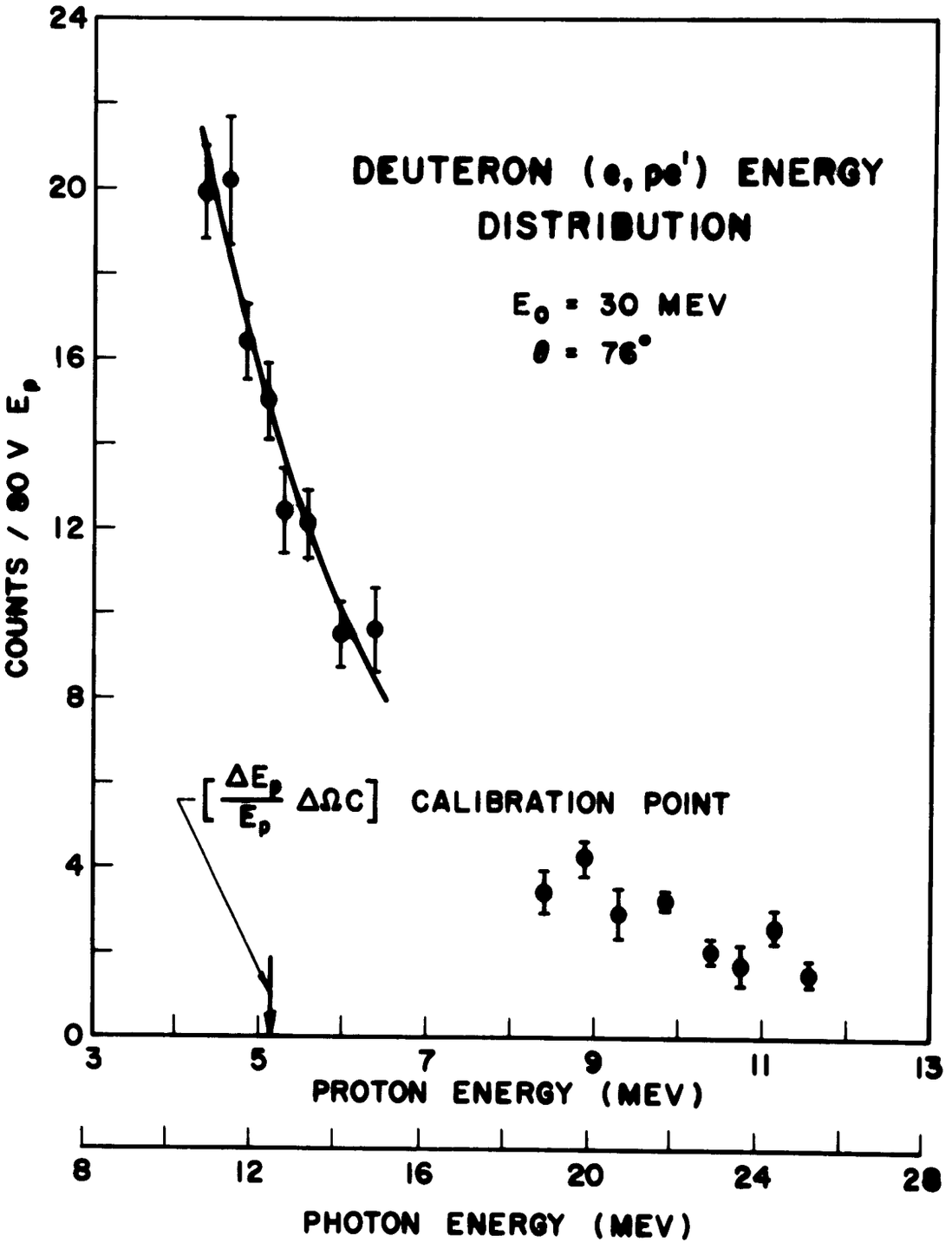

FIGURE 4

Deuteron (e,pe') energy distribution at 76° and E_0 = 30 Mev. The solid curve is an approximate fit to the yield around the $(\Delta E/E)\Delta\Omega C$ calibration point.

[Eq. (4)]. The real photons produced in the 0.495×10^{-3} radiation length of the SEM and window and 0.354×10^{-3} radiation length of gas-chamber wall were included in the calculation. This measurement gave

$$\left(\frac{\Delta E}{E}\right) \Delta\Omega C = \left(\frac{d\sigma}{d\Omega}\right)_{76°} \frac{1}{2} \frac{k}{N(E_0,k)} \frac{N_p}{n_t V E} , \qquad (10)$$

equal to 4.6×10^9 sr-electrons per unit monitor response, where $N(E_0,k)$ is the number of real and virtual photons of energy k per incident electron of energy E_0, n_t is the number of target nuclei per unit area, N_p is the number of protons emitted into the spectrometer solid angle for monitor response V, and E is the proton energy. The integrator capacitor was measured against a standard capacitor in the usual way[23] and found to be .104 μfarad. Using this value to calculate C and the measured values of $\Delta\Omega$ and $\Delta E/E$, 3.96×10^9 is obtained for $(\Delta E/E)\Delta\Omega C$. This synthesized value can be compared with the D value after the latter has been corrected for the presumed SEM efficiency increase which occurred before the D calibration experiment. The corrected value of 4.3×10^9 from the deuteron experiment and the synthesized value of 4.0×10^9 agree within 8%. The synthesized value was used in cross-section determinations.

The effective gas-target length at 76° was determined by masking the α-particle source to a .06-in. vertical slit and measuring the counting rate as a function of lateral displacement from the scattering-chamber center, as the source was moved in the beam direction. The effective target thickness was assumed to be the width of a rectangle with the

same area and height as the experimentally measured trapezoid which resulted in an effective target thickness of 1.01 ± .03 in. (See Chapter III.)

The solid angle was not corrected for the second-order effects arising from finite target and beam width since this correction is less than 1% for all the conditions of this experiment. For a spectrometer with field index $n = 1/2$,

$$\langle \Delta\Omega \rangle = \frac{A_0}{2\sqrt{2}\, r_0\, \Delta S_0} \left(\tan^{-1} \frac{2\sqrt{2}\, \Delta S_0\, r_0}{2r_0^2 + S_0^2 - \Delta S_0^2} \right) , \qquad (11)$$

where S_0 is the effective source distance, ΔS_0 the half-width of the electron beam, r_0 the radius of curvature of the magnet, and A_0 the area of the magnet aperture. For small ΔS_0 ,

$$\langle \Delta\Omega \rangle = \Delta\Omega_0 \left[1 + \frac{\Delta S_0^2}{2r_0^2 + S_0^2} \left(1 - \frac{8}{3} \frac{r_0^2}{2r_0^2 + S_0^2} \right) \right] . \qquad (12)$$

The maximum ΔS_0 encountered in this experiment is 1 in.; therefore,

$$\langle \Delta\Omega \rangle = (1.0003)\Delta\Omega_0 .$$

2.4 Target energy-loss calibration. The wall thickness of the gas chamber was determined by placing the α-particle source in the center of a chamber of the same dimensions, and fabricated by the same method as the signal-gas chambers, but with removable top to facilitate insertion of the source. Originally, it was planned to determine the energy-loss in both the gas and the target wall by this method, but time limitations and the

relatively short range of 5.81-Mev α particles precluded these attempts. The mean energy of the α particles which had traversed the wall was determined by measurements with the spectrometer magnet to be 3.36 Mev. This corresponds to a mean energy-loss in the target wall of 2.44 Mev for 5.81-Mev α particles (see Fig. 5). The 301 stainless-steel foil which constituted the gas-chamber wall was directly measured before the soldering operation to be 12% thicker than the value obtained from the α-particle energy-loss data. The velocity of a 3.36-Mev α particle is 1.29×10^9 cm/sec, at which velocity the effective charge due to random pick-up and loss of electrons is 1.97 q_e, so that this effect cannot entirely explain the observed discrepancy. Finite α-source width (.47 in.) and target curvature increase the effective wall thickness by about 1%. The most likely explanation of the discrepancy between the direct and α-particle energy-loss measurements is an error in the ionization potential or attrition of the wall material by oxidation during the soldering operation. The wall thickness determined by the α-particle measurements was used in computing the proton energy losses in the target wall.

The integrated non-relativistic form of the well-known Bethe-Bloch formula

$$\mathrm{Ei}\left[2 \ln\left(4 \frac{m_e}{M_p} \frac{T_i}{I}\right)\right] - \mathrm{Ei}\left[2 \ln\left(4 \frac{m_e}{M_p} \frac{T_f}{I}\right)\right] = 32\pi\alpha^2 \frac{m_e}{M_p} \Delta x \; N_0 \frac{Z}{A} \left(\frac{\hbar c}{I}\right)^2 \qquad (13)$$

was used to calculate the proton's energy losses in the gas and gas-chamber wall. In this formula Ei is the extensively tabulated exponential integral; Δx is the mass per unit area and I the ionization

ENERGY LOSS OF 5.80 MEV α PARTICLE IN THE GAS TARGET WALL

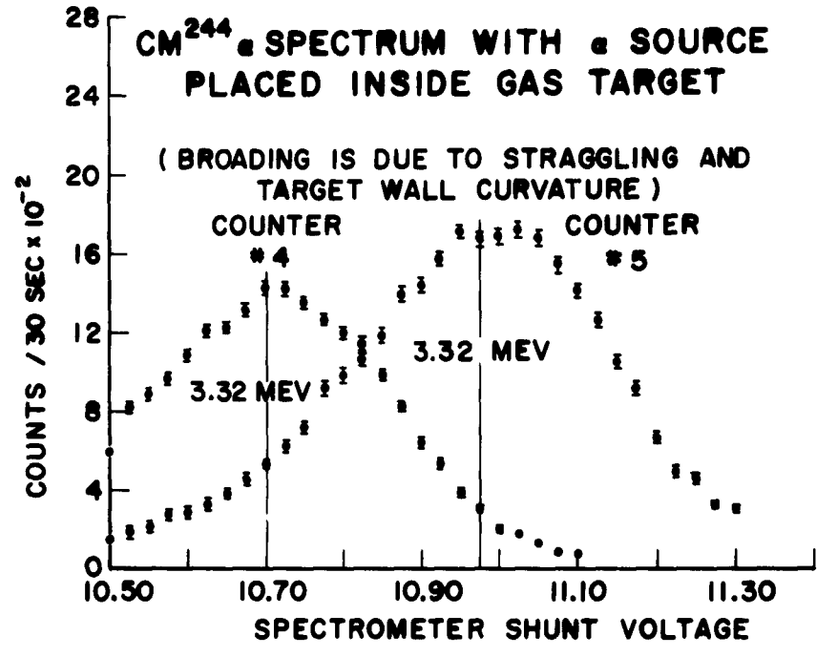

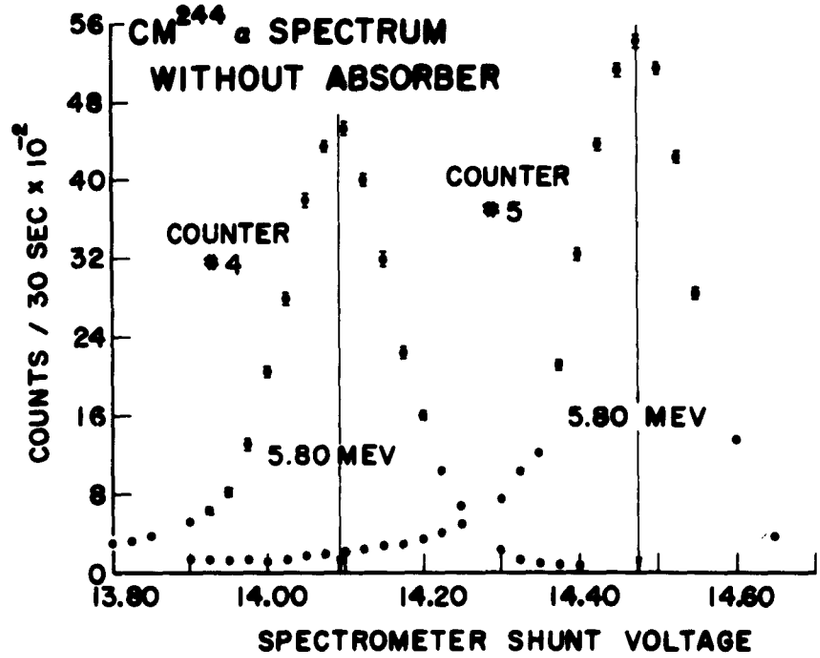

FIGURE 5

potential of the matter the proton traversed, and the other symbols have their usual meaning (m_e/M_p is the ratio of electron to proton mass and is equal to 1/1836, $\hbar$ is Planck's constant/2π, c is the velocity of light in a vacuum, N_0 is Avogadro's number, and Z and A are the atomic and mass number of the stopping matter). The proton energy loss in the polystyrene (CH) and teflon (CF_2) foils was calculated with the data of Rich and Madey.[28] For teflon, the formula

$$\left(\frac{dT}{d\xi}\right)_{CF_2} = \frac{96}{100}\left(\frac{dT}{d\xi}\right)_C\left[1 - \frac{3}{4}\frac{\ln(I_F/I_C)}{\ln(2mv^2/I_C)}\right] \qquad (14)$$

was used. For the gaseous boroethane (B_2H_6) target, the approximate formula

$$\left(\frac{dT}{d\xi}\right)_{B_2H_6} = \frac{\ln 8}{\ln 5}\left(\frac{dT}{d\xi}\right)_{O_2} = 1.29\left(\frac{dT}{d\xi}\right)_{O_2} \qquad (15)$$

was used. The values of the ionization potentials employed were $I_C = 76.2$, $I_O = 97.6$, $I_F = 108.4$, $I_{Ne} = 119$, $I_A = 187$, and $I_{Fe} = 241$ ev. One half the total effective target thickness was used for Δx for the solid targets, while .95 of the gas-target radius was used for Δx for the gas targets.

C. Ported Scattering-Chamber Design

Motivated by the desire to extend angular distributions to more extreme forward and backward angles than were accessible with existing scattering chambers and to eliminate as much of the matter the beam

traversed before the target as possible — for both these proton experiments and inelastic electron scattering experiments — a ported scattering chamber was designed. In the design which was adopted the electron beam pipe was directly connected to one of the scattering-chamber ports, depending on the selected scattering angle, and the spectrometer and accelerator vacuums were continuous. While this arrangement satisfies the two design objectives admirably, it increases the difficulty of angular changes greatly but not prohibitively. Other important design considerations are the solid angle subtended by the target and output window, and a suitable range of scattering angles. The target output-window solid angle is essentially independent of the scattering-chamber radius, the window diameter being proportional to the radius, but the existing apparatus and surface area needed for an O-ring vacuum seal dictated a chamber radius of 10 in. Angles of 20°, 48°, 76°, 104°, 132°, and 160° were accessible with a symmetric arrangement of ports around the spectrometer input channel. In order to extend the angular range to include the interpolated half-angles, the spectrometer input channel and the two adjacent ports were made removable so that an insert with a spectrometer input channel shifted by 14° could be installed. The original intention to incorporate the spectrometer and accelerator vacuum systems was abandoned because a small leak in the spectrometer-magnet vacuum system necessitated separating the SEM and accelerator vacuum systems from the spectrometer vacuum system by a .001-in. Al window to obtain reliable SEM performance.

D. Gas-Target Design

The most prevalent configuration for gas targets in this laboratory is a cylinder orientated so that the electron beam passes through parallel to its longitudinal symmetry axis, this design being desirable for electron scatterers because of the large effective target length and because, in general, energy loss in the walls for electrons at higher energies is not a serious problem even at extreme angles. For the study of the (e,pe') reaction, however, an effective target thickness of ~ 5 mg/cm^2 provides an ample counting rate in most cases, and energy-loss considerations are paramount. These considerations imply that a cylinder with the beam passing through perpendicularly to the longitudinal axis would be an experimentally propitious arrangement. Since stressed organic materials quickly fail under high-energy electron bombardment, thin metallic foils were indicated for the window material. Preliminary experiments were made with a target chamber fabricated from a 2-in. diameter, 0.06-in. wall stainless-steel cylinder, 2-in. high, with a window opening 1-in. high and extending around the cylinder circumference except for a 1-in. supporting web. The window material was 0.00025 in. of 301 stainless steel.[29] This target chamber design showed that the limited vertical clearance and supporting web were a source of copious background. The subsequently developed target had a vertical clearance of 1-1/2 in. and a single gold-silver soldered wall-seam and no supporting web. This configuration was probably mechanically superior to the supporting web construction because it allowed the targets to assume a more symmetric and hence more mechanically desirable shape. Background from

the target walls was unavoidable at extreme angles; but, with a suitable choice of target radius and spectrometer baffles, it could largely be eliminated at angles nearly perpendicular to the beam. In order to restrict the spectrometer's view of the target walls a lead baffle was placed in the spectrometer entrance port, 8.95 in. from the scattering-chamber center. Experiment indicated that a lead baffle with a rectangular hole of horizontal dimension .880 in. and vertical dimension 1.975 in. would reduce the background counting rate by a factor of ~ 5, while only reducing the effective spectrometer solid angle 20% (the residual background was twice background from external sources alone under these conditions). For an experiment with equal signal and background rates this arrangement would reduce signal statistical errors to 75% of those of the unbaffled arrangement. Background from target walls became more virulent when angular distributions were measured, since in the forward and backward directions the spectrometer could clearly "see" the target walls. However, at these angles the effective target length increased enough so that a workable signal-to-noise ratio was maintained.

Two similar target chambers, one containing the signal gas and the other H_2 for background measurements, were used in (e,pe') experiments. Both chambers were inflated to nearly equal pressures so that they would have nearly identical shapes and were interchanged occasionally to test their (e,pe') similarity. As would be expected under baffled conditions, the slight difference in gas-target shape and construction produced only a slight (2%) statistically unreliable difference between H_2 background rates for the two targets. The background counting rate due to electron

pile-up is not expected to depend greatly on multiple scattering of the primary electron beam in the target, assuming that the primary target background contribution is to multiple-scatter the incident beam rather than to Mott-scatter it, the latter process being important in the thick walls of the scattering chamber beyond the target and in the .001-in. (Fe) exit window. Multiple-scattering of the electron beam before Mott-scattering changes the $(\cos^2 \theta/2)/(\sin^4 \theta/2)$ angular dependence of the Mott cross section to

$$\frac{\cos^2 \frac{\theta}{2}}{\sin^4 \frac{\theta}{2}} \left(1 + \frac{\sigma^2}{\sin^2 \frac{\theta}{2}} + \frac{\sigma^2}{2 \cos^2 \frac{\theta}{2}} \right) , \qquad (16)$$

where σ is the multiple-scattering rms angle [Eq. (5)], and provided $\theta \gg \sigma$. Therefore, the electron pile-up background rate should not be increased significantly by multiple scattering in the target. Mott-scattered electron intensities were 100-times greater from the target gases than from H; but single electron-scattering events in the target contributed negligibly to the background, and consequently no background subtraction bias was expected from this source.

The background subtraction method used with the gas target was clearly valid as the above considerations showed. The target-in target-out method of background subtraction used with the solid targets was experimentally confirmed with the CH target by using an incident electron energy of 24.5 Mev and searching with a null result for signal above the proton threshold.

The target wall curvature decreased the overall resolution very little. Since the beam-spot was small compared to the dimensions of the gas container (a probable beam half-width of 3/16 in. compared to the 1-in. chamber radius), and since the energy loss in the target wall in the normal direction was nearly equal to the energy loss in the target gas in a target radius distance, then $\Delta(dE/dx)/(dE/dx)$ varied like $-1/8(d/R)^4$; so that the energy loss was sensibly constant out to a distance of .7R, where $\Delta(dE/dx)/(dE/dx) = 3\%$, and where the efficiency of the spectrometer at 76° for detecting protons was only 25%.

The actual fabrication of the gas target chambers was carried out in the High-Energy Physics Laboratory Tube Shop by William Ewing. It was experimentally shown that the gas containers would hold approximately four atmospheres, indicating that the yield strength of stainless steel can be scaled almost linearly with thickness in this thickness region, a similar target of approximately .5-in. radius and .001 in. thickness having held 22 atmospheres.

E. Description of Targets

Table II contains a description of the targets used in our experiments. The pressure of the gaseous targets was recorded with a Bourdon tube gauge (the manufacturer's estimated absolute accuracy was ± .05 lb/in.^{2}) and Hg barometer at frequent intervals. The temperature of the air near the scattering chamber was recorded and not the temperature of the target gas; but inaccuracies due to temperature lags between the air and the target-cell environment were small (total daily temperature variations

TABLE II. Description of targets.

Element	Target	Isotopic composition (%)	Supplier and purity (%)	Actual target thickness (mg/cm^2)	Average absolute pressure ($lb/in.^2$)	Target thickness at NTP (mg/cm^2)
O	O_2	(99.8) O^{16}	Linde Co.[a] MSC grade (99.99)	6.29	27.8	3.66
F	CF_2	(100) F^{19}	——— (100)	2.55	——	——
Ne	Ne	(90.9) Ne^{20} (0.3) Ne^{21} (8.8) Ne^{22}	Linde Co. MSC grade (99.99)	3.66	25.2	2.31
A	A	(99.6) A^{40}	Linde Co. com'l grade (99.99)	4.79, 6.34	16.8, 22.7	4.56
B	B_2H_6	(18.7) B^{10} (81.3) B^{11}	Bios Labs[b] (unspecified)	——	27.2	——
C	CH	(98.9) C^{12} (1.1) C^{13}	A. D. Makay[c] (100)	3.54	——	——
Al	Al	(100) Al^{27}	Com'l Al foil	20.6	——	——

(a) Linde Co., Division of Union Carbide Corp., 22 Battery Street, San Francisco, California.
(b) Bios Laboratories, Inc., 17 West 60th Street, New York 23, New York.
(c) A. D. Makay, 198 Broadway, New York 38, New York.

were less than 15°C), and the data-combination method tended to average these errors to zero. The average of the individual runs for each counter at each datum point was corrected to NTP using the average temperature and pressure conditions encountered during the datum point run.

F. The Method of Data Combination

The data from the eight counters were grouped into energy bins less than 1% wide which contained on the average data from three counters. Each proton-energy interval was corrected for target-energy losses, and the datum from each counter in the energy interval was multiplied by the reciprocal of the relative counter efficiency $(\Delta E/E)\Delta\Omega$, and the mean datum point for this energy interval was computed in the usual way ($\overline{W} = \Sigma P_i W_i / \Sigma P_i$, where the P_i's are the reciprocals of the squares of the standard deviations associated with the W_i's). The relative efficiencies of the counters were obtained from the Al data-runs by plotting the ratios of the counting rates of the other counter to counter 7. The modulation of the ratios due to small random variations in counter 7's efficiencies were removed by renormalization of the ratios with subsequent renormalization of counter 7's efficiency. The experimental data are shown in Figs. 6 and 7. The renormalized efficiencies of the counters with a Pb-baffle, described in Section D above, were .31, .42, .54, .70, .85, .94, 1.00, and .98; without a Pb-baffle they were .30, .41, .53, .71, .87, .93, 1.00, and 1.01. Therefore, the counting statistics for the combined data should be $\sqrt{5.76}$, or 2.4 times better than those of counter 7. In fact, since the ratios of the counters were constant over the

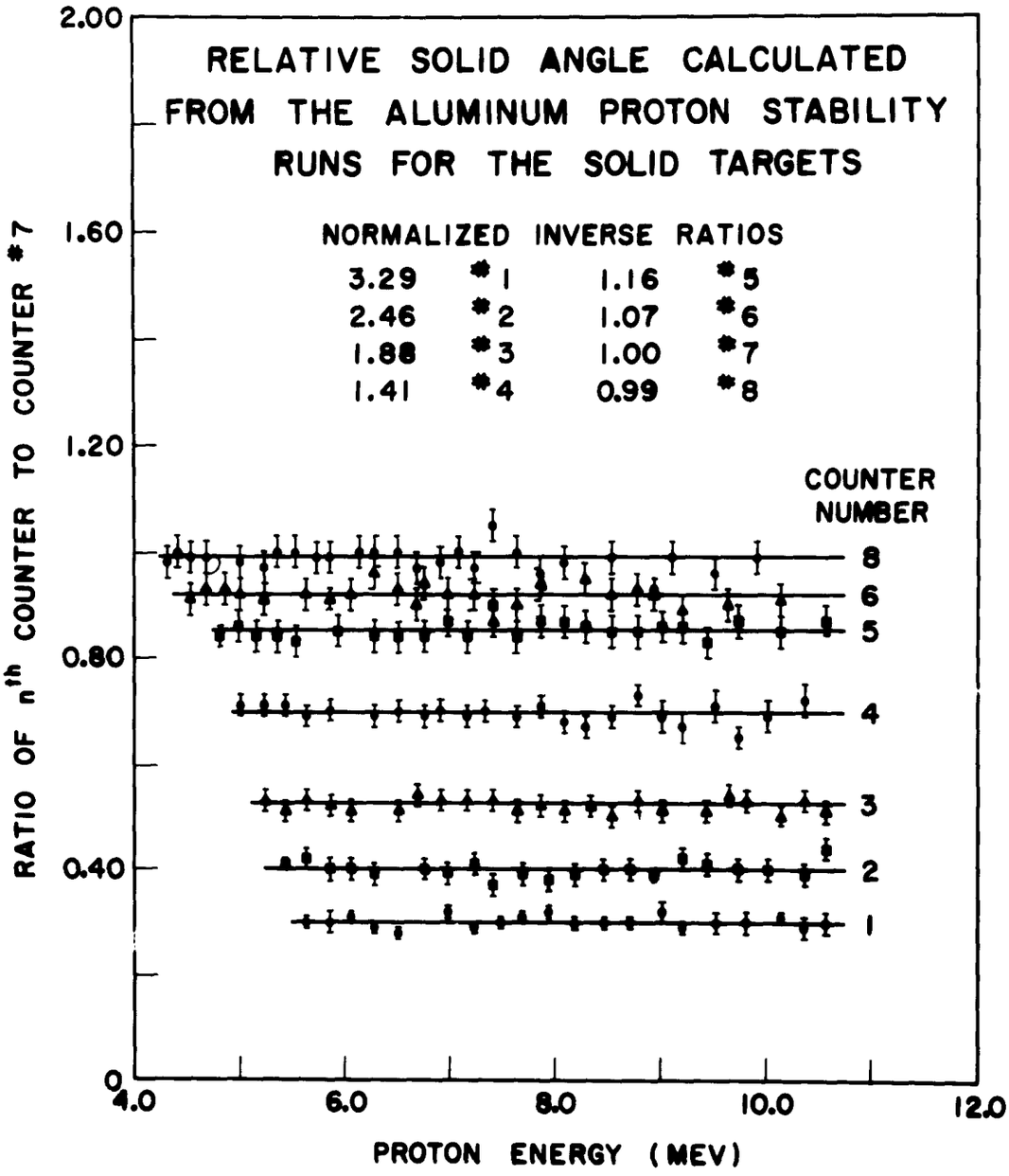
RELATIVE SOLID ANGLE CALCULATED
FROM THE ALUMINUM PROTON STABILITY
RUNS FOR THE SOLID TARGETS
NORMALIZED INVERSE RATIOS
3.29 #1
2.46 #2
1.88 #3
1.41 #4
1.16 #5
1.07 #6
1.00 #7
0.99 #8
COUNTER NUMBER
8
6
5
4
3
2
1
RATIO OF nth COUNTER TO COUNTER #7
2.00
1.60
1.20
0.80
0.40
0
4.0
6.0
8.0
10.0
12.0
PROTON ENERGY (MEV)

FIGURE 6

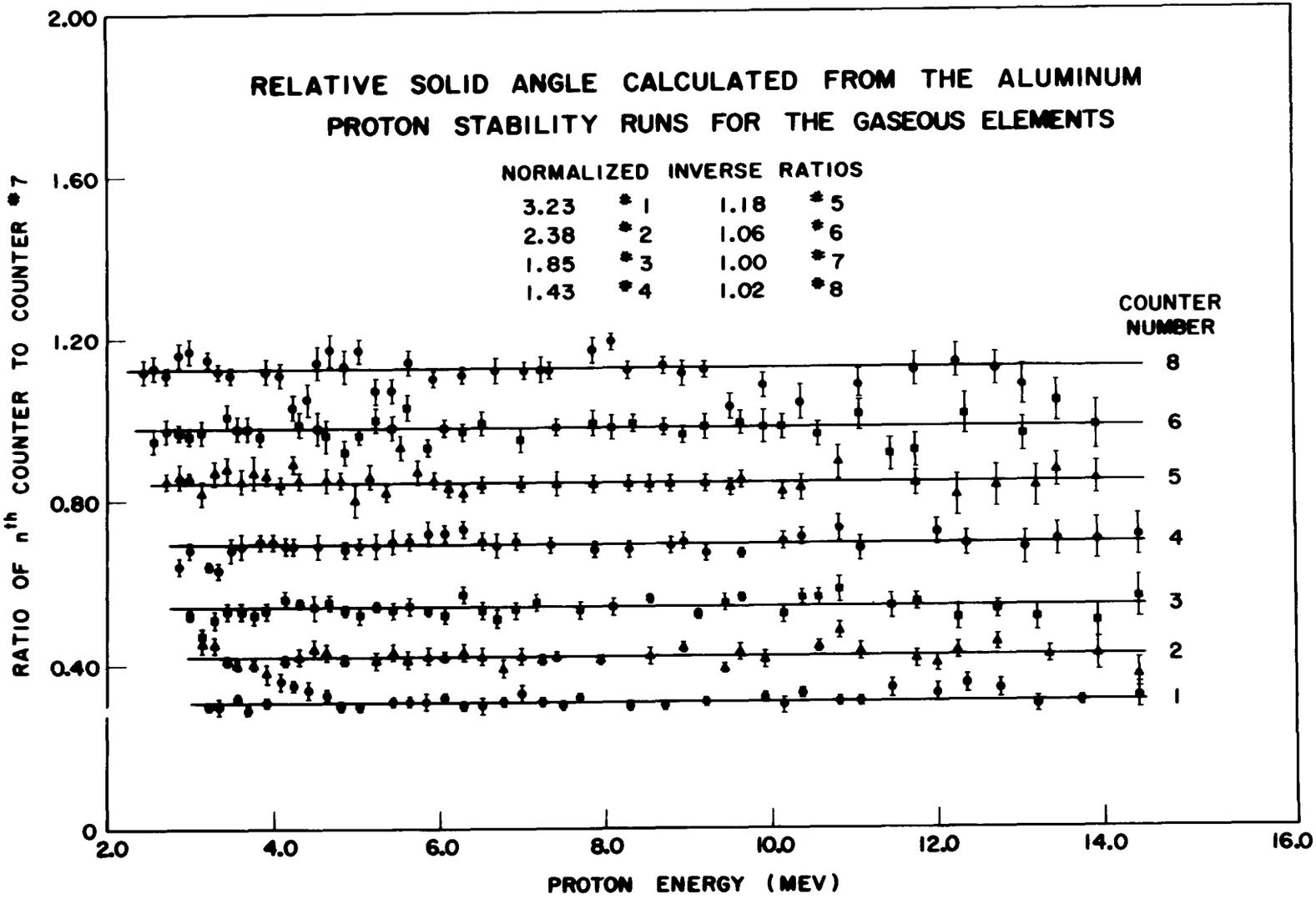
RELATIVE SOLID ANGLE CALCULATED FROM THE ALUMINUM
PROTON STABILITY RUNS FOR THE GASEOUS ELEMENTS
NORMALIZED INVERSE RATIOS
3.23 #1
2.38 #2
1.85 #3
1.43 #4
1.18 #5
1.06 #6
1.00 #7
1.02 #8
COUNTER NUMBER
8
6
5
4
3
2
1
RATIO OF nth COUNTER TO COUNTER #7
2.00
1.60
1.20
0.80
0.40
0
2.0
4.0
6.0
8.0
10.0
12.0
14.0
16.0
PROTON ENERGY (MEV)

FIGURE 7

energy range employed, the assumption of 100% counting efficiencies, made highly plausible by integral discriminator curves with wide plateaus, was supported; and furthermore, since the experimental points for the same energy were taken at different times, the confidence level attached to the data is somewhat greater than if 5.76 times as many counts were accumulated on one counter.

In the region below 13.0 mv spectrometer shunt current, the proton pulses in the scintillators were the same order of magnitude as electron pile-up pulses; and, therefore, the background rate was slightly sensitive to beam alignment, which could depend on gun and accelerator tune-up parameters. Therefore, it is expected that the standard deviations computed from the variation in the standard, 272-μcoul runs (about 20 signal and 20 background, standard runs in this region) would be larger than those expected from counting statistics. While uncertainties in the branching ratios to ground and excited states of the residual nucleus vitiate the practical value of any statistical test for goodness of fit, since the cross section to a definite final state is the more interesting information, a comparison of the standard deviations predicted by Poisson statistics and those computed from internal consistency in the usual fashion at different spectrometer shunt voltages are given in Table III for the Ne energy distribution. It is obvious that the errors on the first six points of the Ne energy distribution, which were computed by assuming Poisson statistics, should be increased by a factor of ~ 2.

TABLE III. Ratio of computed standard deviations from internal consistency and those predicted by Poisson statistics for Ne energy distribution data.

Spectrometer shunt voltage	Counter no. 1	Counter no. 2	Counter no. 3	Counter no. 4	Counter no. 5	Counter no. 6	Counter no. 7	Counter no. 8
10.00	3.5	3.5	3.1	2.6	2.7	4.2	4.1	1.9
11.00	1.4	2.0	1.2	1.8	2.2	2.8	1.6	2.0
13.00	1.5	1.2	0.8	1.3	1.0	0.2	0.4	0.6
15.00	0.5	0.4	1.9	1.4	1.0	1.0	0.8	1.1
17.00	0.5	2.5	0.8	0.7	2.5	0.7	1.2	0.7
19.00	2.9	1.8	0.5	0.5	1.1	1.2	0.3	1.1

G. Shielding Improvements

Pilot-B CH scintillators[30] were used for proton detectors; and since (n,p) cross sections are 14 b at .1 Mev, 4 b at 1 Mev, and 1 b at 10 Mev, appreciable background could result from knock-on protons. For this reason the amount of borax-paraffine neutron shielding in the laboratory was greatly increased. This shielding, gradually increased over a period of time, reduced the background by an appreciable factor for E_0 = 30 Mev. Estimates of the background due to (n,p) events can be made with the use of the following assumptions:

(1) The origin of all neutrons in the paraffine beam-stopping material and a mean neutron energy of 6 Mev.

(2) The neutron yields in C measured by Barber and George.[31]

(3) A discriminator cut-off corresponding to the energy loss of a 2-Mev proton.

(4) The same angular distribution for the (γ,n) reaction as for the (γ,p) reaction.

(5) A geometric factor of 1/2 to estimate losses incurred because the range of a 4-Mev proton is the order of the scintillator thickness.

(6) A factor of 2/3 to account for (n,p) events which result in a recoil proton with energy greater than 2 Mev.

(7) Target-cave and target-scintillator distances of 8 and 4.8 ft, respectively.

Making these assumptions, we calculate $4 \times 10^{-13} (1 - .88 \cos\theta + .40 \sin^2\theta)/(1 - .88 \cos\theta)^2$ counts per electron, where θ is the angle

between the spectrometer and electron beam, were produced by knock-ons in the unshielded scintillators. The average .003-in. Al proton-counting rate was approximately 5×10^{-13}/electron at 76°, compared to the 6×10^{-13} to be expected from (n,p) events without shielding.

Preliminary runs, with the spectrometer shielding of 20 in. of borated paraffine, 4 in. of lead, and 2 in. of iron in place, indicated that a larger component of the ambient background (background not originating in the target area) was a function of spectrometer angle than predicted by the above calculation. Therefore, an additional 4-in. Pb shielding-wall was built along the output-wall of the cave housing the achromatic beam-translation system and the former collimator shielding-wall was moved nearer the collimator[23] and thickened. It was experimentally determined that the scraping slits located about two feet in front of the second magnet added appreciably to the background counting rate, and in an especially noxious way, the background rate not being strictly a function of the SEM beam current, but a slight function of accelerator tune-up conditions; therefore, these slits were retracted. Probably the largest contribution to background reduction was the construction of a beam-stopping cave with walls composed of two 1-ft-thick layers of a borax and paraffine mixture separated by a 4-in. layer of lead.

CHAPTER III

EXPERIMENTAL RESULTS AND DISCUSSION

A. Excitation and Energy Distribution Experiments

In most cases we interpreted our (e,pe') excitation-experiment data by assuming that only E-1 transitions are important in the giant-resonance region. As mentioned previously, the electron virtual-photon spectrum, unlike the real-photon spectrum, depends on the multipole order of the transition induced. Consequently reaction multipolarities could theoretically be determined by electron-excitation experiments alone and the validity of the assumption of only E-1 transitions in the giant resonance region investigated; however, in practice, the electron-excitation method of multipolarity determination is difficult. In particular, electron-induced E-1 and M-1 transitions can be separated and identified only if the (γ,p) branching ratios to excited states, and the fractional errors resulting from yield counting statistics are $\ll 2/[(\omega/\omega' + \omega'/\omega)\lambda - 2]$ — since the E-1 and M-1 virtual-photon spectra are approximately proportional to $(\omega/\omega' + \omega'/\omega)\lambda - 2$ and $(\omega/\omega' + \omega'/\omega)\lambda$, respectively [$\lambda$ is defined in Eq. (4)] — and if higher multipoles do not become important at electron energies high enough to satisfy this criterion.

In addition, $\langle f|\vec{J}(\vec{k},k_0)|i\rangle$, the matrix element of the current operator between initial nuclear and final nuclear-nucleon states, is evaluated for $|\vec{k}| = [p^2 + p'^2 - 2pp' \cos\theta]^{1/2}$ in electron-induced transitions and for $|\vec{k}| = \Delta\omega$, the energy transfer, in photon-induced transitions. Deviations of the ratio of the square of $\langle f|\vec{J}(\vec{k},k_0)|i\rangle$, evaluated for those values

of $|\vec{k}|$ which are effective in electron-induced transitions, to the square of $\langle f|\vec{J}(\vec{k},k_0)|i\rangle$, evaluated for the value of $|\vec{k}|$ which is effective in photon-induced transitions, from unity must be small for the above considerations to apply. The stacked foil experiments of Barber[32] have shown this to be a good approximation for C^{12} for electron energies below ~ 60 Mev.

Experimental instabilities partially nullified the accumulation of enough counting statistics and, in most cases, excited-state branching ratios appeared to be too large to satisfy the above criterion. Therefore, we assumed E-1 excitation and interpreted deviation of the proton yield from an E-1 isochromat as attributable to an additional E-1 transition in which the residual nucleus was left in an excited state. Usually a definite break in the yield curve occurred when deviations were observed; and, since the general E-1 character of the giant resonance is alleged to be well established, the above assumption is highly plausible. However, our results do not exclude the possibility of other than E-1 excitation in isolated proton peaks..

Furthermore, the correct virtual-photon spectrum is also dependent on the angle between the primary electron beam and the reaction product, as explained in the Introduction (Chapter I), in contrast to the theories of Dalitz and Yennie[17] and especially Blair,[33] which was specially derived for application to stacked-foil experiments where the experiment integrates over both reaction-product and scattered-electron directions. The fractional error made in applying the Blair E-1 virtual-photon spectrum to the reaction product observed at an angle θ_q is

$$\frac{(\omega'/\omega)(1 - \frac{3}{2}\sin^2\theta_q)\beta(E)}{[\alpha(E) + \beta(E)\sin^2\theta_q][(\omega/\omega' + \omega'/\omega)\lambda - 2] + (\omega'/\omega)(1 - \frac{3}{2}\sin^2\theta_q)\beta(E)} , \quad (17)$$

where $\alpha(E)$ and $\beta(E)$ are defined in Eq. (2). In the case where $\alpha(E) \ll \beta(E)$, such as the D (γ,p)n, large deviations could occur; but for the elements of this experiment the maximum error is 4%, which is probably smaller than arises from the assumption of only E-1 transitions. Therefore, the reaction product angle-independent approximation to the E-1 virtual-photon spectrum was used at 76°, where energy distribution and excitation experiments were executed.

Multiple scattering of the incident electron beam altered the E-1 virtual-photon, differential spectrum negligibly and was not a cause of error, the reaction-product, angle-independent differential spectrum being transformed from

$$\frac{2m^2 k_0^2}{(k_0^2 - \vec{k}^2)^2} + \frac{\omega^2 + \omega'^2}{k_0^2 - \vec{k}^2} - \frac{1}{2}$$

to

$$\frac{2m^2 k_0^2}{(k_0^2 - \vec{k}^2)^2}\left[1 \quad \frac{\sigma^2}{2} \quad \frac{1 + \cos^2\frac{\theta}{2}}{\sin^2\frac{\theta}{2}}\right] + \frac{\omega^2 + \omega'^2}{k_0^2 - \vec{k}^2}\left[1 + \sigma^2\cos^2\frac{\theta}{2}\right] - \frac{1}{2} ,$$

$$\sigma \ll \theta ,$$

where θ is the angle between incident and scattered electron, and σ is the rms multiple-scattering angle.

3.1 Oxygen. Our experimental results for the O (e,pe') yield (Fig. 8), with an initial electron energy E = 30 Mev, are in essential agreement

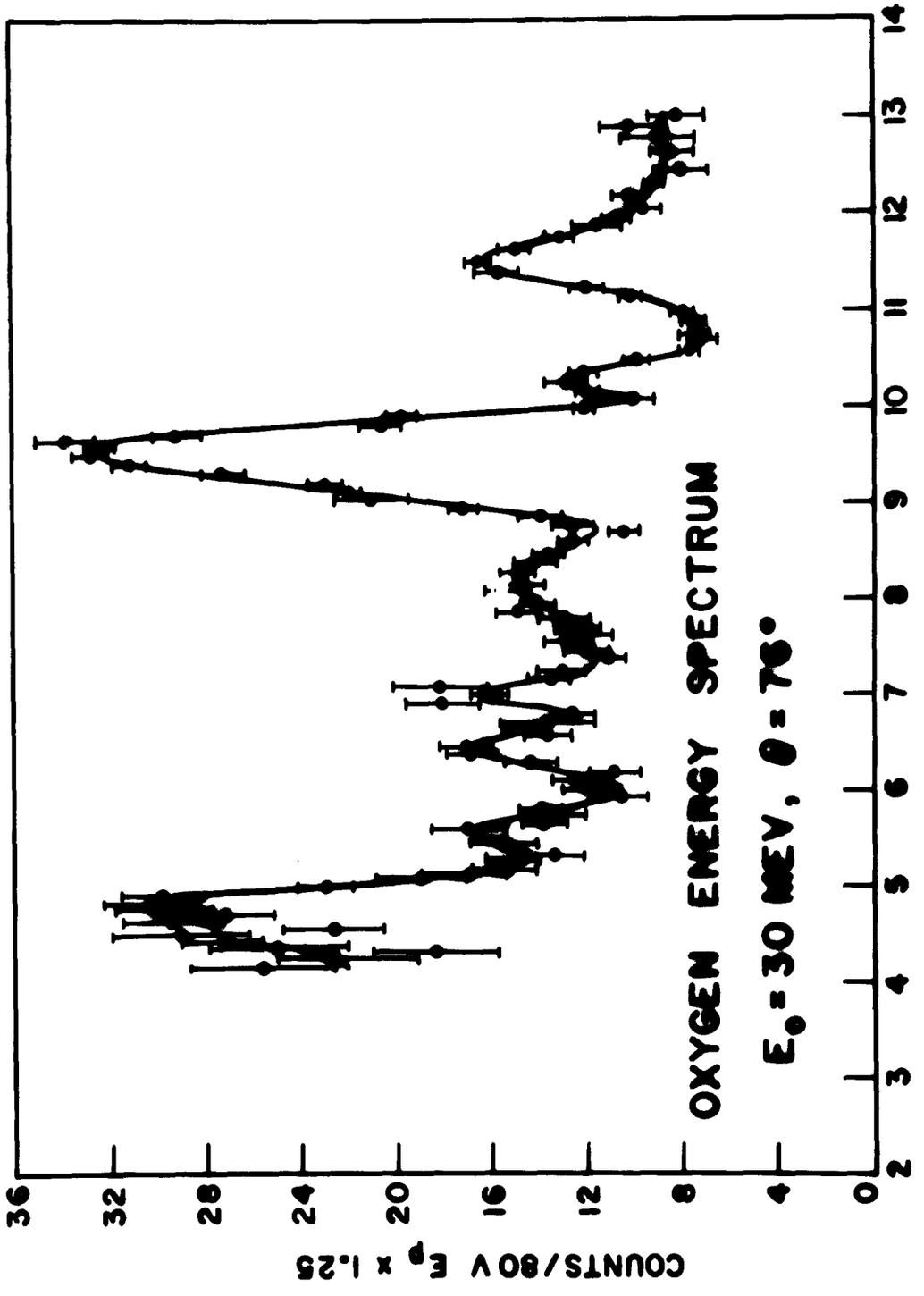
OXYGEN ENERGY SPECTRUM
E_o = 30 MEV, θ = 75°
COUNTS/80V E_p x 1.25
PROTON ENERGY (MEV)
0
4
8
12
16
20
24
28
32
36
2
3
4
5
6
7
8
9
10
11
12
13
14

FIGURE 8

with the gross features of earlier[34] and contemporary[14] (γ,p) work, although our superior resolution and counting statistics enabled us to resolve a small peak at 10.25 Mev on the high-energy side of the large resonance at 9.53 Mev, usually alleged to be the O giant resonance. The energy spectrum at 48° (Fig. 9) confirms the existence of this small peak and extends the spectrum to a proton energy of 14 Mev, showing the smooth yield decrease above the 11.50-Mev peak. Peaks occur at proton energies of 4.85, 5.60, 6.45, 7.00, 8.30, 9.53, 10.25, and 11.50 Mev, corresponding, in the case of ground-state transitions, to photon energies of 17.27, 18.07, 18.99, 19.57, 20.65, 22.30, 23.10, and 24.35 Mev. Geller[35] has applied second-order difference analysis of the bremsstrahlung yields to the O^{16} (γ,n) reaction and obtained peaks at 18.11, 18.91, 19.60, 20.70, and 22.4 Mev, the first three consecutive, the last two intersticed between other peaks of unspecified widths. The agreement between peaks in $\sigma(\gamma,p)$ of our experiment and $\sigma(\gamma,n)$ as derived by Geller provides support for charge symmetry of nuclear forces. The $\sigma(\gamma,n)$ of Milone *et al.*[36] at a bremsstrahlung endpoint energy of 31 Mev is not in agreement with our proton spectra; but because of the statistics of the (γ,n) experiment the difference is probably not significant.

Excitation of the 9.58-Mev O protons (Fig. 10) indicates ground-state transitions up to an excitation energy of 31.8 ± .5 Mev, above which approximately 8% of the proton yield leaves the residual nucleus N^{15} with 9.5 ± .5 Mev of excitation. Extreme single-particle photonuclear theory[37] requires N^{15} to be left in a state of negative parity and spin 3/2 or 1/2. N^{15} levels with unassigned spin and parity exist at 9.16 and

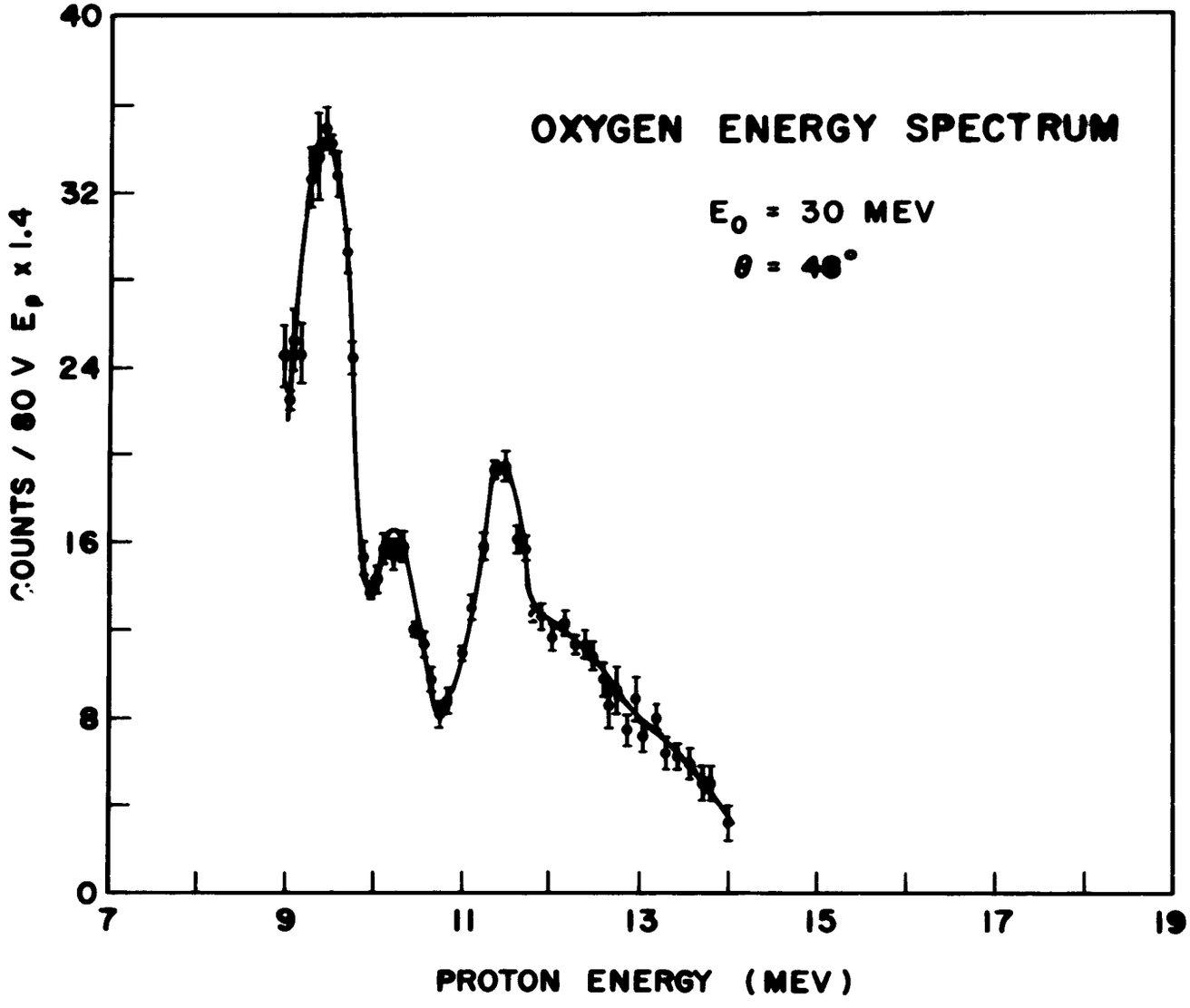
OXYGEN ENERGY SPECTRUM
E_0 = 30 MEV
θ = 40°
COUNTS / 80 V E_p x 1.4
PROTON ENERGY (MEV)
0
8
16
24
32
40
7
9
11
13
15
17
19

FIGURE 9

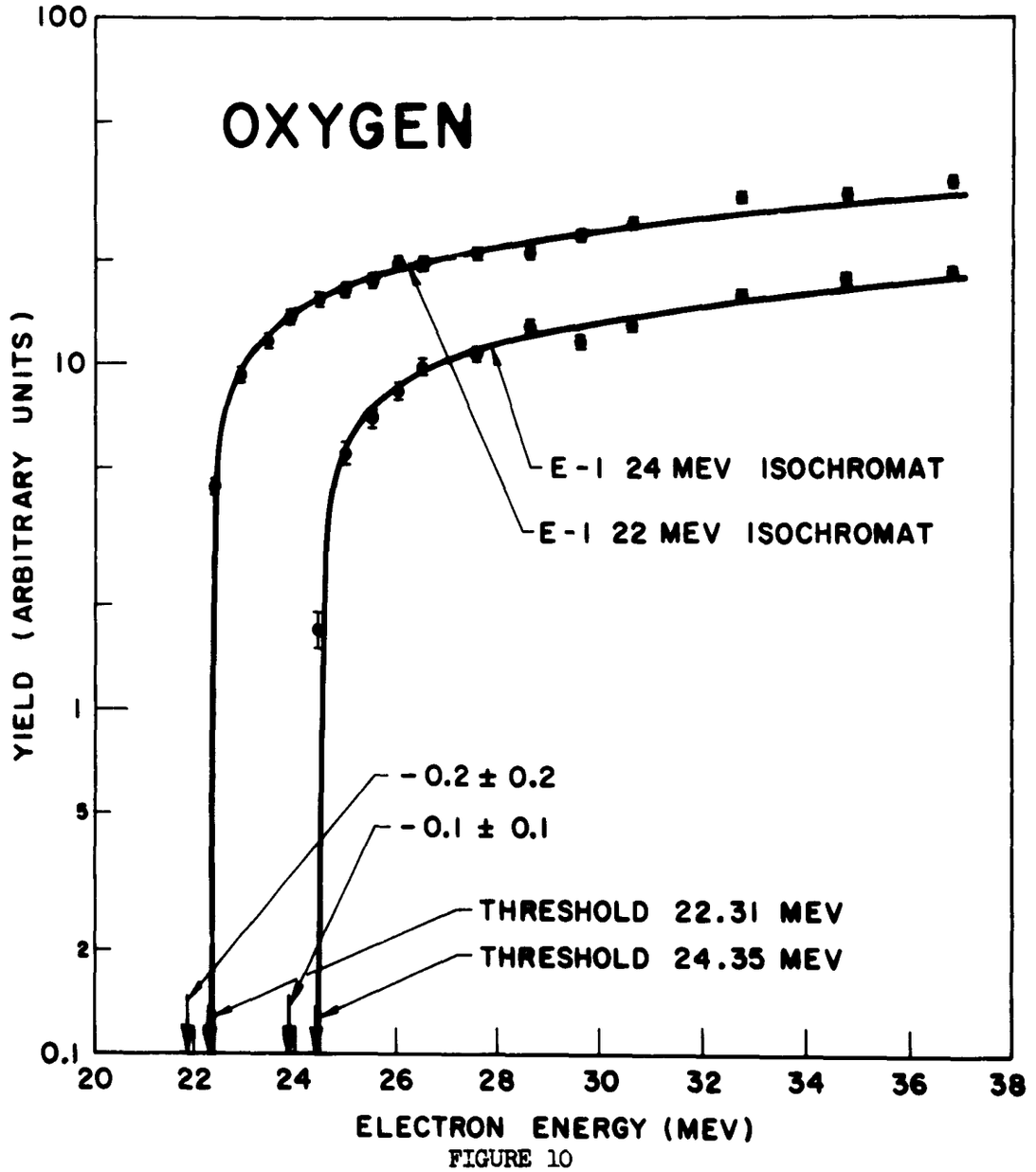
OXYGEN
100
10
1
5
2
0.1
YIELD (ARBITRARY UNITS)
E-1 24 MEV ISOCHROMAT
E-1 22 MEV ISOCHROMAT
-0.2 ± 0.2
-0.1 ± 0.1
THRESHOLD 22.31 MEV
THRESHOLD 24.35 MEV
20
22
24
26
28
30
32
34
36
38
ELECTRON ENERGY (MEV)
FIGURE 10

and 9.81 Mev,[38] and consequently single-particle excitation implies one or both of these levels should be $1/2^-$ or $3/2^-$. Unfortunately the counter system straddled the 10.25-Mev proton peak during excitation experiments; but the straddling counters at 10.00 and 10.55 Mev (Fig. 11) indicated ground-state transitions for excitation energies up to approximately 33 Mev for the 10.00-Mev protons, and approximately 30 ± .5 Mev for the 10.55-Mev group, with about a 25% branching ratio to the 6.33 Mev $\leq 5/2^-$ state of N^{15}. However, these counters were on steep portions of the energy distribution and small diurnal spectrometer-field instabilities could have produced large errors in the yield. The 11.50-Mev proton yield (Fig. 10) follows a 24.4-Mev isochromat in the range of excitation energies of this experiment, corresponding to ground-state transitions. The 12.33-Mev protons also leave N^{15} in the ground state (Fig. 12) with slight evidence for excited-state transitions for electron bombarding energies above 34 Mev. Table IV summarizes the excitation characteristics of the 0 protons for E_p greater than 9.53 Mev.

Excitation functions at proton energies lower than 7.5 Mev could have clarified the synthesis of data of other experimental workers by Fuller and Hayward[39] who conjectured that a large fraction of these lower-energy protons were produced by the absorption of photons in the region of 25.2 Mev with the residual nucleus N^{15} left in an excited state. Experimental running-time limitations precluded low-energy proton excitation experiments; but the data synthesized in reference 39 can be combined with ours to place qualitative limits on the ratio of $(d\sigma/d\Omega)_{76°}$ at photon energies of 22.4 and 25.3 Mev. The unlikely assumption that the entire

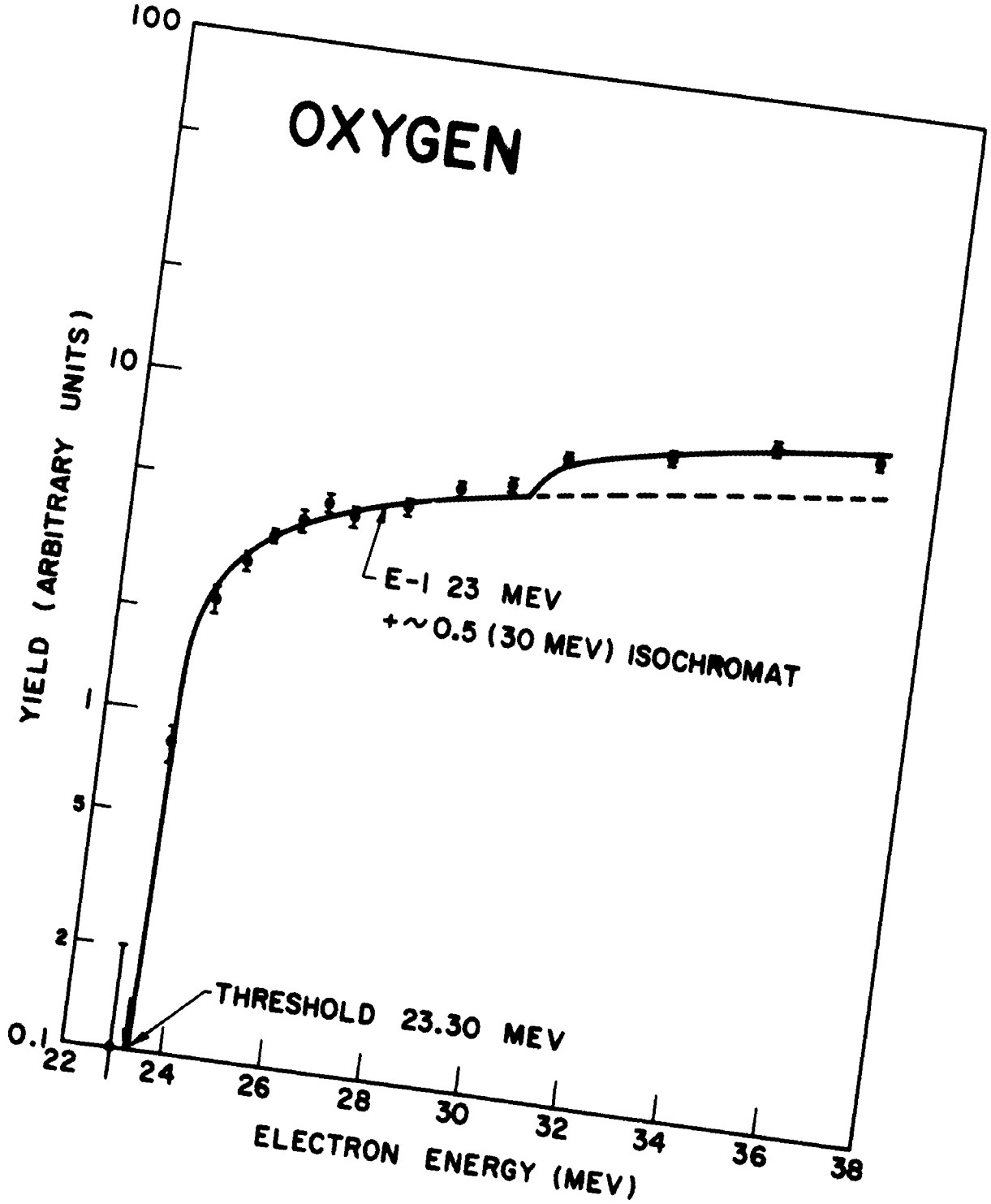
OXYGEN
YIELD (ARBITRARY UNITS)
100
10
1
5
2
0.1
E-1 23 MEV
+~0.5 (30 MEV) ISOCHROMAT
THRESHOLD 23.30 MEV
22
24
26
28
30
32
34
36
38
ELECTRON ENERGY (MEV)

FIGURE 11

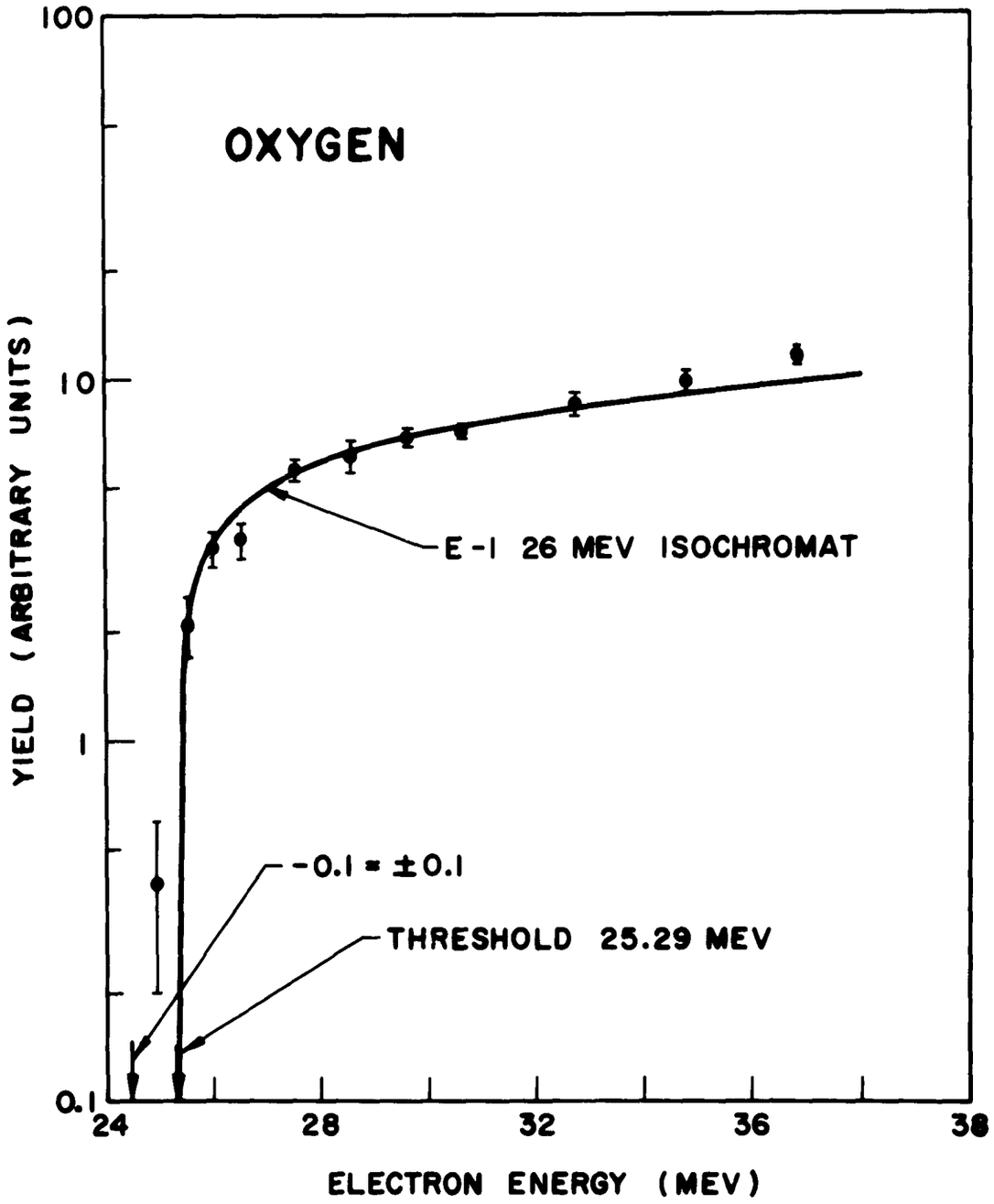
OXYGEN
100
10
1
0.1
YIELD (ARBITRARY UNITS)
E-I 26 MEV ISOCHROMAT
-0.1 = ±0.1
THRESHOLD 25.29 MEV
24
28
32
36
38
ELECTRON ENERGY (MEV)

FIGURE 12

TABLE IV. Summary of the excitation characteristics of the O protons for $E_p > 9.53$ Mev.

Proton energy (Mev)	Ground state transition energy (Mev)	Electron energy at which a deviation from an E-1 isochromat occurs (Mev)	Branching ratio (%)	Energy of excited state (Mev)
9.58	22.31	31.8 ± .5	8 ± 8	9.5 ± .5
10.55	23.30	30.0 ± .5	25 ± 10	6.7 ± .5
11.49	24.35	——	——	——
12.33	25.29	34.0	——	——

yield of protons in the 7.3-Mev region is attributable to transitions with the N^{15} left in an excited state leads to an upper limit for the ratio of 1:1. This ratio is insensitive to exactly which excited states are fed because of the relatively flat yield in the region in which the final-state properties of the proton are uncertain. The conclusions above are only valid if none of the protons with $E_p < 5$ Mev are produced by the absorption of 25.2-Mev photons.

The proton radiative capture reaction on N^{15} has been studied by Thomas et al.[40] in the photon-energy range of 17.0 to 19.7 Mev, and by Cohen et al.[41] for photon energies between 21 and 26 Mev. Discrepancies between the detailed shapes of the experimental (γ,p_0) and (p_0, γ) cross sections do exist, particularly for photon energies in the region of 25 Mev; but elsewhere, except for relative peak size differences, the agreement is fair when the proton energies of the direct reaction are multiplied by the kinematic factor of $(A/A-1)^2 = 1.139$ needed for comparison with proton energies of the capture reaction. Detailed balance predicts

$$\left(\frac{d\sigma}{d\Omega}\right)_{\gamma,p_0} = 4M_p c^2 \frac{E_{p_0}}{E_\gamma^2} \left(\frac{d\sigma}{d\Omega}\right)_{p_0,\gamma} , \qquad (18)$$

for 0, from which Cohen et al. obtained for the 9.53-Mev peak $(d\sigma/d\Omega)_{\gamma,p_0}$ = 14 mb/4π sr = 1.12 mb/sr at 90°, to be compared with our 1.32 mb/sr.

The integrated cross sections and widths of an approximate resonance-curve fit to the data for $22 < E_\gamma < 25$ Mev are given in Table V. The difficulty in fitting a single resonance curve to the region around 22.3 Mev, and the appearance of a slight inflection on the lower-energy side

TABLE V. Parameters of an approximate resonance curve fit to the O cross section for $22 < E_\gamma < 25$ Mev.

Proton energy of peak (Mev)	Photon energy of peak (Mev)	Peak height at 76° (mb/sr)	Photon width at half-height (Mev)	$\int \sigma(\gamma,p)dE_\gamma$ under resonance curve (Mev-mb)	$\% \int_{16.7}^{27} \sigma(\gamma,p)dE_\gamma$
9.53	22.3	1.29	0.70	14.4	26.2
10.25	23.1	0.27	0.32	1.7	3.1
11.50	24.35	0.78	0.87	10.9	19.7
				Total 27.1	49.0

of this peak suggest unresolved structure. To unfold the contributions of the finite spectrometer resolution and the finite electron-beam width to the intrinsic width of the peaks, we geometrically subtracted twice $\Delta p/p$, which is nonrelativistically $\Delta E/E$, as given by the full width at half-maximum height of the Cm^{244} α-particle momentum spectrum ($\Delta E = .024E$ for counter 7; Fig. 2) and alegbraically subtracted the proton energy loss in an electron-beam width of the gas (at experimental TP). For the latter correction we assumed a uniform electron-beam intensity distribution which overestimated the resolution degradation produced by finite electron-beam width. With the use of these crude estimates, we find the intrinsic photon widths of the peaks described in Table V to be .62, .17, and .79 Mev, respectively.

The assumption that only O^{16} (γ,p) transitions occur which leave N^{15} in the ground state for excitation energies up to 30 Mev leads to the differential cross sections at 76° and 48° shown in Figs. 13 and 14. We obtained for O^{16}

$$\int_{16.6}^{27} \frac{d\sigma}{d\Omega}(\gamma,p)dE_\gamma = 5.4 \pm 1.1$$

Mev-mb/sr at 76°, or

$$\int_{16.6}^{27} \sigma(\gamma,p)dE_\gamma = 56 \pm 11 \qquad (19)$$

Mev-mb, assuming our angular distributions. For O^{16} $\int^{31} \sigma(\gamma,n)dE_\gamma$, Fuchs and Salander[42] obtained 61 ± 7 Mev-mb, while Carver and Lokan[43] obtained 46 ± 7 Mev-mb. These values of $\int \sigma(\gamma,p)dE_\gamma$ and $\int \sigma(\gamma,n)dE_\gamma$ for O are not in serious conflict with the requirements of charge symmetry.

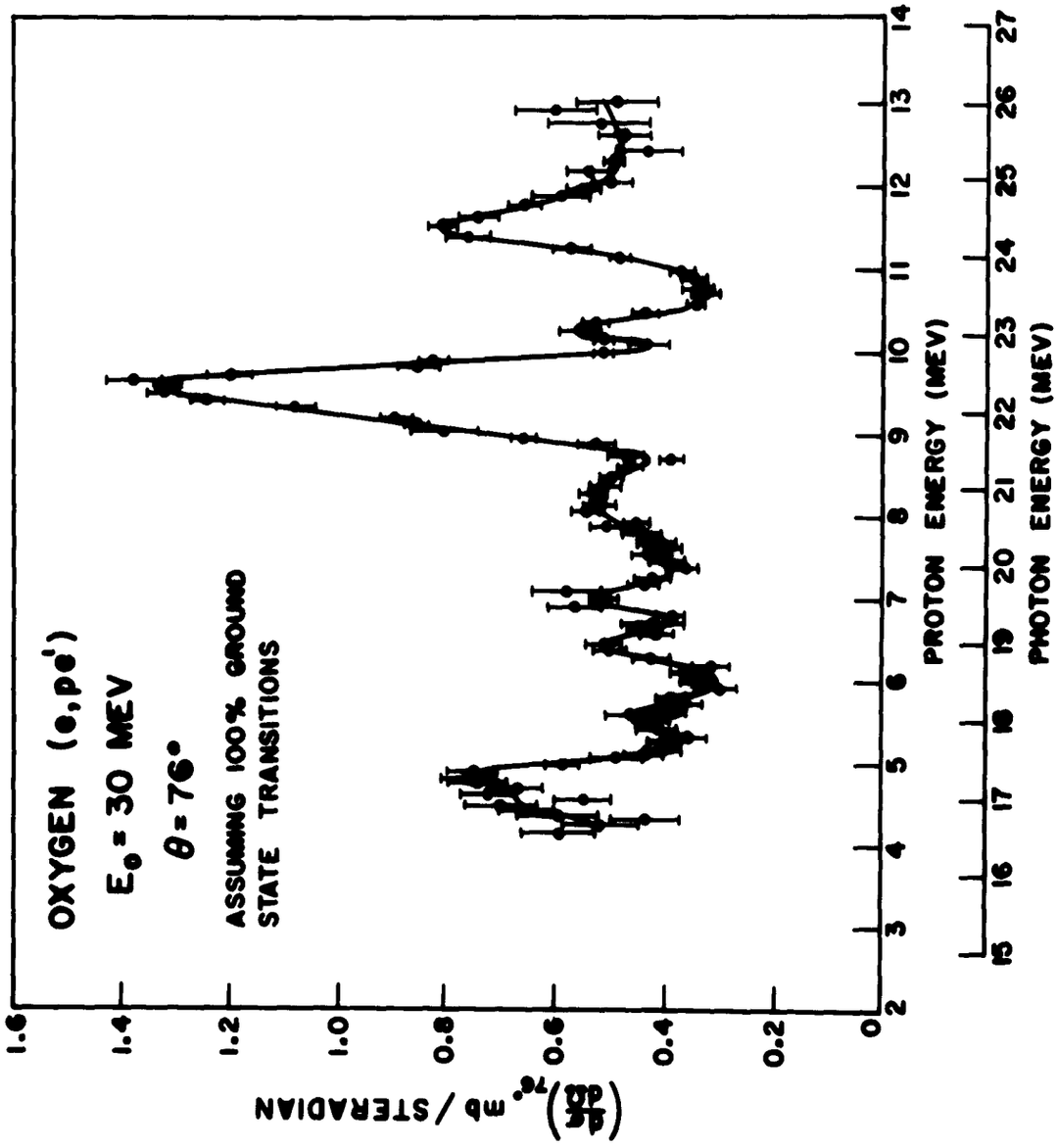
OXYGEN (e,pe')
E_0 = 30 MEV
θ = 76°
ASSUMING 100% GROUND STATE TRANSITIONS
$\left(\frac{d\sigma}{d\Omega}\right)_{76°}$ mb / STERADIAN
PROTON ENERGY (MEV)
PHOTON ENERGY (MEV)

FIGURE 13

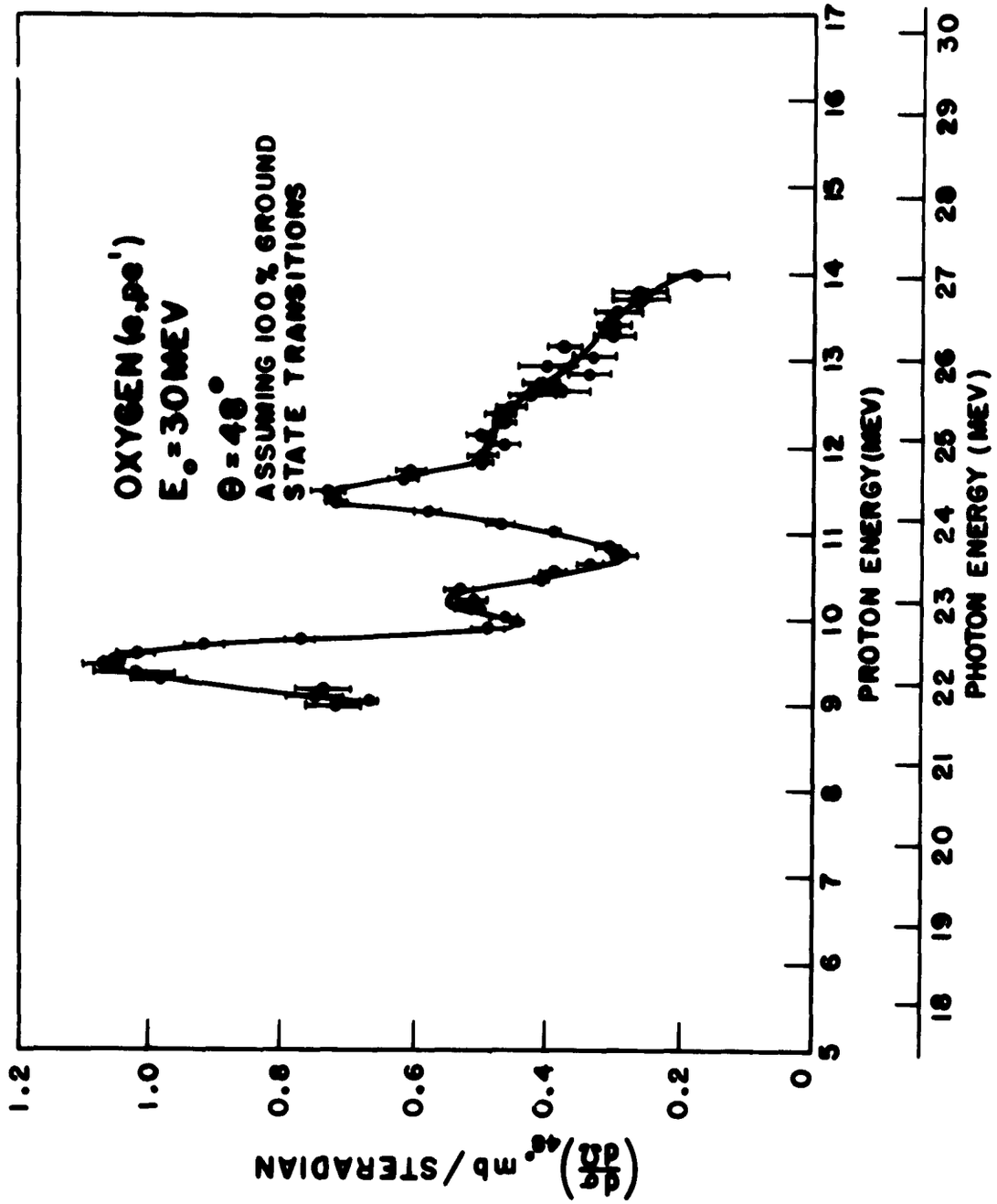
OXYGEN (α,pγ₀)
E_α = 30 MEV
θ = 48°
ASSUMING 100% GROUND STATE TRANSITIONS
(dσ/dΩ)_48° mb/STERADIAN
0
0.2
0.4
0.6
0.8
1.0
1.2
5
6
7
8
9
10
11
12
13
14
15
16
17
PROTON ENERGY (MEV)
18
19
20
21
22
23
24
25
26
27
28
29
30
PHOTON ENERGY (MEV)

FIGURE 14

3.2 Fluorine. The F proton energy spectrum was investigated at three initial electron energies, 18, 24.5. and 30 Mev (Figs. 15 and 16). The 24.5-Mev data contain statistically significant peaks at 3.25, 3.7, 4.5, and 7.3 Mev (ground-state-transition photon energies of 11.42, 11.90, 12.74, and 15.70 Mev), while less reliable evidence exists for a considerable amount of fine structure. The 30-Mev spectrum confirms the essential features of the 24.5-Mev spectrum and contains additional structure at higher proton energies, in particular a peak at 10.1 Mev (ground-state transition energy 18.7 Mev). While the large statistical errors of previous F (γ,p) work vitiate a detailed comparison with our results, the agreement in proton energies of the peaks is good. Forkman and Wahlström[44] observed peaks at photon energies of 11.4, 11.9, 12.8, 13.6, 15.4, and 18.1 Mev. The F $\sigma(\gamma,n)$ has not been made with the refined techniques of Geller,[35] but breaks do occur in the F (γ,n) activation curves at 11.5, 11.9, 12.2, and 15.3 Mev.[45,46]

No excitation experiments were undertaken per se, but the three energy spectra can give semi-quantitative final-state information. The yields of the 7.25-Mev F protons at E_0 = 18, 24.5 and 30 Mev are in the proportion of $1/(3.4 \pm .4)/(5.9 \pm .8)$; while E-1 virtual-photon spectra at these electron energies computed for a momentum transfer corresponding to a transition in which O^{18} is left in the ground state are in the proportion of 1/1.81/3.48. The experimental yield ratio for electron energies of 30 and 24.5 Mev is $1.7 \pm .3$, while the E-1 virtual-photon spectra predict a ratio of 1.93. This indicates to first order that the important transitions for 7.25-Mev protons are those in which the residual

nucleus O^{18} is left in the ground state or in an excited state with less than 6 Mev of excitation energy. This situation seems to prevail in the energy range where data at the three excitation energies are available. The differential cross section at 76°, derived by making the erroneous assumption of 100% ground-state transitions for illustrative purposes, is given in Fig. 17. The 0^+ ground state, 2^+ 1.98-Mev level, and 4^+ 3.55-Mev level in O^{18} belong to the $d^2_{5/2}$ valence nucleon configuration in the shell model scheme and thus not expected to be greatly populated by the photonuclear effect, which according to Wilkinson[10] involves predominantly excitation of the closed shell or core nucleons. Several 1^- O^{18} levels below 6 Mev exist which could correspond to hole states of the O^{16} core, but branching ratios to these plausible levels were not determined by our experiment. Therefore, confidence cannot be attached to either the detailed shape of the cross section or to its magnitude. However, the assumption of 100% ground-state transitions for a proton spectrum with a constant branching ratio x to an excited state of energy E^* and a sensibly energy-independent yield in the energy range considered produces a fractional error in the cross section of approximately

$$x \left[1 - \frac{k - E^*}{k} \frac{N_{E-1}(k,\omega)}{N_{E-1}(k-E^*,\omega)} \right],$$

where the notation is standard. This is $\sim$ [illegible] for F, assuming $x = .5$ and $E^* = 4$ Mev. Thus even for the observed F yield curve the error in the integrated cross section is not much greater than 20% due to final

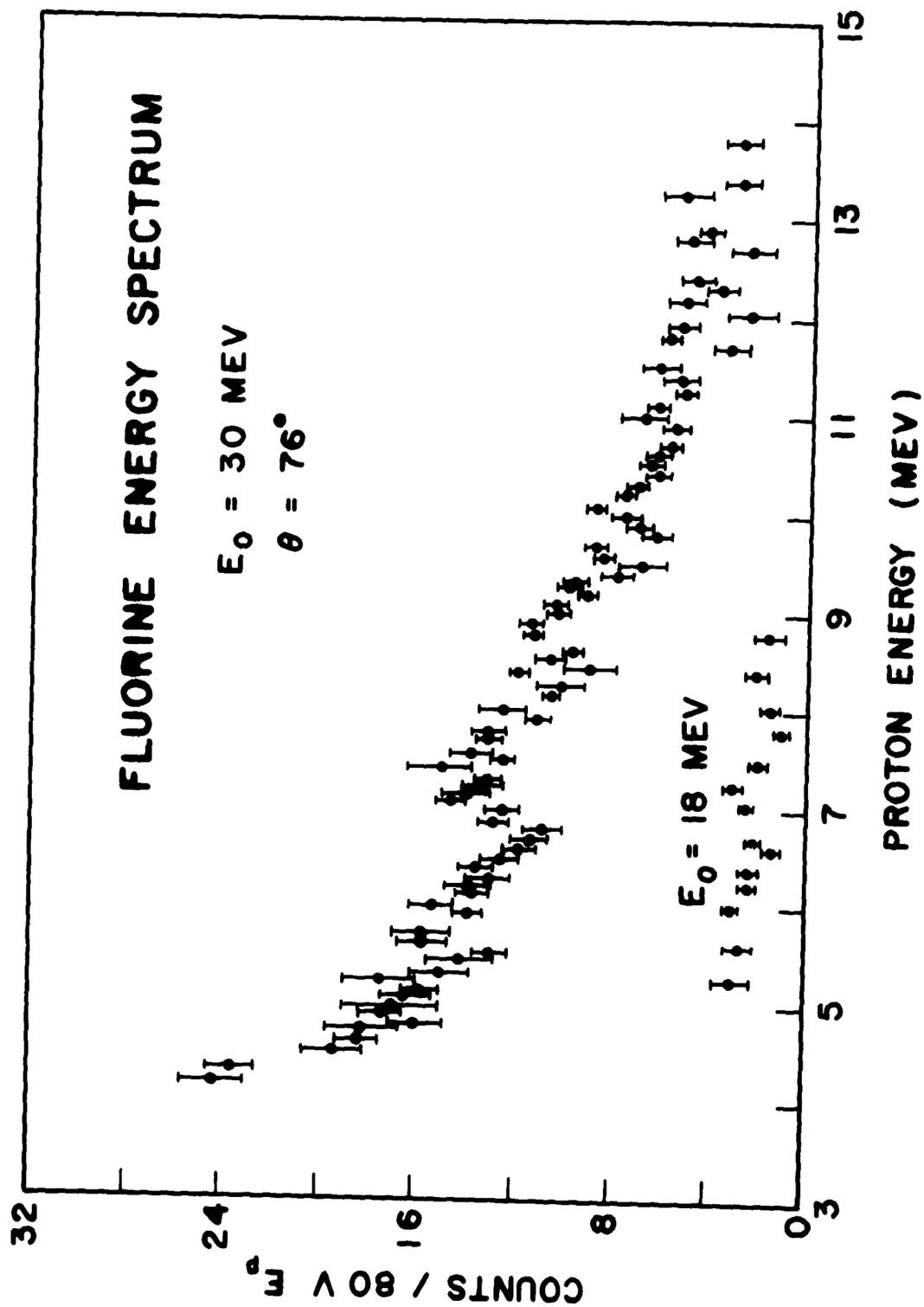
FLUORINE ENERGY SPECTRUM
E_0 = 30 MEV
θ = 76°
E_0 = 18 MEV
COUNTS / 80 V P_a
PROTON ENERGY (MEV)
0
8
16
24
32
3
5
7
9
11
13
15

FIGURE 15

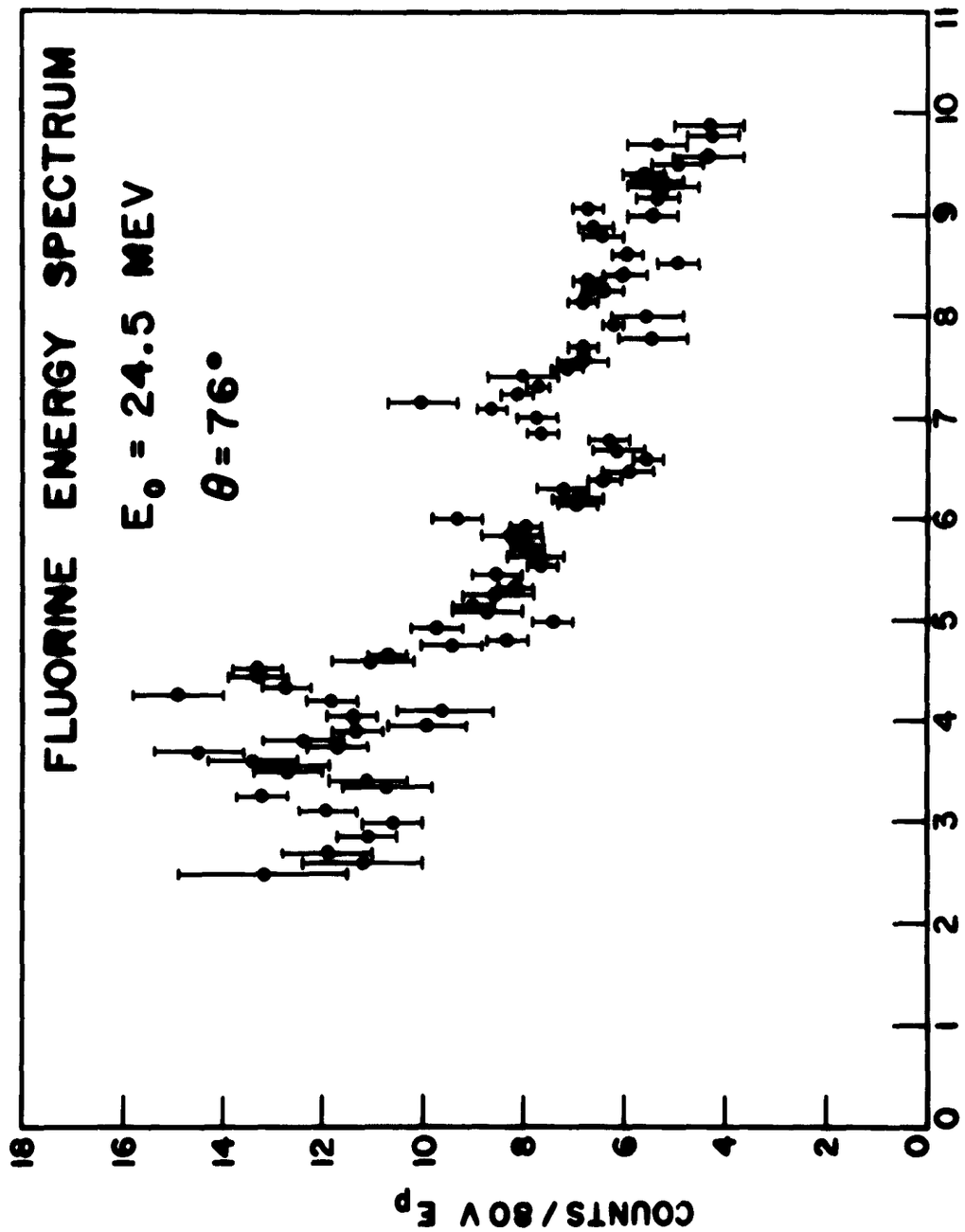
FLUORINE ENERGY SPECTRUM
E_0 = 24.5 MEV
θ=76°
COUNTS / 80 V E_p
PROTON ENERGY (MEV)
0
2
4
6
8
10
12
14
16
18
0
1
2
3
4
5
6
7
8
9
10
11

FIGURE 16

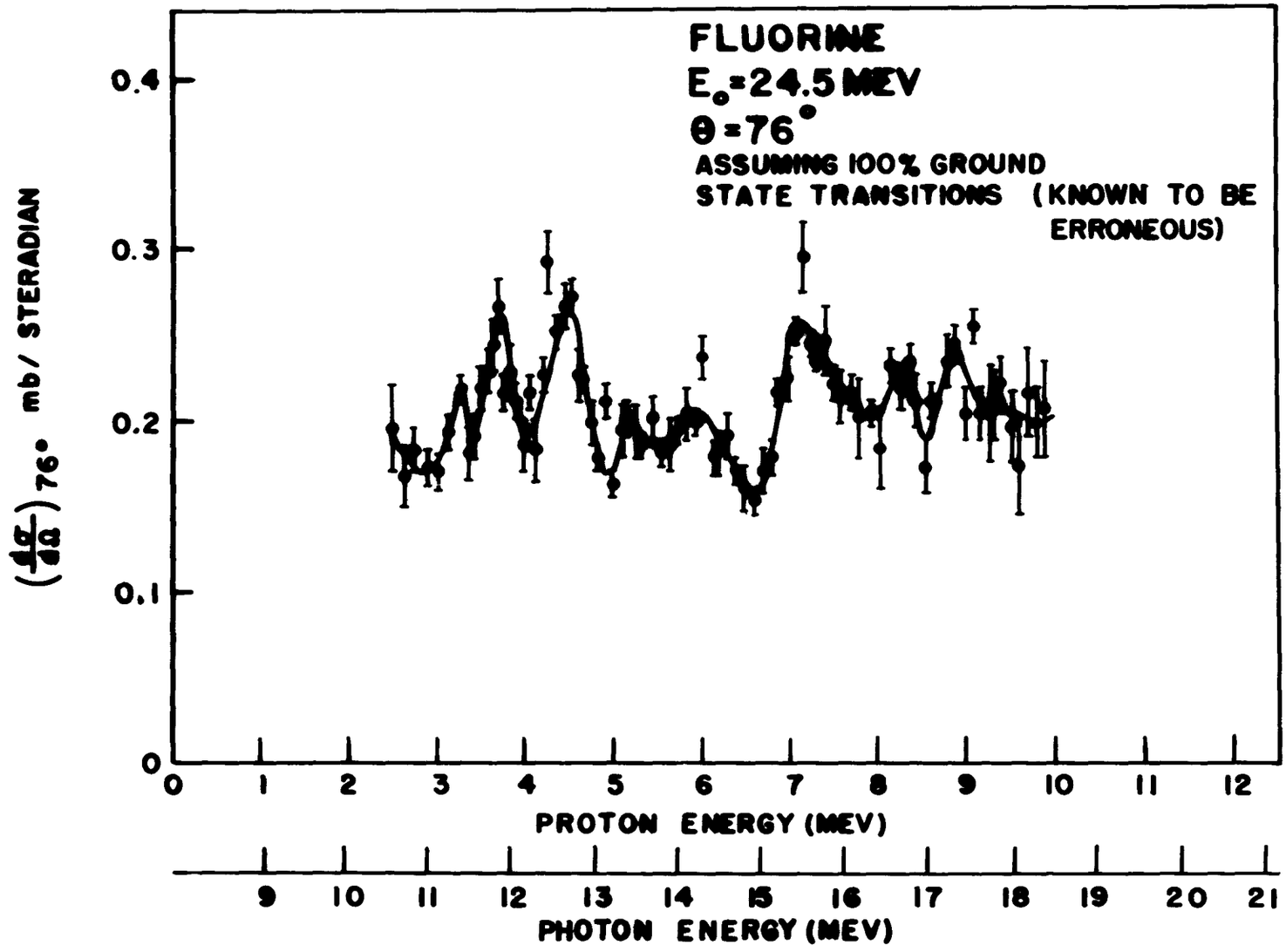
FLUORINE
E₀=24.5 MEV
θ=76°
ASSUMING 100% GROUND
STATE TRANSITIONS (KNOWN TO BE
ERRONEOUS)
(dσ/dΩ)76° mb/ STERADIAN
0.4
0.3
0.2
0.1
0
0 1 2 3 4 5 6 7 8 9 10 11 12
PROTON ENERGY (MEV)
9 10 11 12 13 14 15 16 17 18 19 20 21
PHOTON ENERGY (MEV)

FIGURE 17

state assignment uncertainties with E^* known to be ≤ 6 Mev. Taking these considerations into account, we obtain for F^{19}

$$\int_{10.5}^{23} \sigma(\gamma,p)dE_\gamma = 29^{+9}_{-3} \text{ Mev-mb} \qquad (20)$$

for the assumption of 100% ground-state transitions, and 37 ± 11 Mev-mb for the assumption that all F^{19} (γ,p) transitions leave O^{18} with an excitation energy of 4 Mev. Lasich et al.[47] obtained for F^{19}

$$\int_{10}^{16.5} \sigma(\gamma,p)dE_\gamma \approx 18 \text{ Mev-mb}, \qquad (21)$$

which is compatible with our measurements. G. A. Ferguson et al.[48] obtained for F^{19}

$$\int^{22.2} \sigma(\gamma,n)dE_\gamma = 77 \text{ Mev-mb}. \qquad (22)$$

3.3 Neon. Neon has the most interesting energy spectrum of the elements investigated. The Ne (γ,p) reaction was previously investigated with 23-Mev[49] and 80-Mev[50] bremsstrahlung by cloud-chamber measurements of the recoiling F^{19}, but with apparently inconclusive results regarding the shape of the cross section. Warren and Hay,[51] using monochromatic 17.6-Mev photons from the Li (p,γ) reaction and a Ne-filled proportional counter, obviously observed the low-energy side of the 4.58-Mev peak but lacked sufficient energy to map the full contour of this peak. Gemmell et al.[52] observed the first two peaks in the inverse F^{19} (p,γ_0) Ne^{20} reaction, but the peak widths and energies differ from our work which is in excellent agreement with the inverse reaction done at Oxford.[15] We observe

narrow, symmetric peaks in the Ne-proton energy spectrum at 76° (Fig. 18) at 3.20, 3.70, 4.58, 5.80, 6.65, 7.75, 8.65, 9.40, and 11.40 Mev, whose envelope has the usual giant-resonance shape with a maximum at 4.58 Mev.

Attention was focused on the major proton peaks in the Ne-excitation experiments. Unfortunately, even though the experiments were scheduled so that counting statistics for each point on the excitation curve of the major proton peaks were 3% or less, the experimental results cannot be interpreted unambiguously and all the precautions previously cited are especially pertinent to the analysis of the data. In particular, for the reasons explained earlier in this section, the a priori assumption of only E-1 transitions was made, even though there were isolated cases in which the data seemed to be fit somewhat better by M-1 or E-2 than by E-1 virtual-photon isochromats.

Threshold energy ambiguities arise from three sources: (1) the large primary electron-energy increments of this experiment, (2) the uncertainty in the primary electron-energy calibration, and (3) the interpretational difficulties that poor threshold statistics and finite electron-energy spread (1.5% full-width for all excitation experiments) engender. Because of these difficulties, the important prediction of the independent-particle model that the excited states of the residual nucleus F^{19} predominantly populated by the photoproton reaction should be $1/2^-$ or $3/2^-$ cannot be ascertained by these excitation experiments alone since the $1/2^+$ ground state and $1/2^-$ first excited state are only 110 Kev apart. Presumably, transitions to the other negative-parity states at 1.35 and 1.46 Mev, both with spin 3/2, could be identified.

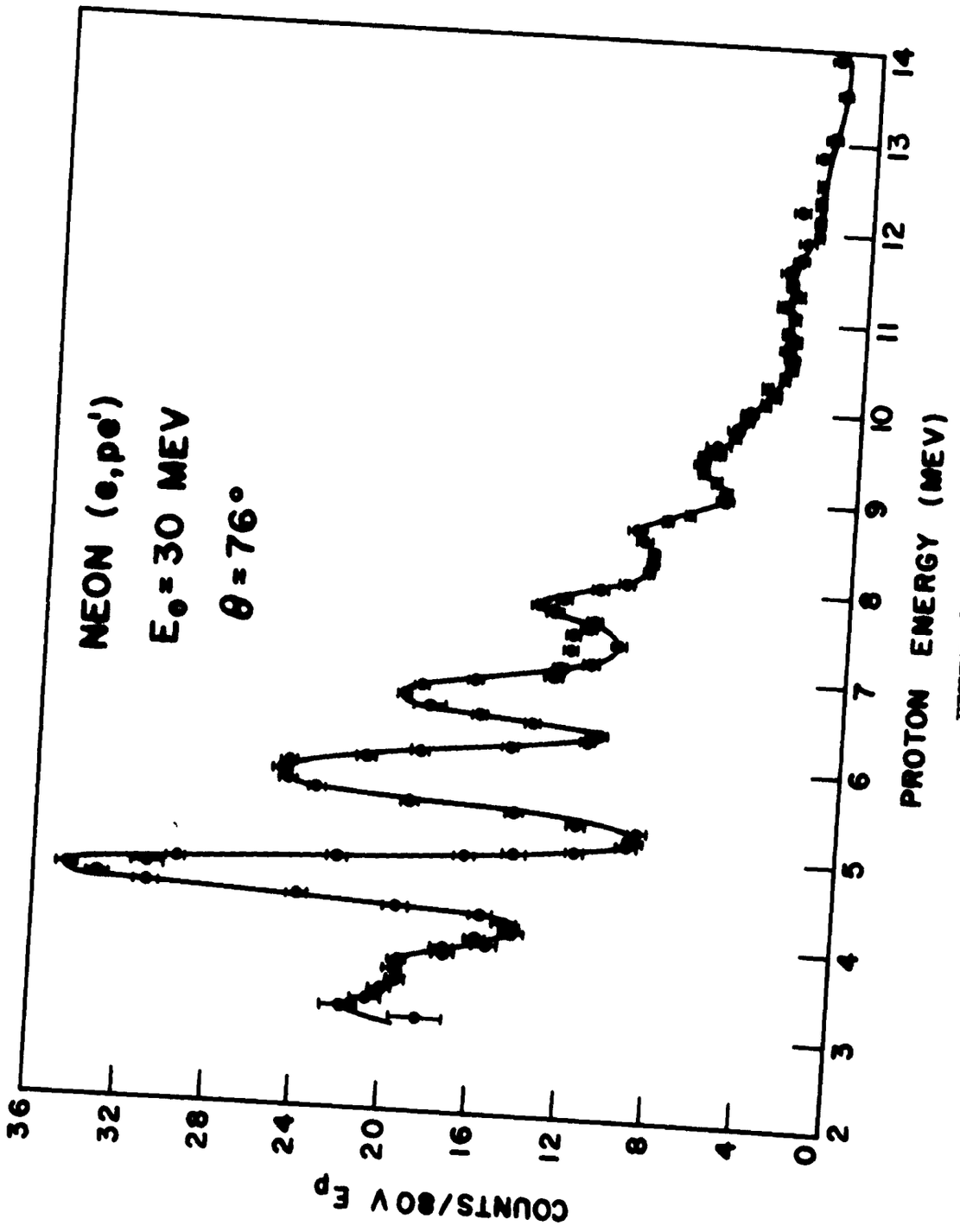
NEON (e,pe')
E_e = 30 MEV
θ = 76°
COUNTS/80 V E_p
PROTON ENERGY (MEV)
0
4
8
12
16
20
24
28
32
36
2
3
4
5
6
7
8
9
10
11
12
13
14

FIGURE 18

The excitation characteristics of the protons from the principal peaks and valleys are displayed in Figs. 19 - 22 , and the salient features summarized in Table VI. The 5.20-Mev protons seem to have a complex parentage with little evidence for ground- or near-ground-state transitions. No excitation experiments were made for the 7.75-Mev peak protons, but since the straddling protons at 7.51 Mev had experimentally identical yield shapes the results were appropriately combined and presented as the excitation of the 7.77-Mev peak protons. All other excitation curves shown are data from at least two counters lying in a proton-energy interval 1.5% wide, with the increased reliability outlined in the experimental section; or were data from a single counter.

The differential cross section at 76°, derived with the assumption of 100% ground-state transitions, is shown in Fig. 23. We obtained for Ne

$$\int_{16}^{27} \sigma(\gamma,p)dE_\gamma = 65^{+13}_{-10} \text{ Mev-mb.} \qquad (23)$$

Thomas and Tanner,[15] using detailed balance and normalizing to the work of Farney et al.[53] obtained 55 Mev-mb from the inverse (p,γ) reaction to the ground state of Ne^{20} over essentially the same proton-energy interval. Normalizing to Gemmell et al.'s[52] inverse reaction cross section, they obtained 140 Mev-mb. The σ(γ,n) measurements of Ferguson et al.[48] had insufficient resolution to observe structure similar to that occurring in the σ(γ,p). The obtained for Ne^{20} $\int^{21.5} \sigma(\gamma,n)dE_\gamma$ = 52 Mev-mb. (Because both the ground and first excited states of F^{19} have spin 1/2, and the relative (γ,p) branching ratios to these states are not known,

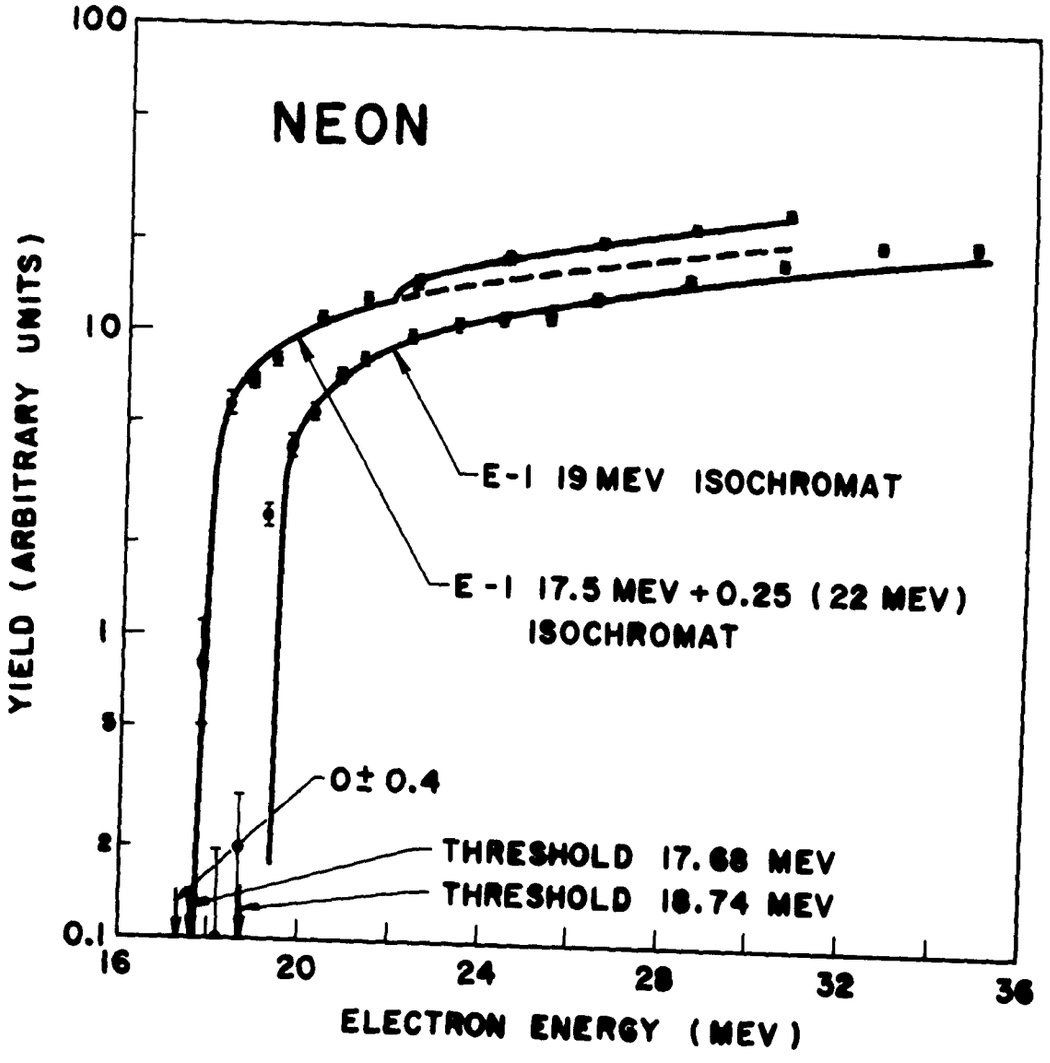
NEON
YIELD (ARBITRARY UNITS)
100
10
1
.5
.2
0.1
16
20
24
28
32
36
ELECTRON ENERGY (MEV)
E-1 19 MEV ISOCHROMAT
E-1 17.5 MEV + 0.25 (22 MEV) ISOCHROMAT
0 ± 0.4
THRESHOLD 17.68 MEV
THRESHOLD 18.74 MEV

FIGURE 19

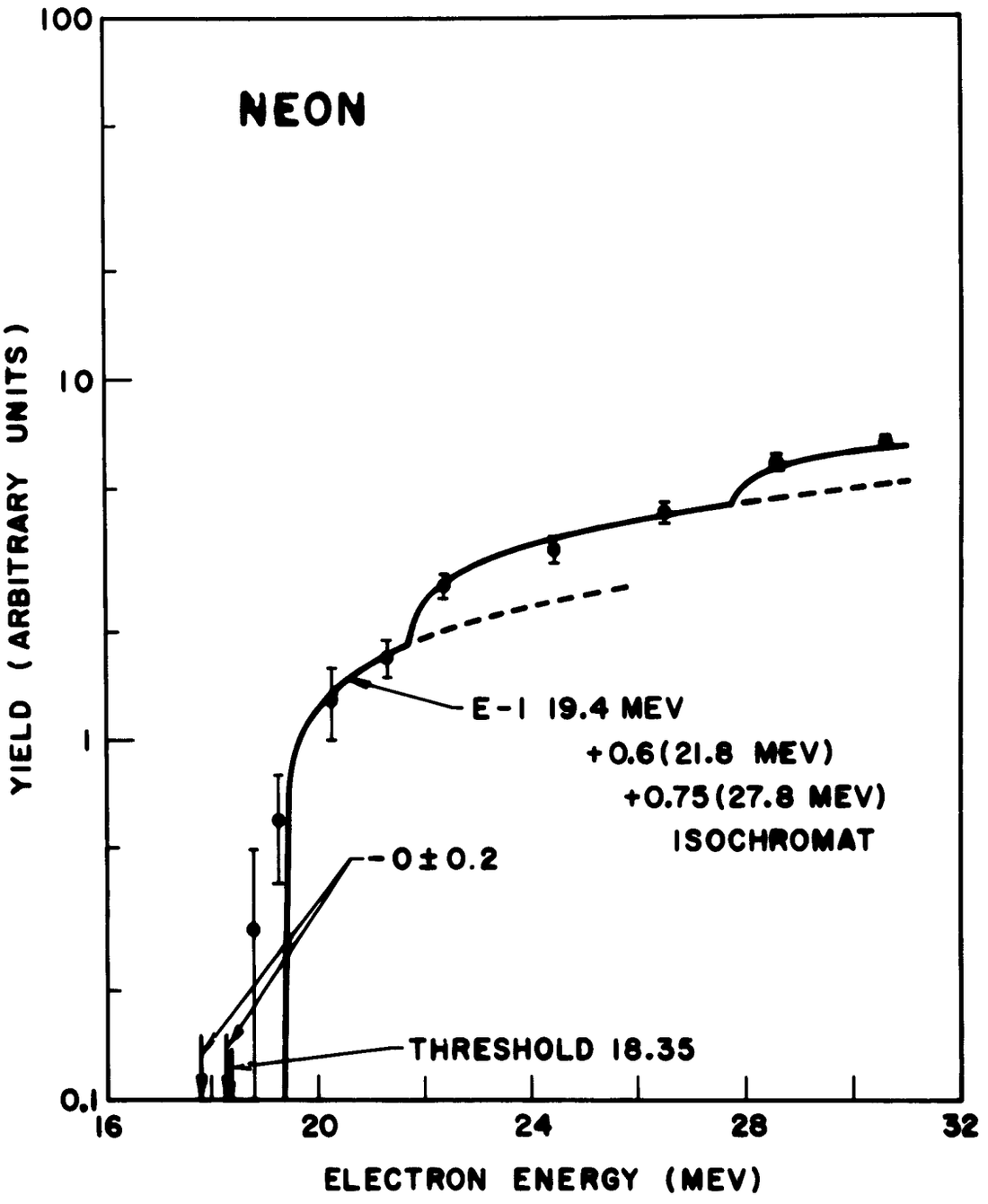
NEON
100
10
1
0.1
YIELD (ARBITRARY UNITS)
16
20
24
28
32
ELECTRON ENERGY (MEV)
E-1 19.4 MEV
+0.6(21.8 MEV)
+0.75(27.8 MEV)
ISOCHROMAT
0±0.2
THRESHOLD 18.35

FIGURE 20

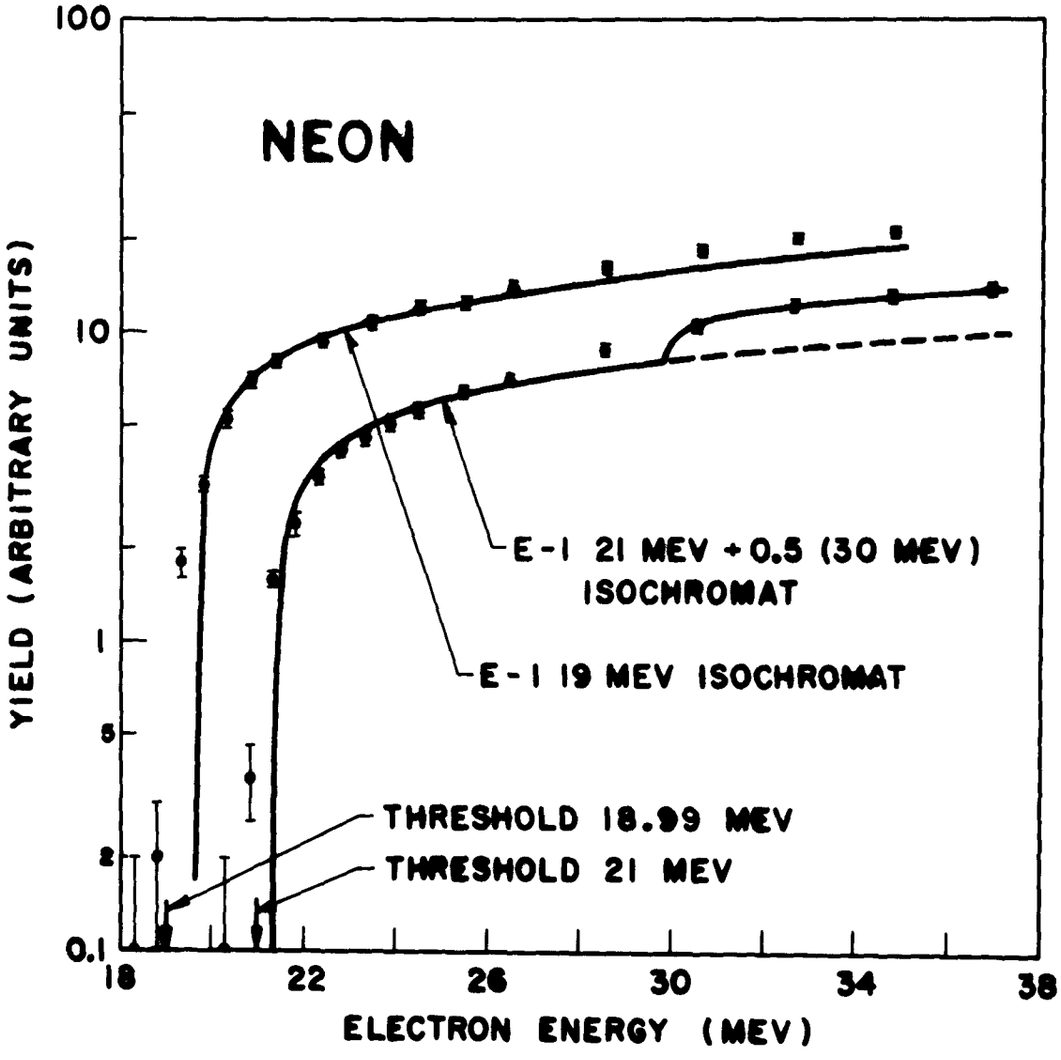
NEON
YIELD (ARBITRARY UNITS)
100
10
1
5
2
0.1
18
22
26
30
34
38
ELECTRON ENERGY (MEV)
E-1 21 MEV + 0.5 (30 MEV) ISOCHROMAT
E-1 19 MEV ISOCHROMAT
THRESHOLD 18.99 MEV
THRESHOLD 21 MEV

FIGURE 21

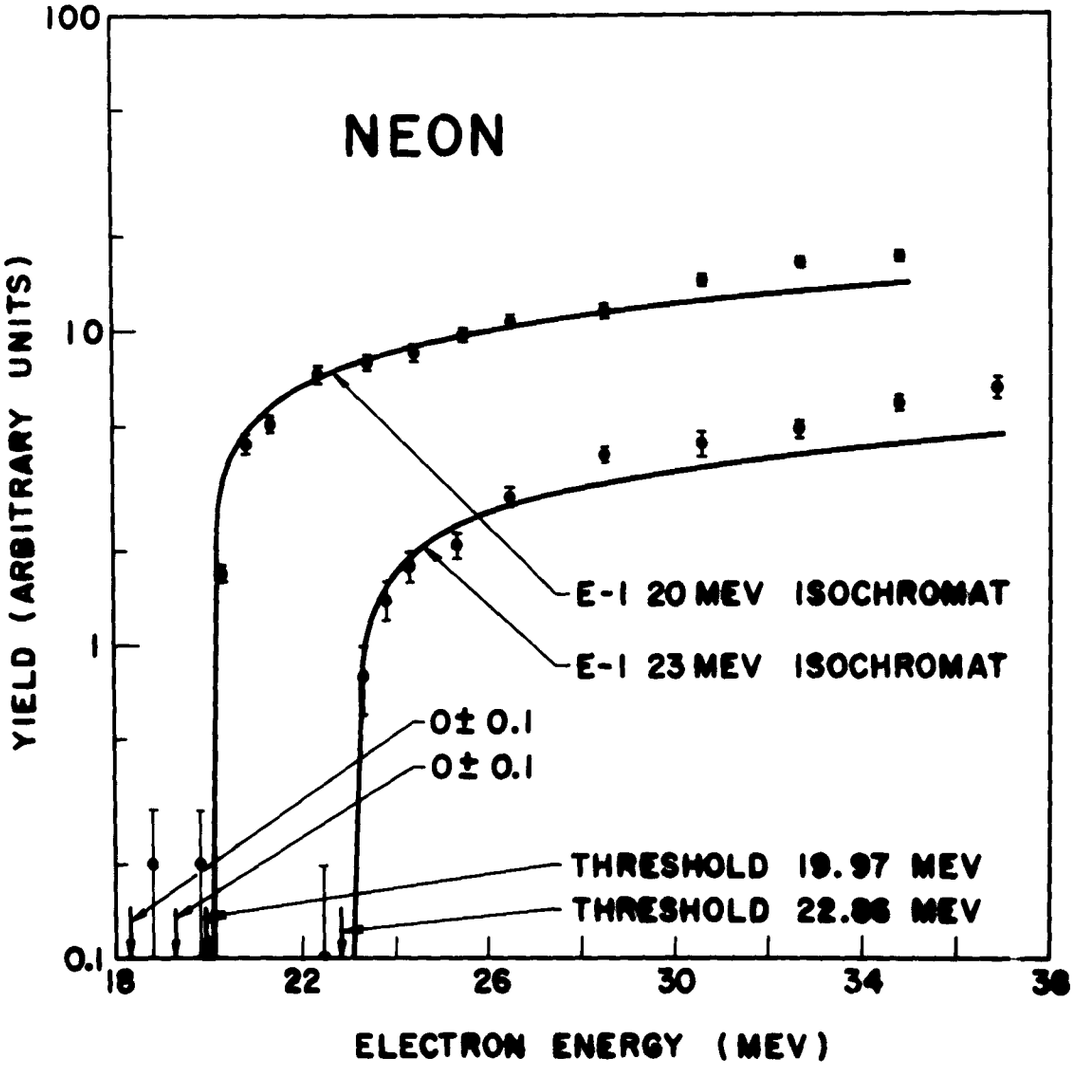
NEON
100
10
1
0.1
YIELD (ARBITRARY UNITS)
18
22
26
30
34
38
ELECTRON ENERGY (MEV)
E-1 20 MEV ISOCHROMAT
E-1 23 MEV ISOCHROMAT
0 ± 0.1
0 ± 0.1
THRESHOLD 19.97 MEV
THRESHOLD 22.86 MEV

FIGURE 22

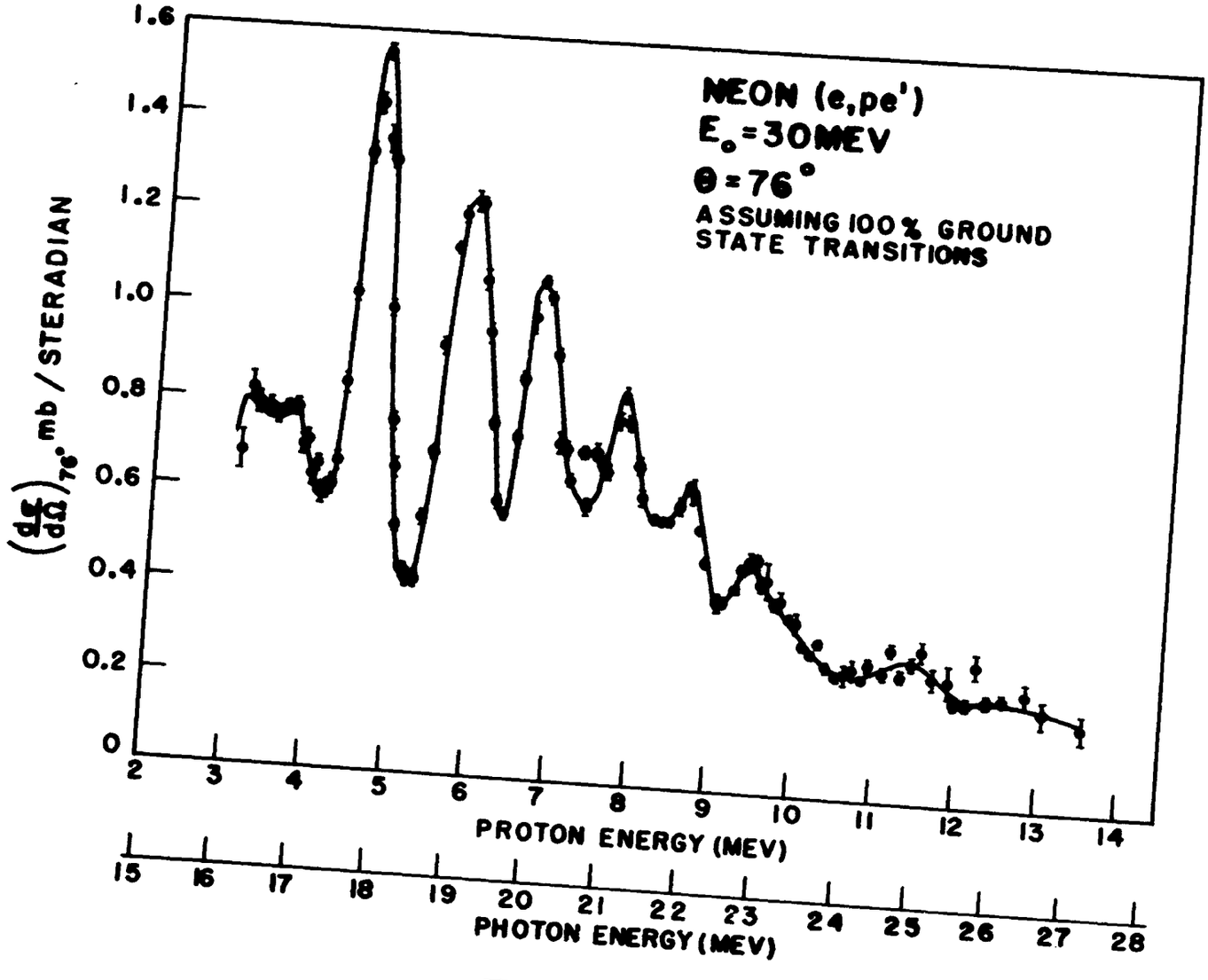
NEON (e,pe')
E₀=30MEV
θ=76°
ASSUMING 100% GROUND STATE TRANSITIONS
(dσ/dΩ)₇₆°, mb / STERADIAN
1.6
1.4
1.2
1.0
0.8
0.6
0.4
0.2
0
2 3 4 5 6 7 8 9 10 11 12 13 14
PROTON ENERGY (MEV)
15 16 17 18 19 20 21 22 23 24 25 26 27 28
PHOTON ENERGY (MEV)

FIGURE 23

TABLE VI. Summary of the excitation characteristics of the Ne protons.

Proton energy (Mev)	Ground state transition energy (Mev)	Experimental threshold (Mev)	Electron energy at which a deviation from an E-1 isochromat occurs (Mev)	Branching ratio (%)	Energy of excited state (Mev)
4.56	17.68	17.7 ± .3	21.8 ± .5	17 ± 8	4.1 ± .5
5.20	18.35	19.4 ± .6	21.8 ± .7 ; $27.8^{+1.3}_{-1}$	25 ± 5 ; 39 ± 10	3.5 ± .7 ; $9.5^{+1.3}_{-1}$
5.57	18.74	19.5 ± .7	———	———	———
5.81	18.99	19.6 ± .6	———	———	———
6.74	19.97	20.0 ± .4	———	———	———
7.22	20.47	20.4 ± .4	———	———	———
7.77	21.00	21.4 ± .5	29.8 ± 1	26 ± 10	8.8 ± 1
8.30	21.61	21.9 ± .5	26.0 ± 1	29 ± 10	4.4 ± 1
8.72	22.05	22.3 ± .5	26.5 ± 1	29 ± 10	4.5 ± 1
9.20	22.56	23.0 ± .6	28.2 ± 1.5	29 ± 10	5.2 ± 1.5
9.49	22.86	23.0 ± .5	27.6 ± 1.5*	———	4.7 ± 1.5*
9.86	23.25	23.6 ± .6	———	———	———

*Slight evidence.

TABLE VII. Summary of the properties of the major Ne peaks.

Proton energy of peak (Mev)	Photon energy of peak (Mev)	Peak height at 76° (mb/sr)	Photon width at half height (Mev)	$\int\sigma(\gamma,p)dE_\gamma$ under resonance curve (Mev-mb)	$\% \int_{16}^{27}\sigma(\gamma,p)dE_\gamma$
4.58	17.70	1.45	.50	11.4	19.0
5.80	18.87	1.11	.58	11.1	16.7
6.65	19.87	0.90	.54	7.6	12.7
7.75	21.02	0.77	.49	6.1	10.5
			Total	36.2	58.9

the agreement between the direct and inverse reactions is not necessarily a confirmation of detailed balance; the similarity between the two previous reactions probably stresses the importance of the excitation of discrete levels or very closely spaced groups of levels in Ne^{20} about 1-Mev apart.)

The cross section in the region of the four major peaks can be approximated by a superposition of resonance curves. The width, peak-height, area, and integrated cross section of the individual resonance curve belonging to each peak are presented in Table VII. Making the same crude estimates for the contributions of the experimental resolution to the peak width as in the O discussion section results in photon half-widths of .46, .52, .49, and .42 Mev, respectively.

3.4 Argon. Our survey study of the A (e,pe') energy spectrum at E_0 = 30 Mev, $\theta = 76°$ (Fig. 24) exhibits a sharp maximum at a proton energy E_p of 3.6 ± .1 Mev, with the yield nearly inversely proportional to E_p from the peak to E_p = 6.8 Mev, where an inflection occurs in the yield curve. The general features of the energy spectrum are in agreement with the statistically inferior work of Iavor.[54] Since we lack an experimentally determined relationship between photon and proton energy, we can only set limits on the cross section integrated over our proton-energy interval. An isotropic angular distribution is assumed. The assumption of ground-state transitions, which would make the (γ,p) peak occur at the same photon energy as the (γ,n) peak cross section, leads to 62 Mev-mb; while the assumption that the peak yield arises from the absorption of 24-Mev photons leads to 110 Mev-mb. The latter assumption is supported by the energy spectra of Emma et al.[55] taken at bremsstrahlung endpoint energies of 23, 26, and 30

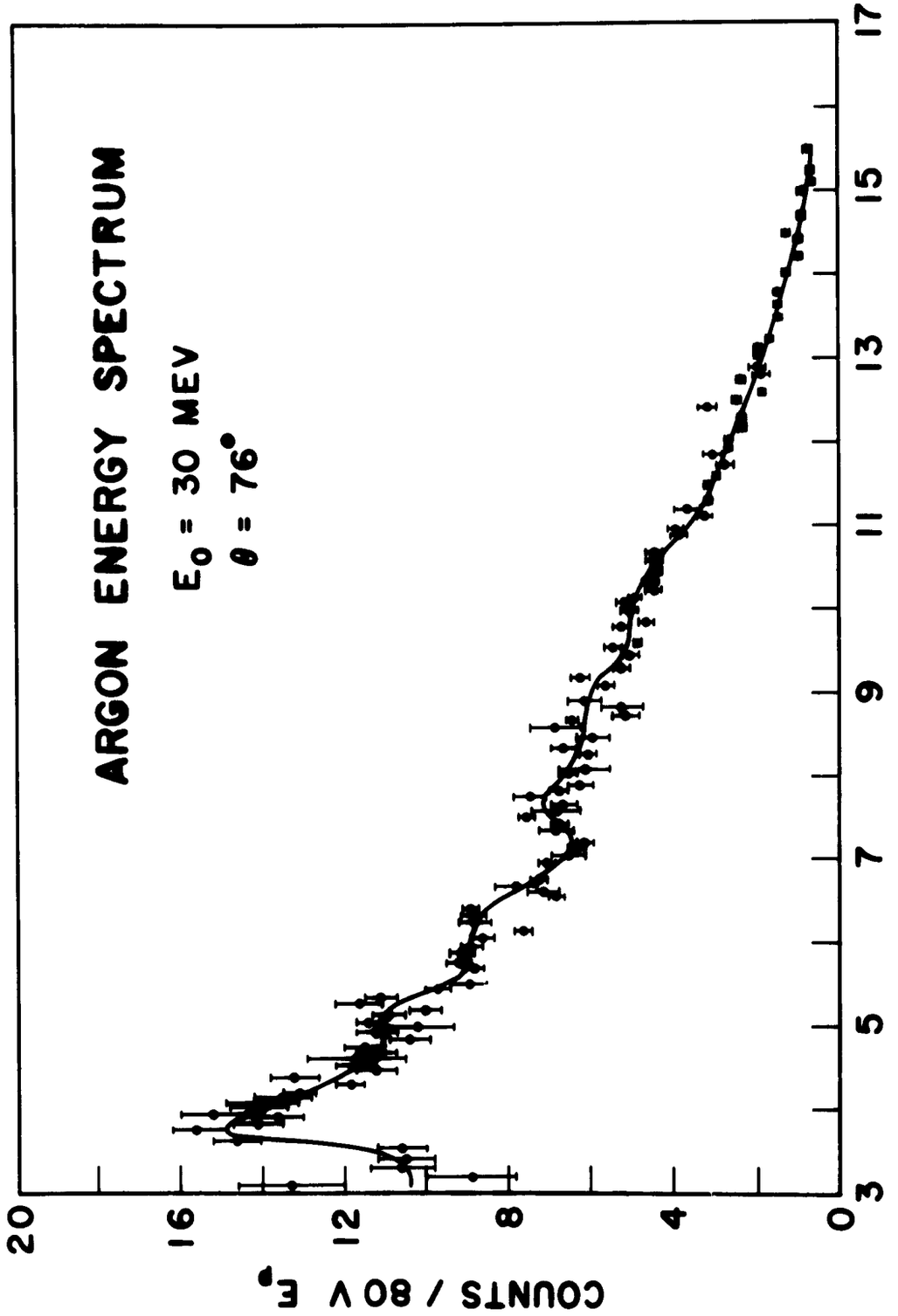
ARGON ENERGY SPECTRUM
E_0 = 30 MEV
θ = 76°
COUNTS / 80 V E_p
PROTON ENERGY (MEV)
0
4
8
12
16
20
3
5
7
9
11
13
15
17

FIGURE 24

Mev, and by the shape of $\sigma(\gamma,p)$ measured by Penfold and Garwin.[56] Consequently, we conclude that for A^{40}

$$62 \text{ Mev-mb} < \int_{E_p=3.1}^{E_p=15.25} \sigma(\gamma,p)dE_\gamma < 110 \text{ Mev-mb}. \qquad (24)$$

Cloud-chamber measurements with $E_{\gamma\ max} = 15.1$ Mev by Gudden and Eichler,[57] together with estimates of our α-particle counting efficiency, and the continuity of the yields during runs in which the A pressure was changed by a factor of ~ 2 indicate that the large $\sigma(\gamma,\alpha)$ postulated by Emma et al. is not observed. If the detected yields had been α particles, the large α-particle energy-loss differences caused by the pressure change would have produced a measurable yield discontinuity.

3.5 Boron. The B energy spectrum at $E_0 = 30$ Mev (Fig. 25) exhibits a broad maximum extending from 3 to 5 Mev with a long high-energy tail. Suggestions of structure appear but statistics do not warrant detailed speculation. Since neither excitation functions nor angular distributions were measured, the B data do not merit extensive discussion. The photoplate work of Erdös et al.[58] and estimates of our efficiency for counting deuterons both indicate that most of the yield is protons. In order to provide limits for the $B \int \sigma(\gamma,p)dE_\gamma$ we make a plausible analogy to the F^{19} (γ,p) reaction, assuming B^{11} and C^{12} (γ,p) reactions are homologous to the F^{19} and Ne^{20} (γ,p) reactions. Using the above analogy, 100% population of the 1^- and 2^- states at 5.96 and 6.26 Mev gives for the $B \int \sigma(\gamma,p)dE_\gamma$ the value 42 Mev-mb. A lower limit is 25 Mev-mb. These estimates are for the proton-energy interval from 3.5 to 15 Mev.

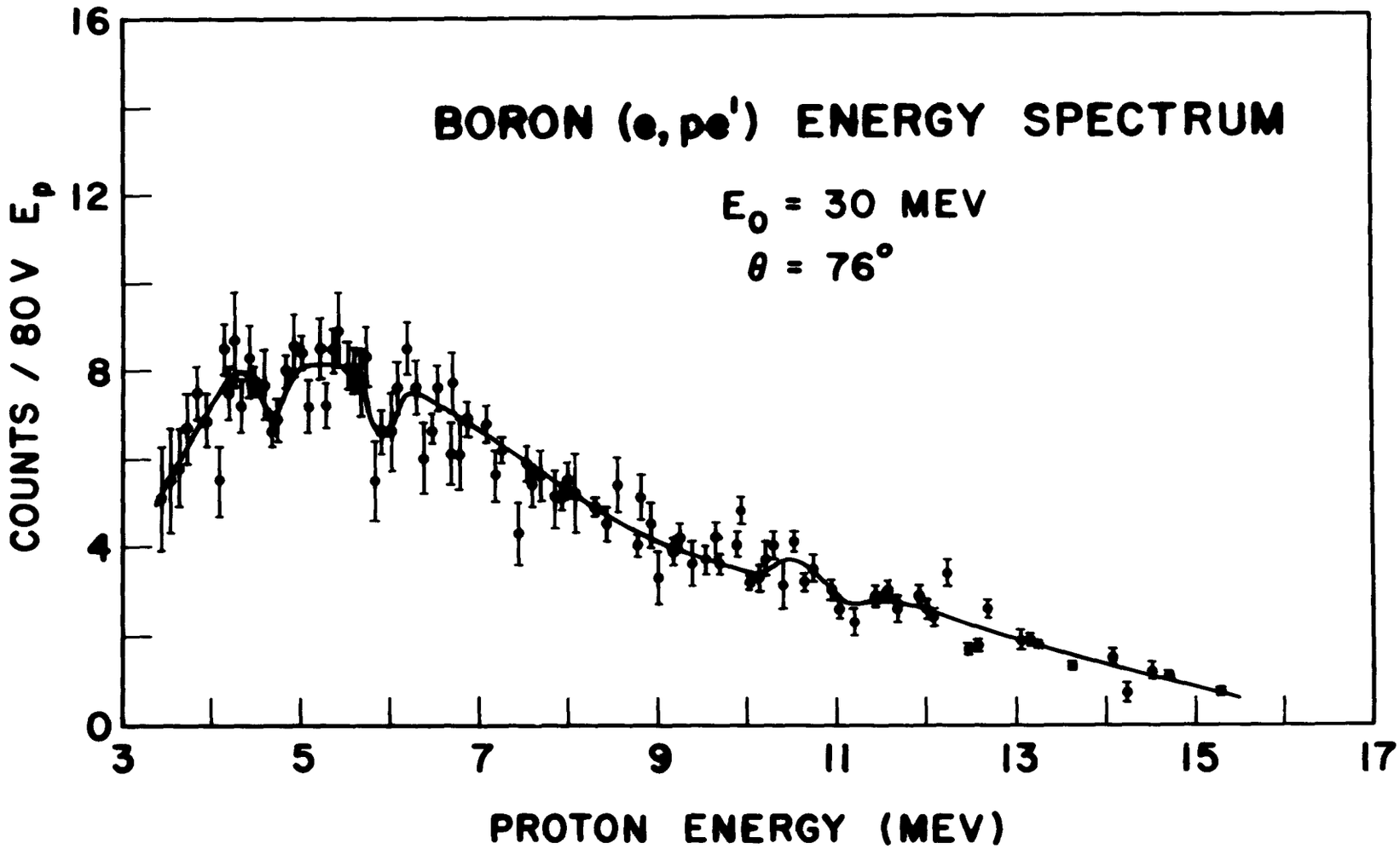
BORON (e, pe') ENERGY SPECTRUM
E_0 = 30 MEV
θ = 76°
COUNTS / 80 V E_p
PROTON ENERGY (MEV)
0
4
8
12
16
3
5
7
9
11
13
15
17

FIGURE 25

3.6 Carbon. Our C^{12} $\sigma(\gamma,p)$ at E_0 = 30 Mev (Fig. 26) shows the giant resonance peak at E_p = 6.05 Mev, with slight evidence for structure at 6.7 and 3.2 Mev but with no evidence for splitting of the magnitude observed by Cohen et al.[59] The width of the C^{12} (γ,p) giant resonance at half-maximum is approximately 3.1 Mev which is slightly narrower than previously reported.[60] Some evidence for fine structure exists at proton energies of 8.2, 8.9, 10.2, and 10.9 Mev in the 30-Mev data. The energy spectrum at 24.5 Mev (Fig. 27) again gives us no evidence for splitting; and above proton energies of 8 Mev, where proton emission is energetically impossible, it demonstrates the validity of the background-subtraction method employed. The cross section for E_0 = 24.5 Mev (Fig. 28) is in essential agreement with the 30-Mev cross section, as expected, since the precise work of Penner and Leiss[61] showed an excited-state cross section of 7 ± 16% of the ground-state cross section for photon energies below 30 Mev. We obtained a differential cross section of 1.03 mb/sr at 76° at E_p = 6.05 Mev, and

$$\int_{20.3}^{29.3} \sigma(\gamma,p)dE_\gamma = 50 \pm 8 \text{ Mev-mb} \qquad (25)$$

for C^{12}. Using detailed balance, Gemmell et al.[62] obtained 24 ± 5 mb for the peak cross section from the inverse B^{11} (p,γ) C^{12} reaction. This value becomes 19 ± 4 Mev-mb after converting from the isotropic angular distribution Gemmel et al. assumed to a $1 + 3/2 \sin^2 \theta$ angular distribution (a factor of 4/5 for an angular distribution measured at 90°). However, as pointed out in the discussion of the Ne results, the F^{19} $\sigma(p,\gamma_0)$ Ne^{20} of Gemmell et al., obtained with the use of detailed balance

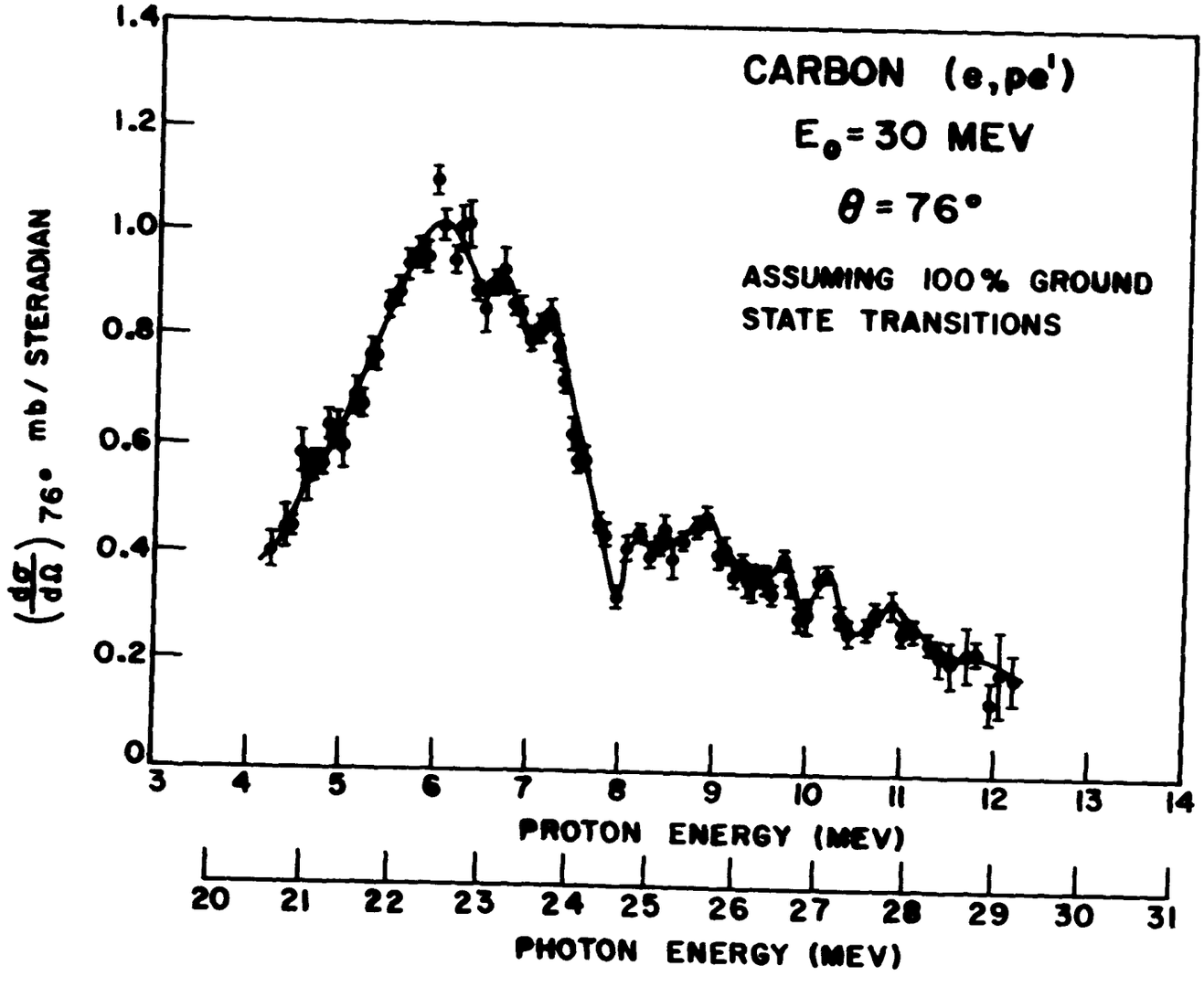
CARBON (e,pe')
E_e = 30 MEV
θ = 76°
ASSUMING 100% GROUND STATE TRANSITIONS
$(\frac{d\sigma}{d\Omega})_{76°}$ mb/STERADIAN
1.4
1.2
1.0
0.8
0.6
0.4
0.2
0
3 4 5 6 7 8 9 10 11 12 13 14
PROTON ENERGY (MEV)
20 21 22 23 24 25 26 27 28 29 30 31
PHOTON ENERGY (MEV)

FIGURE 26

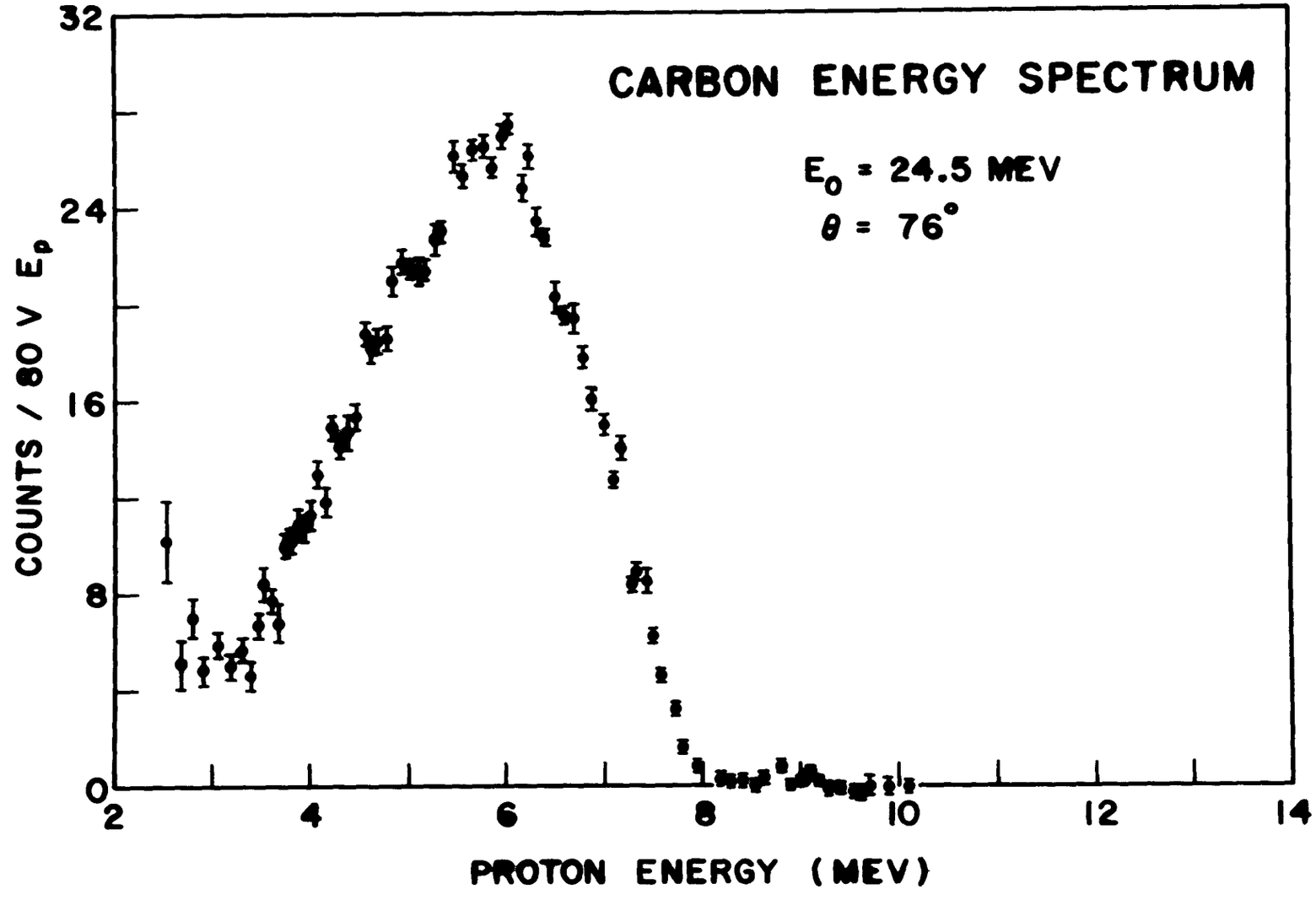
CARBON ENERGY SPECTRUM
E_0 = 24.5 MEV
θ = 76°
COUNTS / 80 V E_p
PROTON ENERGY (MEV)
0
8
16
24
32
2
4
6
8
10
12
14

FIGURE 27

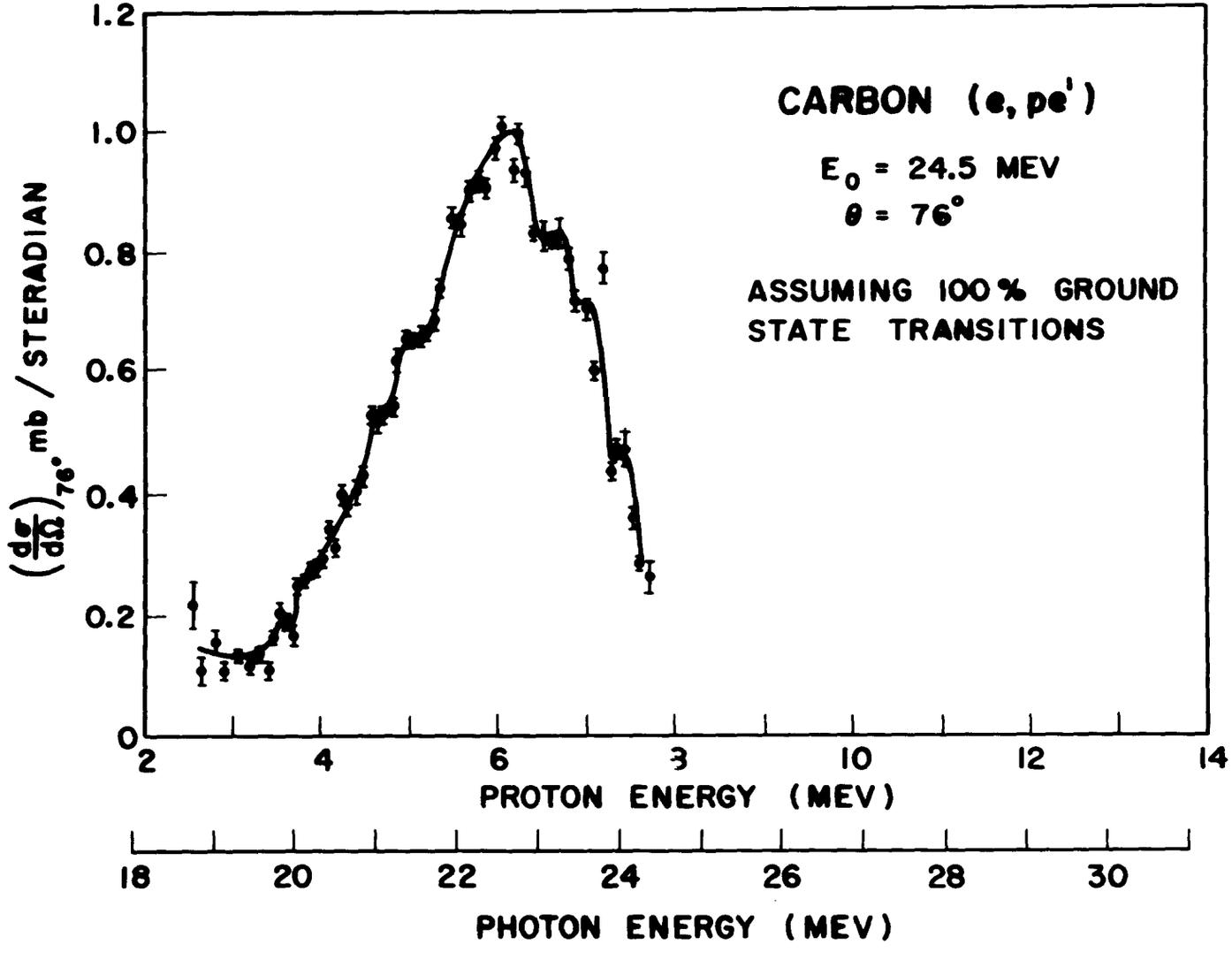
CARBON (e, pe')
E0 = 24.5 MEV
θ = 76°
ASSUMING 100% GROUND STATE TRANSITIONS
(dσ/dΩ)76°, mb / STERADIAN
PROTON ENERGY (MEV)
PHOTON ENERGY (MEV)

FIGURE 28

is also about a factor of two larger than our value or Thomas et al.'s[15] inverse cross section when the latter used an independent calibration. Gove et al.[63] have obtained 12 mb for the peak cross section at E_p = 6.05 Mev from the inverse reaction; while our value is 11.0 ± 15% mb for a $1 \pm 3/2 \sin^2 \theta$ angular distribution, or 9.6 mb using the least squares fit coefficients to our 5.90-Mev C^{12} angular distribution, properly normalized to the peak $d\sigma/d\Omega$.

3.7 Aluminum. The Al proton energy spectra from a 20.6 mg/cm^2 foil of commercial purity (99% Al) used to monitor the stability and reliability of the experimental apparatus as previously explained are shown in Figs. 29 and 30 for E_0 = 18, 24.5, and 30 Mev. As in the case of F, comparison of the yield ratios at the three primary electron energies with the ratios of E-1 virtual-photon isochromats enabled us to establish a semi-quantitative relationship between k and E_p (see Table VIII). The relationship $k = \frac{27}{26}E_p + 16$ seems appropriate in the proton-energy interval of 3.4 to 6-7 Mev. Beyond proton energies of 7 Mev, $k = \frac{27}{26}E_p + 14$ seems indicated. For simplicity, the assumption that $k = \frac{27}{26}E_p + 14$ over the entire range of proton energies was made to compute the cross section shown in Fig. 31; the errors are derived from counting statistics only and do not include the uncertainty in the relationship between k and E_p. In any event, the available information does not justify a more sophisticated analysis. The previous experiments of Diven and Almy[64] and those of Dawson[65] had neither the resolution nor the statistics to detect the hump we observed in the region of 8 Mev. However, our work is in agreement with the gross features of

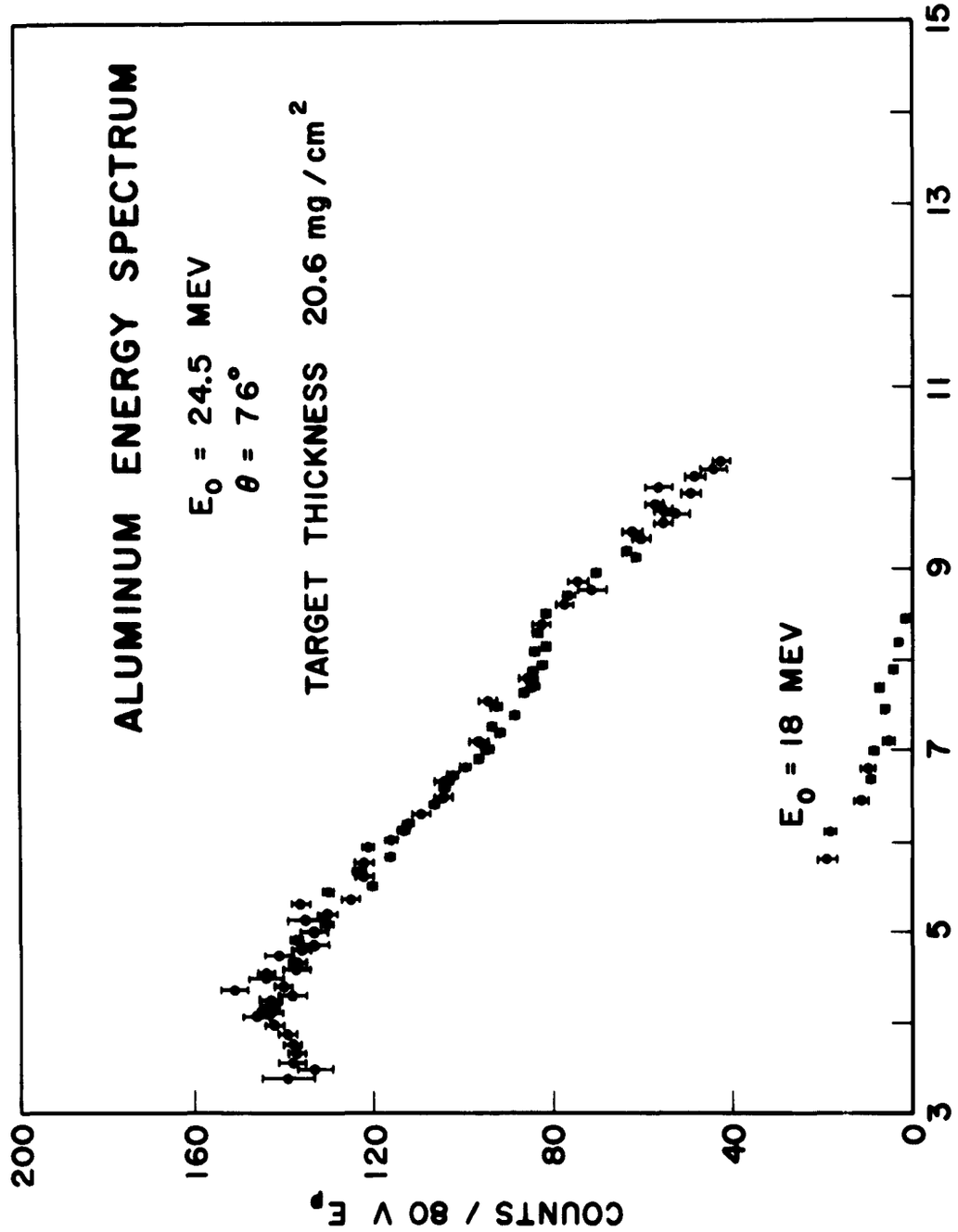
ALUMINUM ENERGY SPECTRUM
E_0 = 24.5 MEV
θ = 76°
TARGET THICKNESS 20.6 mg / cm^2
E_0 = 18 MEV
COUNTS / 80 V E_p
PROTON ENERGY (MEV)
0
40
80
120
160
200
3
5
7
9
11
13
15

FIGURE 29

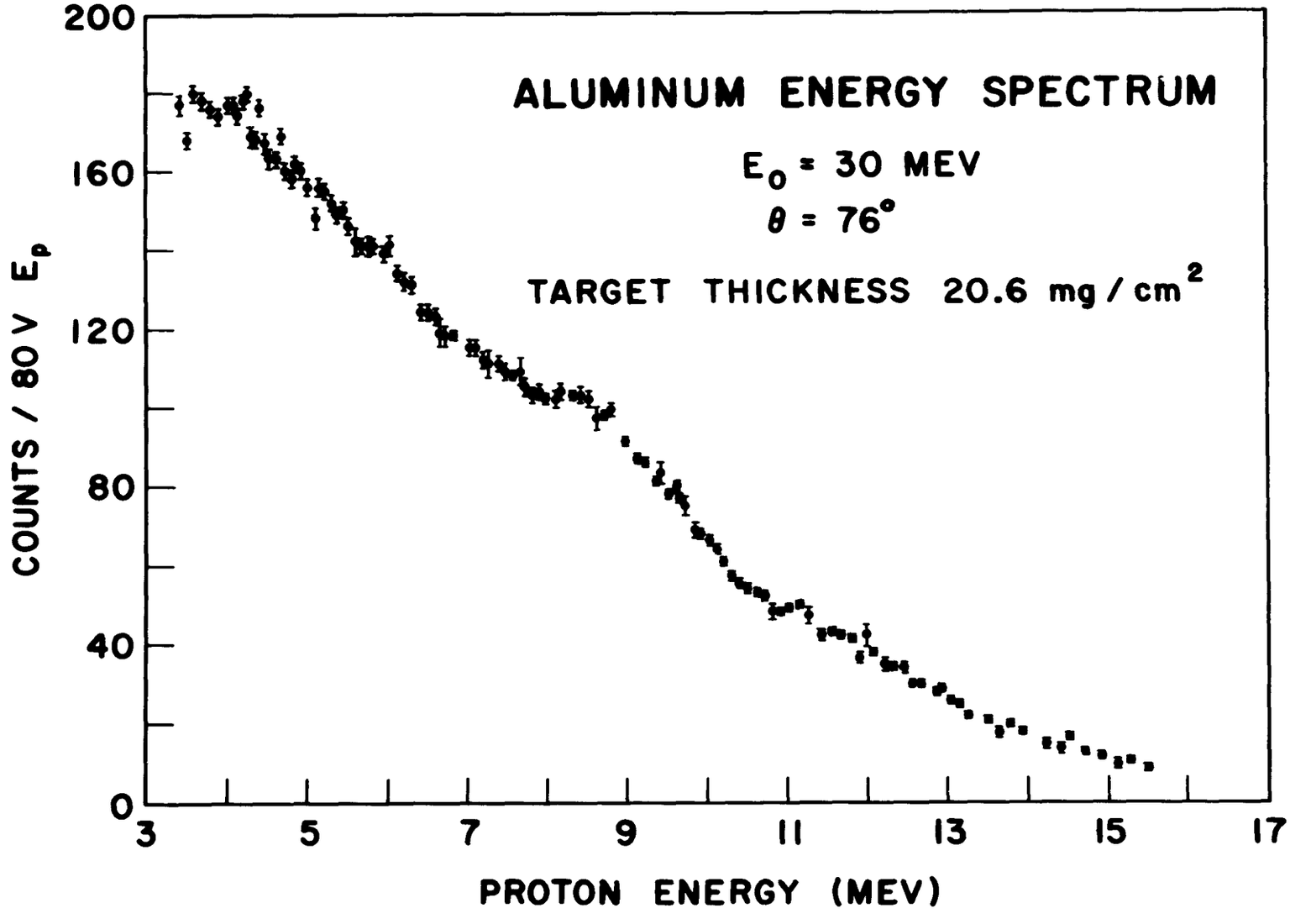
ALUMINUM ENERGY SPECTRUM
E_0 = 30 MEV
θ = 76°
TARGET THICKNESS 20.6 mg / cm^2
COUNTS / 80 V E_p
PROTON ENERGY (MEV)
0
40
80
120
160
200
3
5
7
9
11
13
15
17

FIGURE 30

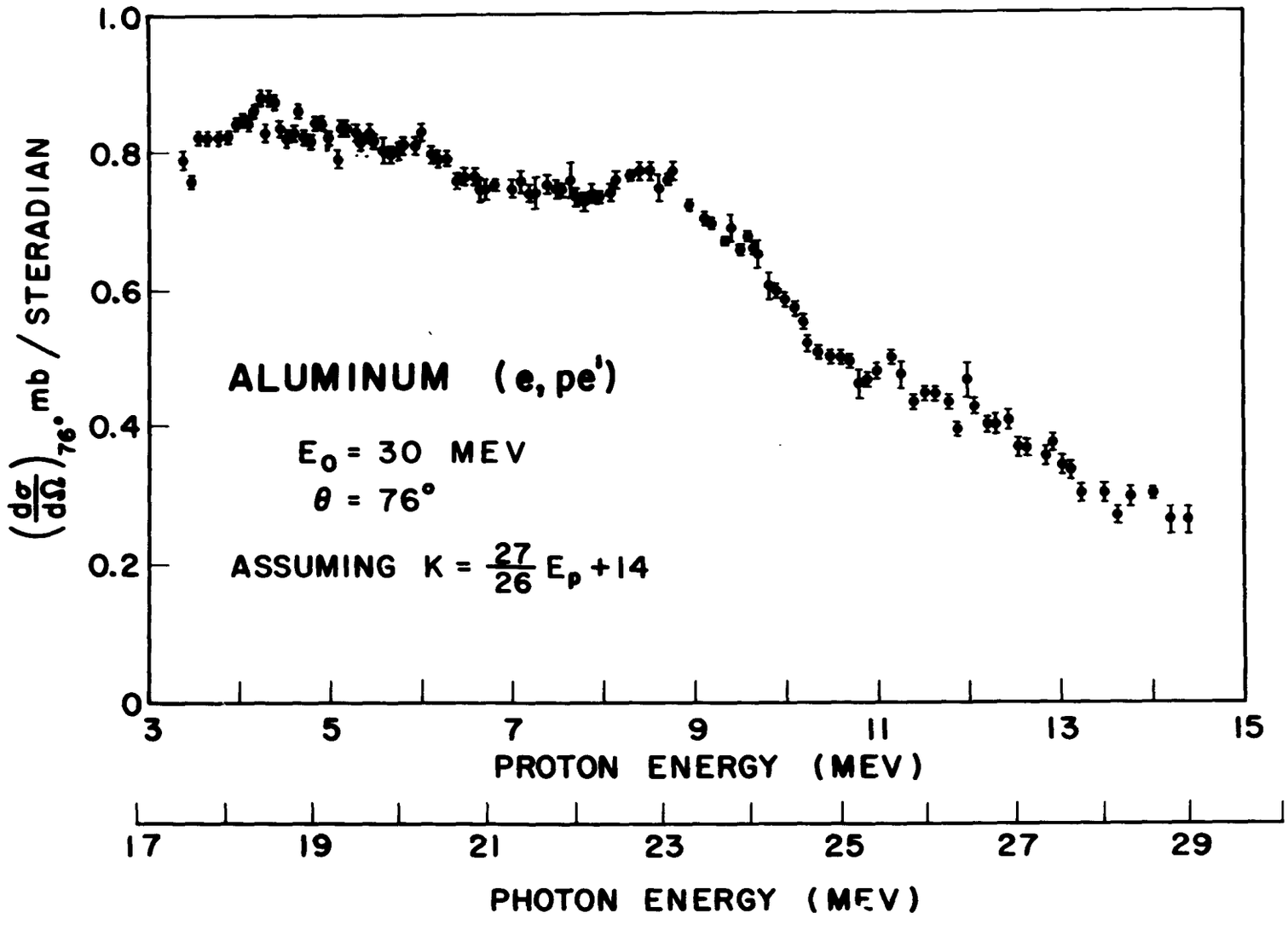
1.0
0.8
0.6
0.4
0.2
0
$\left(\frac{d\sigma}{d\Omega}\right)_{76°}$ mb / STERADIAN
ALUMINUM (e, pe')
E_0 = 30 MEV
θ = 76°
ASSUMING K = $\frac{27}{26}E_p + 14$
3
5
7
9
11
13
15
PROTON ENERGY (MEV)
17
19
21
23
25
27
29
PHOTON ENERGY (MEV)

FIGURE 31

TABLE VIII. Comparison of Al yields at primary electron energies of 18, 24.5, and 30 Mev.

Proton energy (Mev)	Yield E_o = 18 (Mev)	Yield E_o = 24.5 (Mev)	Yield E_o = 30 (Mev)	Yield (24.5) / Yield (18)	Yield (30) / Yield (24.5)	$\frac{N_{E-1}(30,k)}{N_{E-1}(24,k)}$ [k= $\frac{27}{26}E_p$+16]	$\frac{N_{E-1}(30,k)}{N_{E-1}(24,k)}$ [k= $\frac{27}{26}E_p$+14]
5.19	——	130 ± 2	205 ± 2	——	1.58 ± .06	1.52	——
5.60	——	122 ± 2	193 ± 2	——	1.59 ± .06	1.54	——
6.02	18.0 ± 1.5	115 ± 2	180 ± 2	6.5 ± 0.6	1.56 ± .06	1.58	——
6.53	11.0 ± 1.5	104 ± 2	170 ± 2	9.5 ± 1.0	1.64 ± .06	1.73	——
7.01	8.5 ± 1.0	94 ± 2	155 ± 2	11.0 ± 2.0	1.65 ± .06	——	1.52
7.47	6.3 ± 0.8	88 ± 2	149 ± 2	14.0 ± 2.0	1.69 ± .06	——	1.54
7.94	4.4 ± 0.8	82 ± 2	140 ± 2	19.0 ± 3.0	1.71 ± .06	——	1.58
8.45	1.2 ± 1.0	82 ± 2	142 ± 2	68.0 ± 57.0	1.73 ± .06	——	1.73
8.91	——	72 ± 2	130 ± 2	——	1.81 ± .07	——	1.91
9.39	——	62 ± 2	110 ± 2	——	1.78 ± .07	——	2.11

their results. We obtained for Al^{27}

$$\int_{18.5}^{29} \sigma(\gamma,p)dE_\gamma = 94 \pm 19\% \text{ Mev-mb}, \qquad (26)$$

with the use of our angular distribution data. Dawson, using Halpern and Mann's[66] data for calibration, obtained $\int \sigma(\gamma,p)dE_\gamma = 120 \pm 30$ Mev-mb, with unspecified photon limits but presumably over the entire range of sensibly non-zero cross section. For Al $\int_{13}^{18.5}\sigma(\gamma,n)dE_\gamma$, Baglin et al.[67] measured 28 Mev-mb. Since the proton thickness of our Al target was great enough to partially obscure any interesting fine structure, the energy spectrum will not be discussed further; however, the suggestion of unresolved structure, especially at 8 Mev, together with the alleged structure in the total photon absorption curve and Baglin et al.'s calculations are intriguing; and perhaps future Al (γ,p) experiments with thinner targets are advisable. On the other hand, our isotropic angular distributions suggest a statistical emission process and smooth absorption cross section.

B. Angular Distribution Measurements

3.8 The effective gas-target thickness as a function of spectrometer angle. In order to interpret the angular distribution data, the effective gas-target thickness as a function of spectrometer angle had to be known. The effective gas-target thickness was calculated, after attempts to obtain the desired quantity with elastic electron scattering measurements proved abortive, with the use of the measured spectrometer lateral efficiency and certain assumptions about the intensity distribution and width of the primary electron beam. We define the spectrometer lateral efficiency to be the efficiency for detecting particles which originate at positions along a line perpendicular to the spectrometer vertical symmetry-plane, and passing through the spectrometer focal point. The spectrometer lateral efficiency was determined by measuring the counting rate of α-particles from the Cm^{244} source, which was masked to a .06-in. vertical slit, as a function of the distance along the primary electron beam when the spectrometer was at 76°. The results are shown in Fig. 32a, b, and c. The low points, about .2 in. from the alleged vertical symmetry-plane, are due to the source passing behind two thin wires, equidistant from the scattering-chamber center. The slight asymmetry of the experimental lateral efficiency measurements can be partially accounted for by the fact that the source moved through the scattering-chamber center at an angle of 76° to the spectrometer vertical symmetry-plane instead of 90°, and by small differences in counter efficiency for events near the edge of the photocathode on opposite sides of the spectrometer symmetry-plane; the latter hypothesis is supported by the fact that measurements with counter 3 were slightly asymmetric, while those with counter 7 were

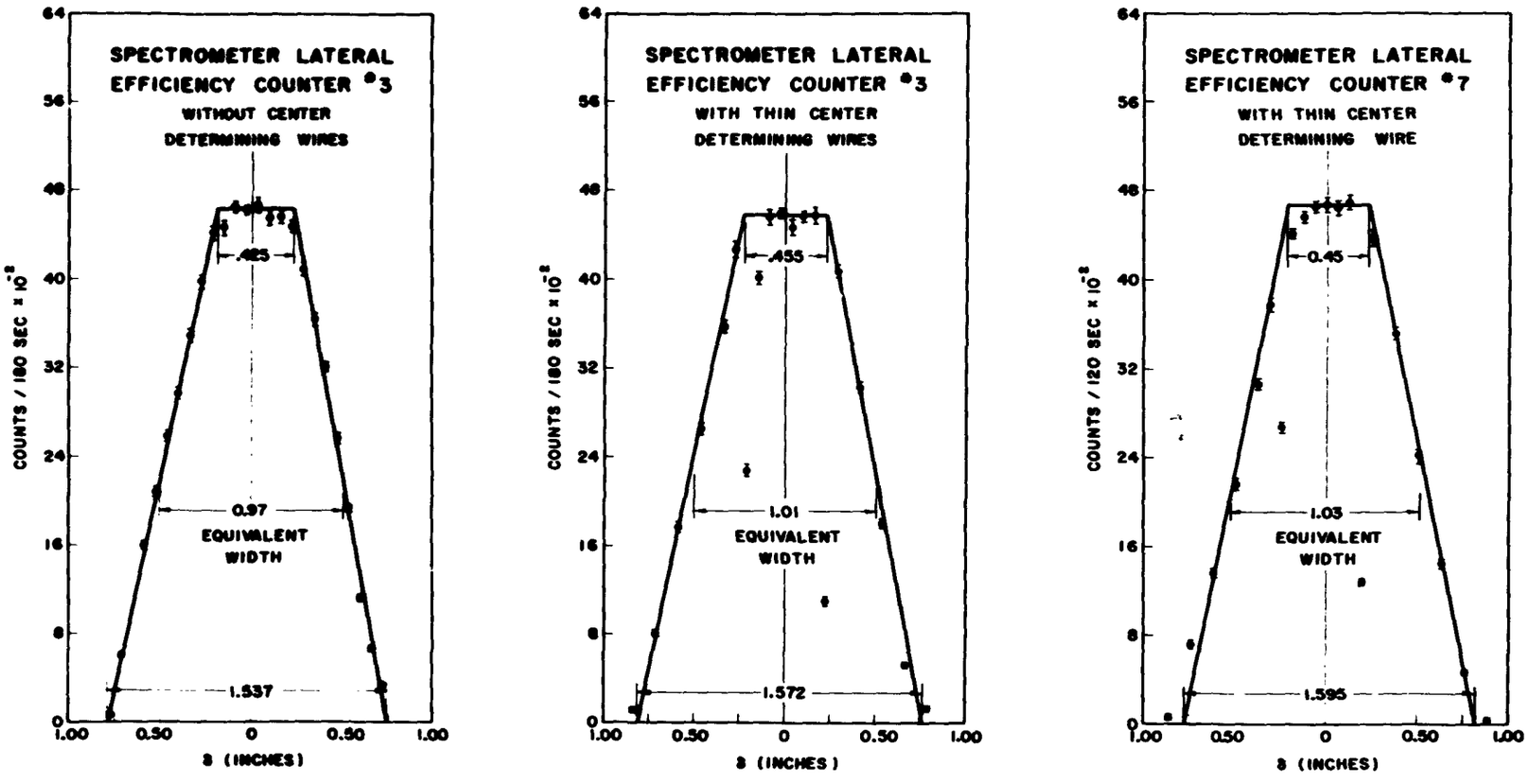
SPECTROMETER LATERAL
EFFICIENCY COUNTER #3
WITHOUT CENTER
DETERMINING WIRES
.485
0.97
EQUIVALENT
WIDTH
1.537
COUNTS / 180 SEC x 10⁻³
δ (INCHES)
SPECTROMETER LATERAL
EFFICIENCY COUNTER #3
WITH THIN CENTER
DETERMINING WIRES
.455
1.01
EQUIVALENT
WIDTH
1.572
COUNTS / 180 SEC x 10⁻³
δ (INCHES)
SPECTROMETER LATERAL
EFFICIENCY COUNTER #7
WITH THIN CENTER
DETERMINING WIRE
0.45
1.03
EQUIVALENT
WIDTH
1.595
COUNTS / 120 SEC x 10⁻³
δ (INCHES)

FIGURE 32

not. From these measurements it was concluded that the lateral efficiency function was a trapezoid of top $2\delta_- = .440 \pm .015$ in. and base $2\delta_+ = 1.550 \pm .040$ in. The errors are standard deviations.

The measured lateral efficiency function can be compared with the predictions of the first-order theory with a baffle of half-width W_b placed at a distance S_b from the source. First-order theory predicts that for a magnet of radius r_0, field index n, and source distance S_0, the solid angle as a function of the lateral distance δ from the vertical symmetry-plane is given by

$$\Delta\Omega(\delta) = \Delta\Omega_0 \; ; \quad 0 \leq \delta \leq \delta_-$$

$$= \frac{\Delta\Omega_0}{2} \left[1 + \frac{W_b}{W_0}\frac{S_0}{S_b} \left\{ 1 + \frac{1}{n}\left(\frac{r_0}{S_0}\right)^2 \right\}^{1/2} - \frac{\delta}{W_0} \left\{ \frac{S_0}{S_b}\left[1 + \frac{1}{n}\left(\frac{r_0}{S_0}\right)^2 \right]^{1/2} - 1 \right\} \right],$$

$$\delta_- \leq \delta \leq \delta_+ , \qquad (27)$$

where

$$\delta_\pm = W_0 \, \frac{\frac{W_b}{W_0}\frac{S_0}{S_b}\left[1 + \frac{1}{n}\left(\frac{r_0}{S_0}\right)^2 \right]^{1/2} \pm 1}{\frac{S_0}{S_b}\left[1 + \frac{1}{n}\left(\frac{r_0}{S_0}\right)^2 \right]^{1/2} - 1} \, . \qquad (28)$$

Thus the lateral efficiency function is predicted to be a trapezoid of top $2\delta_-$ and base $2\delta_+$. The experimental values of $S_b = 9$ in., $W_b = .44$ in., and $W_0 = 1.12$ in., and the previously quoted values for n, r_0, and S_0 of 1/2, 18 in., and 28 in. respectively give $\delta_- = .22$ in. and $\delta_+ = .93$ in., to be compared with the observed values of .22 in. and .78 in. The observed discrepancy in δ_+ is not so serious when account is taken of the finite width of the scintillators.

With no baffle

$$\delta_- = W_0 \ ,$$

and

$$\delta_+ = n(S_0/r_0)^2 \left\{1 + \left[1 + \frac{1}{n}(r_0/S_0)^2\right]^{1/2}\right\}^2 W_0$$

$$= 6.4\, W_0$$

for the above values of n, r_0, and S_0; but since the counter width was only 2 in., the lateral efficiency function was essentially a rectangle of 2-in. width for the conditions of the solid target experiments. The projected beam width on the solid target foils was always less than 1 in., which ensured that no counting losses were incurred by small horizontal shifts in the electron beam. These conclusions were experimentally checked by rotating the target foils about the vertical plane which varied the width of the electron beam projected on the target. The ratios of the yields multiplied by cosec φ, where φ is the angle between the target and the primary electron beam, were statistically the same for $\varphi > 30°$. In previous Stanford (e,pe') experiments[23] larger scintillators were used which could account for the background observed from the target-holder ladder, since the lateral transmission efficiency was about 98% at the scintillator edge in former experiments.

Since the lateral efficiency function for a magnetic spectrometer is in general trapezoidal, and since cylindrical target geometries are not uncommon, the relative effective target-thickness calculations are reproduced in Appendix I. Table IX shows the results of effective target-thickness calculations for spectrometer angles of 20°, 48°, and 76°, with

TABLE IX. Effective target thickness as a function of spectrometer angle and electron beam half-width W, with a target-chamber radius R equal to one inch.

W/R	δ-/R	δ+/R	Effective target thickness 20°	Effective target thickness 48°	Effective target thickness 76°	Ratio normalized at 76°	Average ratio
0	.225	.796	1.930	1.368	1.053	.547/.772/1.000	.558±.011/.775±.004/1.000
0	.225	.836	1.935	1.409	1.094	.566/.778/1.000	
0	.240	.796	1.945	1.387	1.068	.548/.770/1.000	
0	.240	.836	1.948	1.428	1.110	.571/.778/1.000	
.25	.225	.796	1.838	1.294	1.053	.574/.814/1.000	.586±.009/.803±.010/1.000
.25	.225	.836	1.848	1.378	1.094	.593/.796/1.000	
.25	.240	.796	1.840	1.316	1.068	.580/.812/1.000	
.25	.240	.836	1.860	1.402	1.110	.596/.792/1.000	

the assumption of 0.00-in. and .50-in. electron-beam width and the range of probable values of the lateral efficiency-function parameters. Semi-quantitative evidence exists for an electron-beam width of approximately .30 in. and trapzoidal intensity distribution[68]; therefore an average of the zero and .50-in. beam width relative effective target thicknesses, .572 ± .020/.789 ± .024/1.000, represent the best estimate with the available information. The errors associated with the experimental points in the angular distribution measurements include the uncertainty in the relative target thicknesses. All errors are standard deviations.

The calculated relative target thicknesses above are known to an accuracy compatible with the errors from counting statistics; but for a precise determination of the former quantities, a comparison of the angular distribution of carbon photoprotons from a CH (polystyrene) foil and methane (CH_4) in the gas chamber would be preferred. This measurement would correspond to the comparison of the angular distributions from a point and an extended source, and would eliminate uncertainties caused by a possible $\Delta p/p$ dependence of $\Delta\Omega$ for non-zero values of δ.

The electron beam was carefully centered on the gas target at each angle to avoid geometric uncertainties. This slight repositioning of the beam direction at each angle unfortunately could have been the cause of an even larger error than was avoided, since the SEM efficiency, after angular distributions were measured, apparently had increased by 7.5% as previously described. The increased Al proton yields at 76° observed upon completion of the angular distribution experiments which were used to conjecture the SEM efficiency change conceivably could have resulted

from an alteration of the Al target geometry during spectrometer angle changes rather than from a change in the SEM efficiency. An indentation of the target foil large enough to produce the observed effect — an effective increase of 9.2° in the angle between the target and electron beam would be required — would probably have been noticed. Since detailed experimental verification of the SEM's malfunction is lacking, no correction was made. The effect of the alleged SEM efficiency change on the O and Ne $d\sigma/d\Omega$ data would be to decrease the forward and increase the backward asymmetries. The conclusions based on a comparison of the O and Ne $d\sigma/d\Omega$ would not be altered since the data were taken consecutively at each angle.

3.9 Experimental methods and corrections. Angular distributions of the prominent peaks in Ne and O were made by successively positioning the peaks on the same counter by taking partial energy distributions at each angle to locate the peaks. The spectrometer field values which were used for the gaseous elements' angular distributions gave nearly the same proton energies after conversion from laboratory to center-of-mass energies. The center-of-mass proton kinetic energy T_{p_0} is related to the laboratory kinetic energy T_p by

$$T_{p_0} = \frac{[1 + (k/M_A)][T_p + M_p] - P_p\, k \cos\theta_{lab}}{[1 + (2k/M_A)]^{1/2}} - M_p$$

$$\approx T_p - [kM_p/M_A][2T_p/M_p]^{1/2} \cos\theta_{lab}\,, \qquad (29)$$

where M_A is the mass of the target nucleus, k is the energy of the photon inducing the reaction, and natural units are used. The small spread in the calculated center-of-mass energies as a function of angle gives credence to the assumption that most of the detected particles are protons and is a measure of the accuracy of the location of the peaks. (For the 9.53 ± .04 Mev peak in O the center-of-mass energies were 9.51 Mev, 20°; 9.53 Mev, 48°, 9.55 Mev, 76°; 9.61 Mev, 104°; 9.52 Mev, 132°; and 9.47 Mev, 160°. The energies of the largest two neon peaks were similarly determined on the basis of reproducibility to be located at 4.59 ± .03 and 5.79 ± .02 Mev.) Because the energies of the angular-distribution data points for the solid targets and for the gaseous targets from counters other than the one which followed the peak under observation were a slight function of the spectrometer angle, the data points were corrected to the value of the cross section corresponding to the average center-of-mass kinetic energy T_{lab} by referring to the cross section at 76°. The correction was largest for those elements whose cross section changed rapidly with proton energy, and was approximately 10% in the extreme cases at the extreme angles. The uncertainty of this correction was incorporated in the angular-distribution data errors.

The angular distributions' even-parity terms, which are assumed to arise entirely from an E-1 interaction, have been corrected for the dependence of the E-1 virtual-photon spectrum on the reaction product angle [Eq. (4)]. Therefore, if the (e,pe) angular distribution has t' form

$$A + B \cos\theta + C \sin^2\theta + D \sin^2\theta \cos\theta \,, \qquad (10)$$

the quantities

$$A' = A - \left[C \frac{\omega'}{\omega} \Big/ \left(\frac{\omega^2 + \omega'^2}{\omega\omega'} \lambda - 2 - \frac{3}{2} \frac{\omega'}{\omega} \right) \right] , \qquad (31)$$

and

$$C' = \left[C \left(\frac{\omega^2 + \omega'^2}{\omega\omega'} \lambda - 2 \right) \right] \Big/ \left[\frac{\omega^2 + \omega'^2}{\omega\omega'} \lambda - 2 - \frac{3}{2} \frac{\omega'}{\omega} \right] \qquad (32)$$

should be the same as the respective even-parity terms of the real-photon-induced angular distribution. The odd-parity terms, attributable to interference between E-1 and E-2 transitions, were not corrected for the dependence of the E-2 virtual-photon spectrum on reaction product angle.

The second order effects of finite angular divergence and of multiple scattering of the initial electron beam on the proton angular distribution are negligible for this experiment. If the incident beam attained a maximum half-width $W_{1/2}$ in an analyzing magnet of focal length f before being incident on the target, the angular distribution [Eq. (30)] would be measured as

$$A + \tfrac{1}{3}(W_{1/2}/f)^2 C + \{[1 - \tfrac{1}{6}(W_{1/2}/f)^2]B - \tfrac{1}{3}(W_{1/2}/F)^2 D\} \cos\theta$$

$$+ [1 - \tfrac{2}{3}(W_{1/2}/f)^2]C \sin^2\theta + [1 - \tfrac{1}{3}(W_{1/2}/f)^2]D \sin^2\theta \cos\theta . \qquad (33)$$

Multiple-scattering of the primary electron beam in the material ahead of the target changes a sensibly parallel beam into a cone-shaped diverging beam whose intensity is proportional to $e - (\theta^2/2\sigma^2)$, where θ is the half-angle of the cone and σ is the rms scattering angle previously defined [Eq. (5)]. Assuming a parallel electron beam would produce Eq. (30), multiple scattering changes this to

$$A + 2\sigma^2 C + [(1 - \sigma^2)B + 2\sigma^2 D]\cos\theta$$

$$+ (1 - 3\sigma^2)C \sin^2\theta + (1 - \tfrac{9}{2}\sigma^2)D \sin^2\theta \cos\theta \ . \quad (33)$$

For this experiment $W_{1/2}/f$ was $\approx 1.3 \times 10^{-2}$ and $\sigma \approx 2.7 \times 10^{-2}$ radian (1.5°); consequently the above corrections are negligible. The correction for the reaction-product angular dependence of the virtual-photon spectrum was much greater than the multiple-scattering correction in our experiment.

Lastly, the angular distributions were not corrected for finite angular resolution of the spectrometer since this correction was also very small. In general, for a spectrometer of finite horizontal acceptance angle 2Δ, the assumed angular distribution [Eq. (30)] is transformed to

$$A + C \sin^2\Delta + (B \cos\Delta + \tfrac{1}{2} D \sin\Delta \sin 2\Delta) \cos\theta$$

$$+ C(1 - \tfrac{4}{3}\sin^2\Delta) \sin^2\theta + D \cos\Delta \cos 2\Delta \sin^2\theta \cos\theta . \quad (34)$$

For a magnetic spectrometer

$$\tan\Delta = \frac{W}{S_0[1 + \frac{1}{n}(r_0/S_0)^2]^{1/2}} \ , \quad (35)$$

where all symbols except W, the accessible horizontal aperture half-width, have been previously defined [see Eq. (27)]. For an $n = 1/2$ spectrometer

$$\tan\Delta = \sqrt{\Delta\Omega/\Lambda} \ , \quad (36)$$

where Λ is the ratio of the magnet aperture height to width. In the case of this experiment $\tan \Delta = .03$; so this correction is also negligible. These conclusions supercede those of Vanhuyse and Barber.[60]

The relationships between the laboratory system and the center-of-mass system for the (γ,p) reaction are given in Appendix II, Table AII-I.

3.10 Discussion of the angular distributions. The O, F, Ne, C, and Al angular distributions data was fitted to a cos θ power series of fourth degree by the least squares method and the results expressed in the form of Eq. (30) and $\sum_{\ell=0}^{\ell=3} C_\ell P_\ell(\cos\theta)$. The even-parity terms of Eq. (30), A and C , were then corrected to photoproduction [Eqs. (35) and (36)]. The resultant coefficients and their standard deviations in mb/sr are given in Tables X, XI, XII, XIII, and XIV, respectively. In our experiment there are few examples in which the conversion to photoproduction or the difference between the center-of-mass and the laboratory systems is statistically discernible. Table XV gives the measured values of $(C/A)_{e,pe'}$ for the electron-induced angular distributions, and the predicted values of $(C/A)_{\gamma,p} = C'/A'$ for the photon-induced angular distributions for our statistically favorable cases. Representation of the angular distribution in Legendre polynomials distributes the errors of our experiment equitably among the coefficients C_ℓ and is convenient because

$$\sigma = \int_\Omega (d\sigma/d\Omega)d\Omega = 4\pi C_0 , \qquad (37)$$

a consequence of the orthogonality of the Legendre polynomials. Since the dependence of the E-1 virtual-photon spectrum on $\alpha(E)$ and $\beta(E)$

TABLE I. Oxygen angular distribution coefficients in mb/sr for $d\sigma/d\Omega = \sum_{\ell=0}^{3} C_\ell P_\ell(\cos\theta)$ and $A + B\cos\theta + C\sin^2\theta + D\sin^2\theta\cos\theta$ derived from a least squares fit.

E_p	C_0	C_1	C_2	C_3	A	B	C	D	C/A	σ
9.02	.64 ± .05	.01 ± .04	-.35 ± .02	-.04 ± .02	.28 ± .05	.06 ± .00	.55 ± .03	-.29 ± .06	1.96 ± .36	8.1 ± .6
9.53	1.05 ± .01	.01 ± .00	-.69 ± .01	-.10 ± .02	.33 ± .02	.03 ± .00	1.07 ± .02	.01 ± .04	3.19 ± .57	13.2 ± .1
9.96	.47 ± .04	.12 ± .07	-.26 ± .04	-.03 ± .04	.20 ± .07	.16 ± .00	.40 ± .07	.08 ± .11	2.05 ± .08	5.9 ± .5
10.48	.45 ± .02	.13 ± .06	-.17 ± .03	-.03 ± .04	.28 ± .05	.17 ± .00	.26 ± .05	.10 ± .10	.94 ± .25	5.7 ± .2
11.01	.32 ± .03	.05 ± .02	-.22 ± .01	-.34 ± .02	.10 ± .04	.10 ± .00	.34 ± .02	.12 ± .04	3.39 ± .13	4.1 ± .4
11.41	.55 ± .10	.13 ± .04	-.31 ± .02	-.13 ± .03	.23 ± .11	.32 ± .00	.47 ± .02	.28 ± .06	2.04 ± .10	6.9 ± 1.3
11.84	.37 ± .02	.10 ± .03	-.17 ± .02	-.34 ± .02	.20 ± .03	.18 ± .03	.25 ± .03	.05 ± .06	1.23 ± .25	4.7 ± .3
12.25	.28 ± .01	.09 ± .03	-.11 ± .02	.01 ± .02	.17 ± .03	.10 ± .00	.17 ± .03	.08 ± .06	1.02 ± .24	3.5 ± .1

TABLE XI. Fluorine angular distribution parameters in mb/sr for $d\sigma/d\Omega = \sum_{\ell=0}^{3} C_\ell P_\ell(\cos\theta)$ and $A + B\cos\theta + C\sin^2\theta + D\sin^2\theta\cos\theta$ derived from a least squares fit. Absolute values are calculated with the assumptions stated in the text.

E_p	C_0	C_1	C_2	C_3	A	B	C	D	C/A	σ
4.18	.19 ± .07	.03 ± .03	-.04 ± .02	.00 ± .02	.15 ± .07	.03 ± .01	.06 ± .02	.02 ± .05	.42 ± .25	2.4 ± .8
4.38	.17 ± .01	.04 ± .04	-.04 ± .02	.00 ± .03	.12 ± .03	.04 ± .06	.07 ± .03	.04 ± .00	.54 ± .28	2.1 ± .1
4.88	.15 ± .02	.01 ± .02	-.04 ± .01	.00 ± .01	.11 ± .02	.02 ± .00	.06 ± .01	.01 ± .03	.52 ± .15	1.9 ± .2
5.31	.16 ± .00	.02 ± .01	-.06 ± .00	-.19 ± .00	.10 ± .00	.05 ± .00	.09 ± .00	.00 ± .01	.86 ± .05	2.0 ± .0
5.59	.16 ± .03	.01 ± .02	-.03 ± .01	.01 ± .01	.13 ± .03	.00 ± .00	.04 ± .02	.03 ± .03	.33 ± .16	2.0 ± .4
5.88	.18 ± .00	.04 ± .01	-.04 ± .00	-.01 ± .01	.13 ± .01	.06 ± .00	.06 ± .01	.03 ± .01	.48 ± .05	2.2 ± .0
6.19	.16 ± .01	.02 ± .02	-.03 ± .01	.01 ± .00	.12 ± .02	.03 ± .00	.05 ± .01	.01 ± .03	.40 ± .13	2.0 ± .1
6.57	.14 ± .00	.02 ± .01	.00 ± .01	.00 ± .01	.14 ± .01	.02 ± .00	.00 ± .01	.02 ± .02	.03 ± .06	1.7 ± .0
6.68	.15 ± .03	.01 ± .02	-.04 ± .01	.00 ± .01	.11 ± .03	.01 ± .00	.05 ± .02	.02 ± .03	.49 ± .19	1.9 ± .3
7.09	.20 ± .02	.04 ± .02	-.07 ± .01	-.01 ± .01	.13 ± .02	.05 ± .00	.11 ± .01	.03 ± .03	.79 ± .16	2.6 ± .2
7.46	.19 ± .15	.05 ± .04	-.06 ± .02	-.02 ± .02	.14 ± .15	.08 ± .00	.09 ± .03	.04 ± .06	.64 ± .70	2.4 ± 1.8
7.91	.15 ± .02	.03 ± .02	-.06 ± .01	-.02 ± .01	.09 ± .03	.05 ± .00	.09 ± .02	.02 ± .03	1.09 ± .38	1.9 ± .3
8.18	.19 ± .00	.04 ± .01	-.09 ± .00	-.02 ± .01	.10 ± .01	.07 ± .00	.14 ± .01	.02 ± .01	1.47 ± .11	2.4 ± .0
8.50	.18 ± .25	.01 ± .05	-.08 ± .03	-.03 ± .03	.09 ± .27	.05 ± .00	.13 ± .04	-.02 ± .08	1.33 ± 4.71	2.2 ± 3.1
8.81	.21 ± .01	.04 ± .03	-.12 ± .02	-.02 ± .02	.09 ± .00	.07 ± .00	.18 ± .02	.02 ± .01	1.99 ± .58	2.7 ± .1

TABLE XII. Meon angular distribution coefficients in mb/sr for $d\sigma/d\Omega = \sum_{\ell=0}^{3} C_\ell P_\ell(\cos\theta)$ and $A + B\cos\theta + C\sin^2\theta + D\sin^2\theta\cos\theta$ derived from a least squares fit.

E_p	C_0	C_1	C_2	C_3	A	B	C	D	C/A	σ
4.38	.93 ± .08	-.03 ± .06	-.24 ± .03	.02 ± .04	.68 ± .09	-.06 ± .01	.38 ± .05	-.13 ± .10	.57 ± 1.03	11.7 ± 1.0
4.59	1.37 ± .03	.14 ± .04	-.54 ± .02	-.04 ± .03	.79 ± .04	.20 ± .00	.87 ± .04	.10 ± .07	1.05 ± .08	17.2 ± .4
4.77	.97 ± .03	.30 ± .05	-.22 ± .03	-.01 ± .03	.74 ± .05	.29 ± .00	.35 ± .04	.30 ± .09	.46 ± .03	12.2 ± .4
5.00	.48 ± .00	.03 ± .01	-.09 ± .00	.31 ± .08	.39 ± .01	-.02 ± .00	.14 ± .01	.06 ± .02	.36 ± .03	6.0 ± .1
5.24	.40 ± 1.00	.03 ± .19	-.08 ± .06	.06 ± .07	.31 ± 1.01	-.06 ± .16	.13 ± .08	.09 ± .24	.42 ± 1.33	5.0 ±12.6
5.40	.57 ± .00	.00 ± .02	-.15 ± .08	.02 ± .01	.41 ± .00	.04 ± .00	.24 ± .01	.02 ± .02	.58 ± .03	7.2 ± .1
5.50	.81 ± 1.02	.11 ± .22	-.29 ± .07	-.08 ± .09	.50 ± 1.03	.24 ± .17	.46 ± .11	.03 ± .29	.92 ± 1.89	10.2 ±12.8
5.79	1.05 ± .03	.09 ± .03	-.41 ± .02	.01 ± .02	.62 ± .04	.07 ± .01	.65 ± .02	.10 ± .05	1.04 ± .08	13.2 ± .4
6.04	.77 ± .34	.13 ± .08	-.31 ± .03	-.03 ± .04	.44 ± .34	.17 ± .06	.49 ± .05	.10 ± .12	1.12 ± .87	9.7 ± 4.3
6.34	.47 ± .16	.04 ± .04	-.17 ± .02	-.02 ± .02	.29 ± .07	.07 ± .01	.27 ± .03	.02 ± .06	.91 ± .52	5.9 ± 2.1
6.67	.90 ± .00	.58 ± .12	-.33 ± .01	-.05 ± .01	.55 ± .09	.14 ± .00	.52 ± .09	.01 ± .02	.94 ± .02	11.3 ± .0
6.89	.80 ± .07	.15 ± .11	-.24 ± .05	-.04 ± .06	.55 ± .10	.20 ± .16	.38 ± .08	.11 ± .16	.69 ± .19	10.1 ± .9
7.13	.55 ± .01	.10 ± .04	-.13 ± .02	-.07 ± .03	.41 ± .04	.20 ± .00	.21 ± .04	.03 ± .07	.51 ± .10	6.9 ± .2
7.49	.56 ± .02	.07 ± .08	-.19 ± .04	.02 ± .05	.37 ± .06	.04 ± .00	.29 ± .06	.01 ± .13	.79 ± .21	7.0 ± .3
7.94	.52 ± .32	.09 ± .08	-.26 ± .03	-.10 ± .04	.25 ± .32	.24 ± .04	.41 ± .05	.01 ± .11	1.63 ± 2.10	6.6 ± 4.0
8.31	.45 ± .01	.09 ± .02	-.20 ± .01	-.33 ± .02	.25 ± .02	.14 ± .00	.30 ± .02	.06 ± .04	1.22 ± .12	5.7 ± .2
8.72	.48 ± .01	.13 ± .02	-.15 ± .01	-.13 ± .01	.32 ± .02	.33 ± .00	.24 ± .02	.00 ± .03	.76 ± .06	6.0 ± .2
9.19	.35 ± .07	.08 ± .03	-.13 ± .01	.00 ± .02	.22 ± .02	.09 ± .00	.20 ± .02	.08 ± .05	.90 ± .12	4.5 ± .9
9.49	.41 ± .38	.09 ± .10	-.16 ± .04	-.02 ± .04	.24 ± .44	.13 ± .08	.24 ± .06	.07 ± .13	1.02 ± 1.86	5.1 ± 4.8
9.85	.32 ± .01	.06 ± .98	-.06 ± .03	-.05 ± .03	.25 ± .11	.14 ± .98	.10 ± .04	.01 ± .99	.39 ± .25	4.0 ± .2

TABLE XIII. Carbon angular distribution coefficients in mb/sr for $d\sigma/d\Omega = \sum_{\ell=0}^{3} C_\ell P_\ell(\cos\theta)$ and $A + B\cos\theta + C\sin^2\theta + D\sin^2\theta\cos\theta$ derived from a least squares fit.

E_p	C_0	C_1	C_2	C_3	A	B	C	D	C/D	σ
4.23	.30 ± .01	.04 ± .02	-.10 ± .01	-.80 ± .13	.20 ± .02	.16 ± .00	.15 ± .02	-.04 ± .03	1.29 ± .17	3.9 ± .1
4.42	.39 ± .04	.07 ± .13	-.17 ± .07	-.33 ± .09	.21 ± .01	.11 ± .00	.26 ± .10	.03 ± .02	1.18 ± .46	4.9 ± .4
4.68	.46 ± .01	.06 ± .02	-.15 ± .01	-.02 ± .01	.32 ± .02	.09 ± .00	.22 ± .02	.04 ± .03	.71 ± .06	5.9 ± .1
4.93	.48 ± .04	.10 ± .03	-.21 ± .02	.07 ± .02	.26 ± .04	.20 ± .00	.32 ± .02	.03 ± .06	1.21 ± .23	6.0 ± .5
5.25	.60 ± .01	.10 ± .04	-.31 ± .02	.02 ± .03	.28 ± .04	.06 ± .01	.47 ± .03	.12 ± .03	1.48 ± .33	7.5 ± .2
5.59	.67 ± .44	.15 ± .08	-.39 ± .04	-.05 ± .05	.26 ± .05	.24 ± .00	.61 ± .06	.03 ± .10	2.38 ± .51	8.4 ± 5.5
5.90	.74 ± .04	.12 ± .06	-.45 ± .03	-.08 ± .04	.29 ± .06	.25 ± .00	.68 ± .05	.04 ± .11	2.37 ± .50	9.4 ± .4
6.42	.64 ± .02	.11 ± .05	-.47 ± .03	-.10 ± .04	.17 ± .04	.26 ± .00	.71 ± .04	.01 ± .09	4.21 ± 1.14	7.9 ± .2
6.59	.68 ± .00	.16 ± .04	-.44 ± .02	-.06 ± .02	.24 ± .03	.25 ± .00	.67 ± .03	.10 ± .06	2.81 ± .34	8.6 ± .0
6.71	.69 ± .03	.23 ± .09	-.36 ± .05	-.08 ± .06	.34 ± .08	.36 ± .00	.54 ± .08	.15 ± .16	1.60 ± .23	8.7 ± .3
6.84	.63 ± .18	.31 ± .14	-.33 ± .07	-.21 ± .09	.30 ± .21	.62 ± .00	.50 ± .11	.10 ± .23	1.69 ± 1.23	7.9 ± 2.3
7.12	.60 ± .25	.21 ± .07	-.30 ± .04	-.04 ± .05	.30 ± .25	.26 ± .00	.45 ± .06	.17 ± .12	1.50 ± 1.29	7.5 ± 3.1

TABLE XIV. Aluminum angular distribution coefficients in mb/sr for $d\sigma/d\Omega = \sum_{\ell=0}^{3} C_\ell P_\ell(\cos\theta)$ and $A + B\cos\theta + C\sin^2\theta + D\sin^2\theta\cos\theta$ derived from a least squares fit. Absolute values of the coefficients are based on the assumption $k = (27/26)E_p + 14$ as explained in the text.

E_p	C_0	C_1	C_2	C_3	A	B	C	D	C/A	σ
4.97	1.04 ± .01	.14 ± .04	-.02 ± .02	-.06 ± .03	1.01 ± .03	.23 ± .00	.03 ± .03	.07 ± .07	.03 ± .03	13.1 ± .2
5.69	.99 ± .01	.09 ± .01	.01 ± .01	.00 ± .01	1.00 ± .01	.09 ± .00	-.10 ± .10	.09 ± .02	-.10 ± .10	12.5 ± .1
6.20	1.07 ± .06	.08 ± .02	-.06 ± .01	.02 ± .01	1.01 ± .02	.05 ± .00	.10 ± .02	.10 ± .04	.09 ± .02	13.5 ± .7
6.94	.84 ± .05	.09 ± .14	-.06 ± .05	.00 ± .07	.78 ± .05	.09 ± .09	.09 ± .08	.08 ± .02	.12 ± .13	10.5 ± .6
7.63	.79 ± .05	.06 ± .07	-.05 ± .04	.01 ± .05	.74 ± .07	.04 ± .02	.08 ± .06	.08 ± .12	.11 ± .08	10.0 ± .6
8.41	.75 ± .05	.10 ± .02	.01 ± .01	.01 ± .01	.77 ± .02	.09 ± .00	-.02 ± .02	.10 ± .03	-.03 ± .02	9.4 ± .2
8.59	.68 ± .01	.12 ± .04	-.05 ± .03	-.03 ± .03	.63 ± .04	.17 ± .00	.07 ± .04	.09 ± .07	.12 ± .06	8.5 ± .2

vanishes on integration over $d\Omega$, the E-1 $\sigma(e,pe')$ is predicted to be equal to the E-1 $\sigma(\gamma,p)$.

TABLE XV. Measured values of $(C/A)_{e,pe'}$ for $(d\sigma/d\Omega)_{e,pe'}$ and predicted values of $(C/A)_{\gamma,p}$ for $(d\sigma/d\Omega)_{\gamma,p}$.

Element	Oxygen	Oxygen	Neon	Neon
E_p (Mev)	9.53	11.41	4.59	6.67
$(C/A)_{e,pe'}$	2.90 ± .19	1.94 ± .10	1.00 ± .09	0.87 ± .02
$(C/A)_{\gamma,p}$	3.19 ± .19	2.04 ± .10	1.05 ± .09	0.94 ± .02

(a) Oxygen. The O $d\sigma(\gamma,p)/d\Omega$ has been studied in this energy range by Johannson et al.,[12] C. Milone et al.[69] and Brix and Mashke[70]; but the accuracy of previous experiments has been limited by experimental[70] or statistical uncertainties.[12,69] Ratios of C'/A' range from 1.1 obtained by Johannson et al. to 6.7 obtained by Brix and Mashke for $E_p > 10$ Mev. Our values of C'/A' are shown in Fig. 33. The $d\sigma/d\Omega$ of O protons from the 9.53 and 11.50-Mev peaks and the valley in between are displayed in Fig. 34. Wilkinson's resonance direct mechanism predicts $C'/A' = 3/2$ for both the $1p_{3/2}$ to $1d_{5/2}$ transitions and the $1p_{1/2}$ to $1d_{3/2}$ transitions which are expected to be responsible for the 9.53 and 11.50-Mev peaks, respectively. Admixtures of transitions where the relative angular momentum of the proton ℓ changes to $\ell - 1$ with the transitions where ℓ changes to $\ell + 1$, which contribute most of the dipole

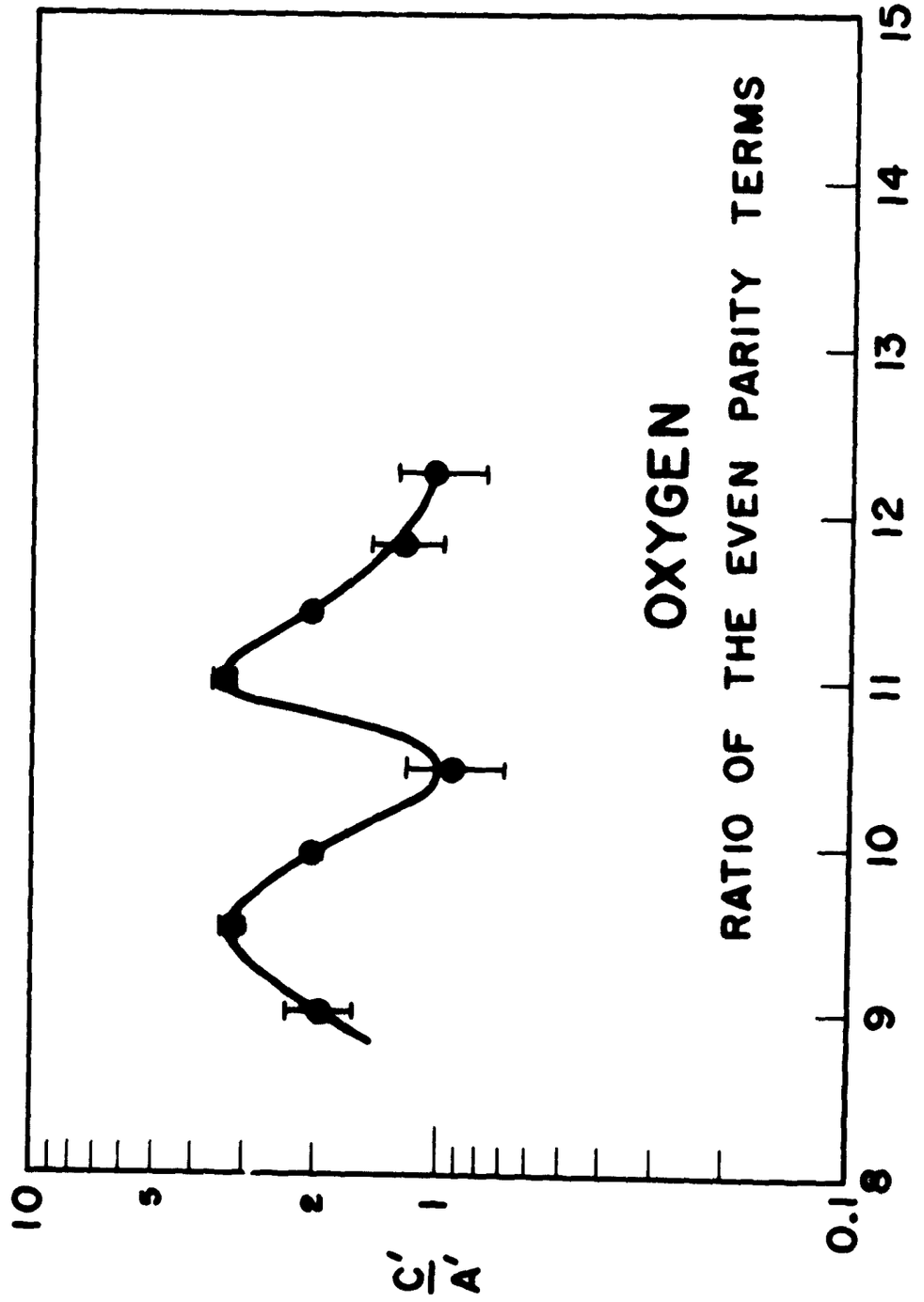
OXYGEN
RATIO OF THE EVEN PARITY TERMS
C'/A'
PROTON ENERGY (MEV)
10
5
2
1
0.1
8
9
10
11
12
13
14
15

FIGURE 33

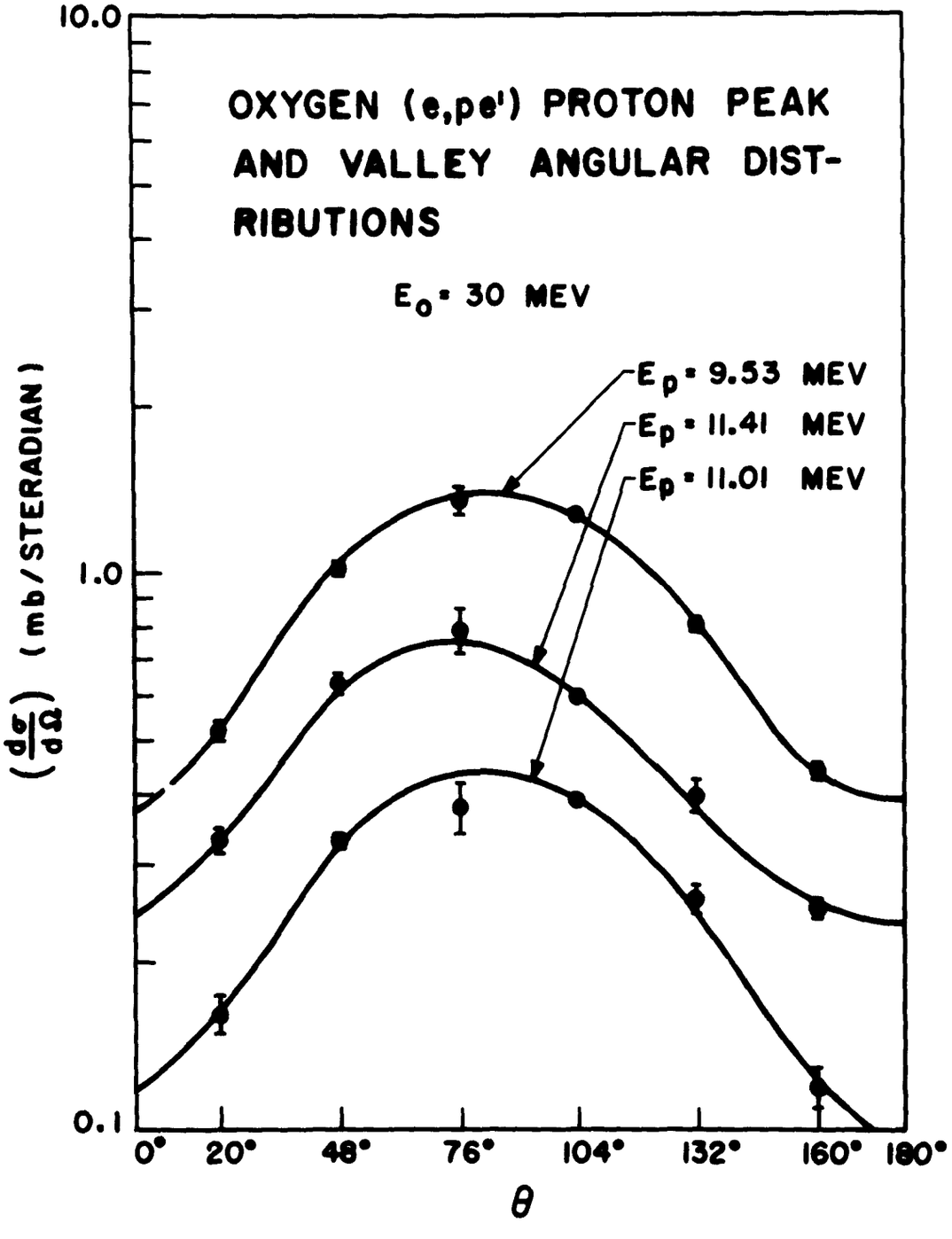
OXYGEN (e,pe') PROTON PEAK AND VALLEY ANGULAR DISTRIBUTIONS
E_0 = 30 MEV
E_p = 9.53 MEV
E_p = 11.41 MEV
E_p = 11.01 MEV
$\left(\frac{d\sigma}{d\Omega}\right)$ (mb/STERADIAN)
10.0
1.0
0.1
0°
20°
48°
76°
104°
132°
160°
180°
θ

FIGURE 34

strength can modify the simple estimates for C/A of Courant[71] and Wilkinson,[6] since the radial matrix elements cannot be factored out in these cases.[72] Calculations of the expected modification of C'/A' have not been extended to this region of Z . Figure 35 shows that the asymmetry in O d (e,pe')/dΩ shifts from the backward to the forward hemisphere, respectively, for protons from the low- and high-energy sides of the 9.53-Mev peak. As Gove[73] has pointed out, this behavior is expected if the asymmetry term arises from interference of two proper Breit-Wigner resonances, one with $J\pi = 1^-$ and the other with $J\pi = 2^+$, and whose spacing is greater than their widths to ensure the physical reasonableness of the single-level Breit-Wigner approximation. The inelastic electron scattering experiments of Bishop and Isabelle[74] indicate the presence of an E-2 level in this vicinity of the photon absorption cross section. Brown and Levinger[75] have placed an upper limit on $\sigma_{E-2}/\sigma_{E-1}$ of $p^2/20$, where $p = C/D$. For O this formula predicts $\sigma_{E-2}/\sigma_{E-1} < 1.8\%$ for the proton energy interval investigated.

(b) Fluorine. The F $d\sigma(\gamma,p)/d\Omega$ C'/A' values (Fig. 36) are ~ .5 for $E_p < 7$ Mev, while for $E_p > 7$ Mev they increase rapidly with E_p . The low values of C'/A' imply either a large component of a statistical emission process or a large proton relative angular momentum ℓ . (According to the resonance direct theories $d\sigma/d\Omega \approx 1 + 1/2 \sin^2\theta$ for large ℓ .) The latter assumption would partially explain the low F^{19} $\int \sigma(\gamma,p)dE_\gamma$ because of the angular momentum barrier; but the (γ,n) yields would also be inhibited by this mechanism. According to the F^{19} $\sigma(\gamma,n)$ E_γ measurements of Ferguson et al.,[48] this inhibition is not observed.

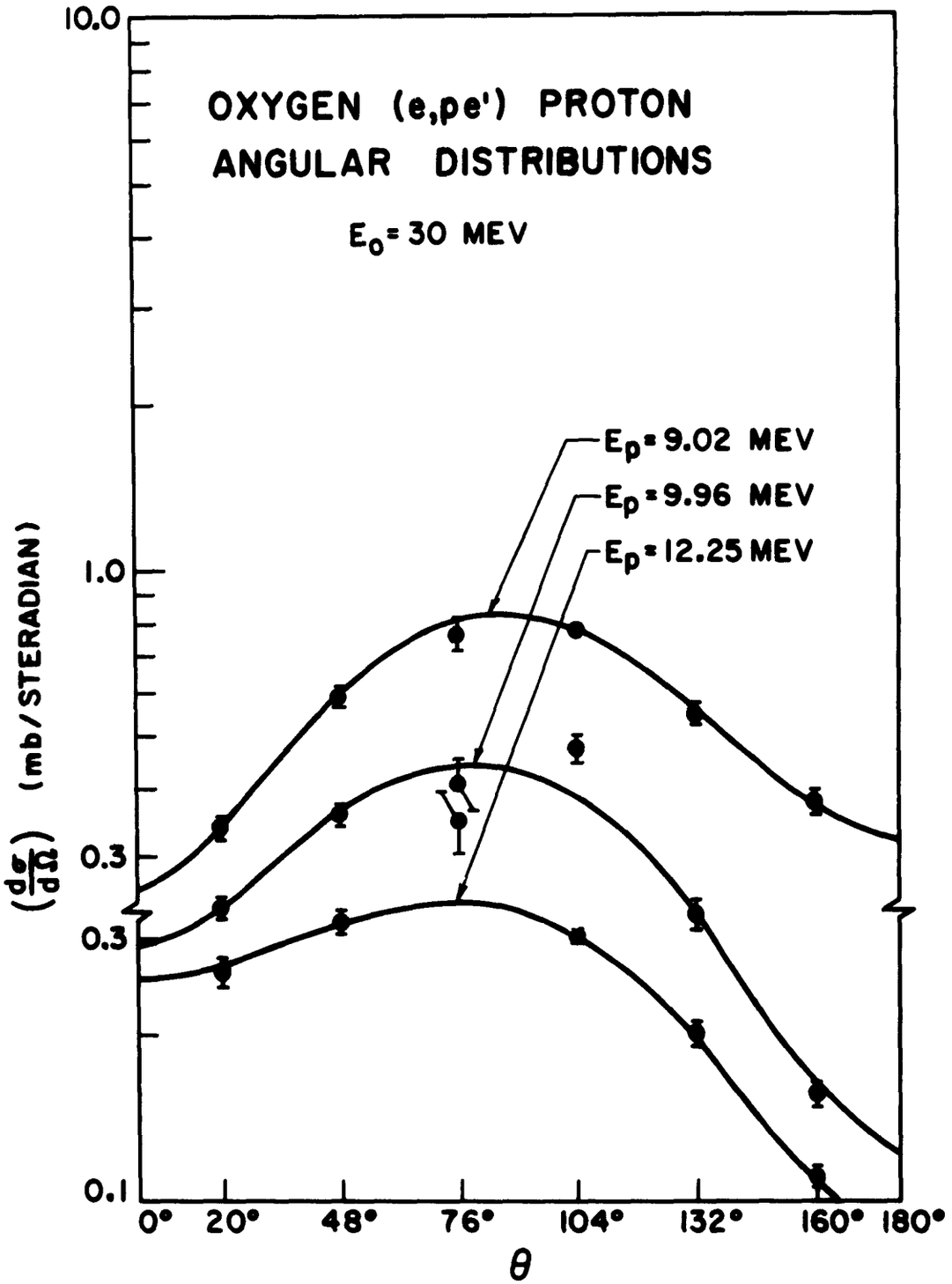
OXYGEN (e,pe') PROTON
ANGULAR DISTRIBUTIONS
E_0 = 30 MEV
E_p = 9.02 MEV
E_p = 9.96 MEV
E_p = 12.25 MEV
$\left(\frac{d\sigma}{d\Omega}\right)$ (mb/STERADIAN)
10.0
1.0
0.3
0.3
0.1
0°
20°
48°
76°
104°
132°
160°
180°
θ

FIGURE 35

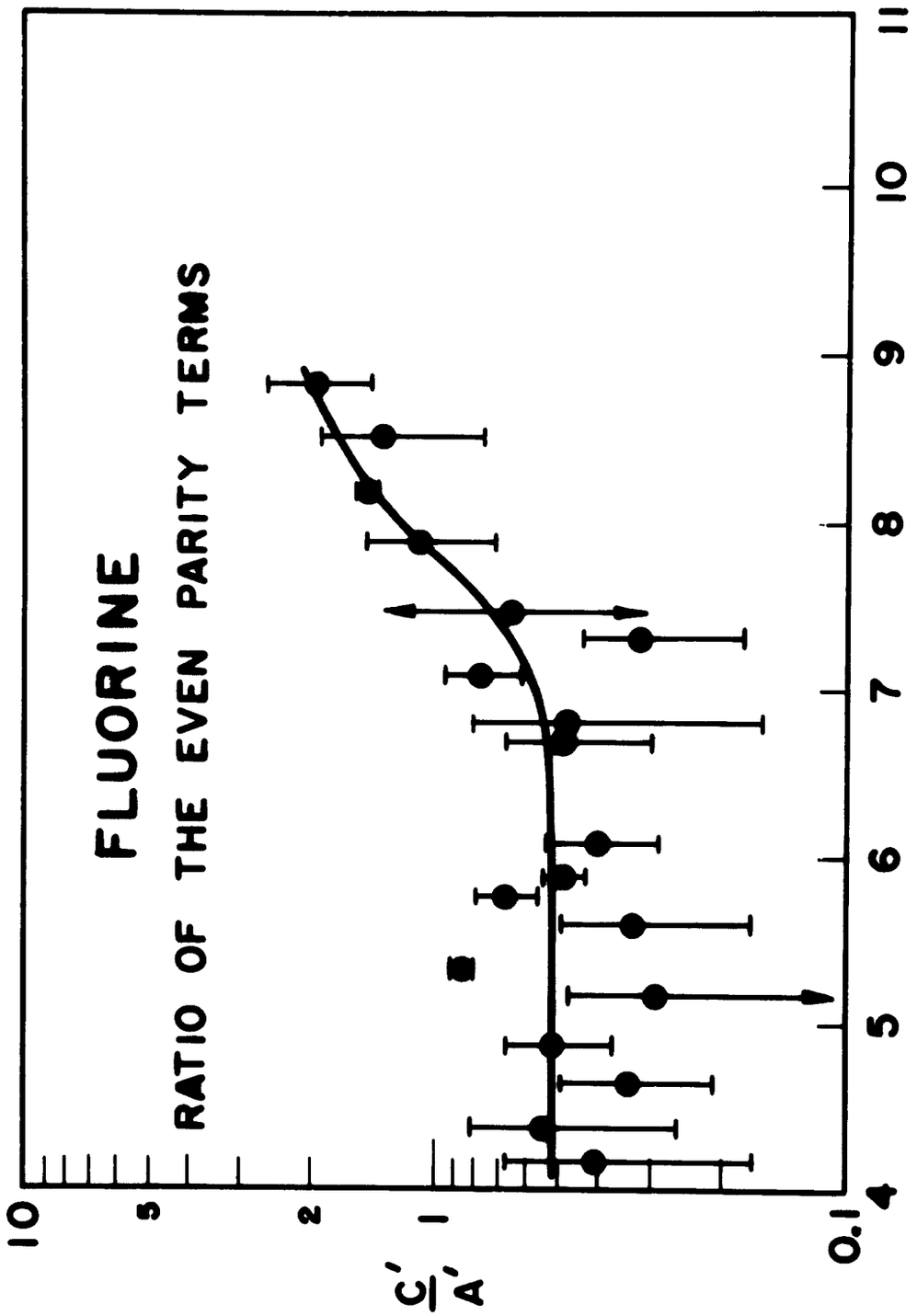
FLUORINE
RATIO OF THE EVEN PARITY TERMS
C'/A'
10
5
2
1
0.1
4
5
6
7
8
9
10
11
PROTON ENERGY (MEV)

FIGURE 36

Typical F $d\sigma(e,pe')/d\Omega$'s for E_0 = 24.5 Mev are shown in Fig. 37 with arbitrary ordinate units. The absolute values of the angular distribution coefficients which were given in Table XI were calculated from the F $d\sigma(e,pe')/d\Omega$ at 76° shown in Fig. 16.

(c) Neon. The Ne $d\sigma(e,pe')/d\Omega$ exhibits the same general behavior as O although C'/A' values (Fig. 38) are smaller — a significant fact since a resonant-state interaction with the valence nucleons which would produce a larger isotropic term than occurs in O seems unlikely in view of the sharper peaks in the Ne cross section. The similarity of shape of $d\sigma/d\Omega$ for the peak protons (which all have $C'/A' \approx 1$) is stressed in Fig. 39. The shift from backward to forward asymmetry on opposite sides of a peak, observed in O, is also seen for the second Ne peak in the $d\sigma/d\Omega$ of the 5.40- and 6.04-Mev protons in Fig. 40, along with the $d\sigma/d\Omega$ for the protons from the sides of other peaks. The angular distributions of Ne valley protons are shown in Fig. 41. According to the work of Komar and Iavor[50] the average value of C'/A' for $1 < E_p < 15$ Mev has increased to 2.5 for $E_{\gamma\ max}$ = 80 Mev. An upper limit for $\sigma_{E-2}/\sigma_{E-1}$ is 3.6% from our work, although the average value is ~1%.

(d) Carbon. The C $d\sigma(\gamma,p)d\Omega$ has been measured by many experimenters for the direct reaction, and by Gove et al.[63] for the inverse reaction. The agreement of the direct and inverse proton and photon angular distributions has been cited previously[60, 63] as quantitative confirmation of detailed balance. Table XVI summarizes the existing data for the $C^{12}(\gamma,p_0)$ proton and $B^{11}(p,\gamma_0)$ photon angular distributions. The C^{12} $d\sigma(e,pe')/d\Omega$

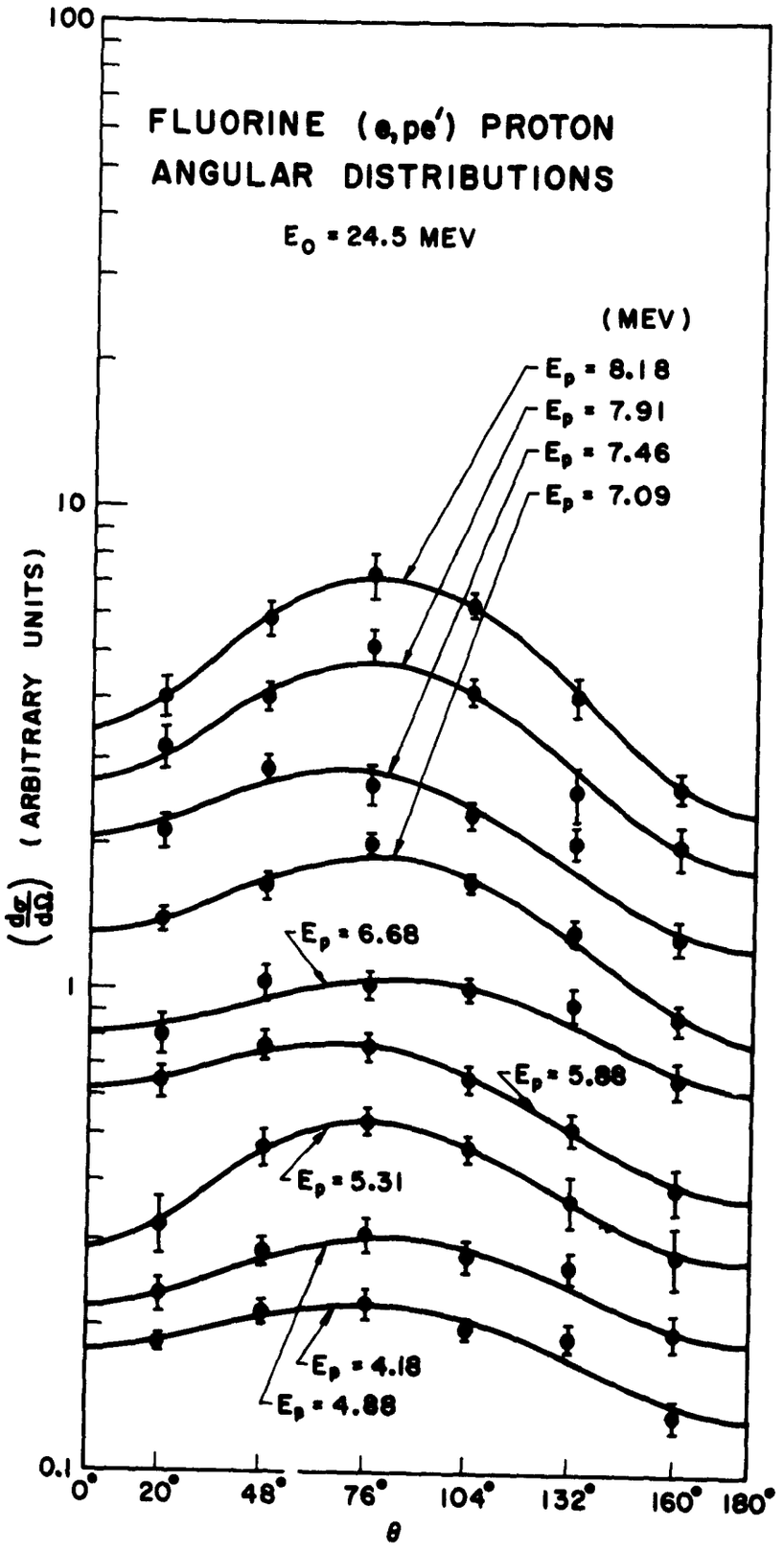
FLUORINE (e,pe′) PROTON
ANGULAR DISTRIBUTIONS
E_0 = 24.5 MEV
(MEV)
E_p = 8.18
E_p = 7.91
E_p = 7.46
E_p = 7.09
E_p = 6.68
E_p = 5.88
E_p = 5.31
E_p = 4.18
E_p = 4.88
$\left(\frac{d\sigma}{d\Omega}\right)$ (ARBITRARY UNITS)
100
10
1
0.1
0°
20°
48°
76°
104°
132°
160°
180°
θ

FIGURE 37

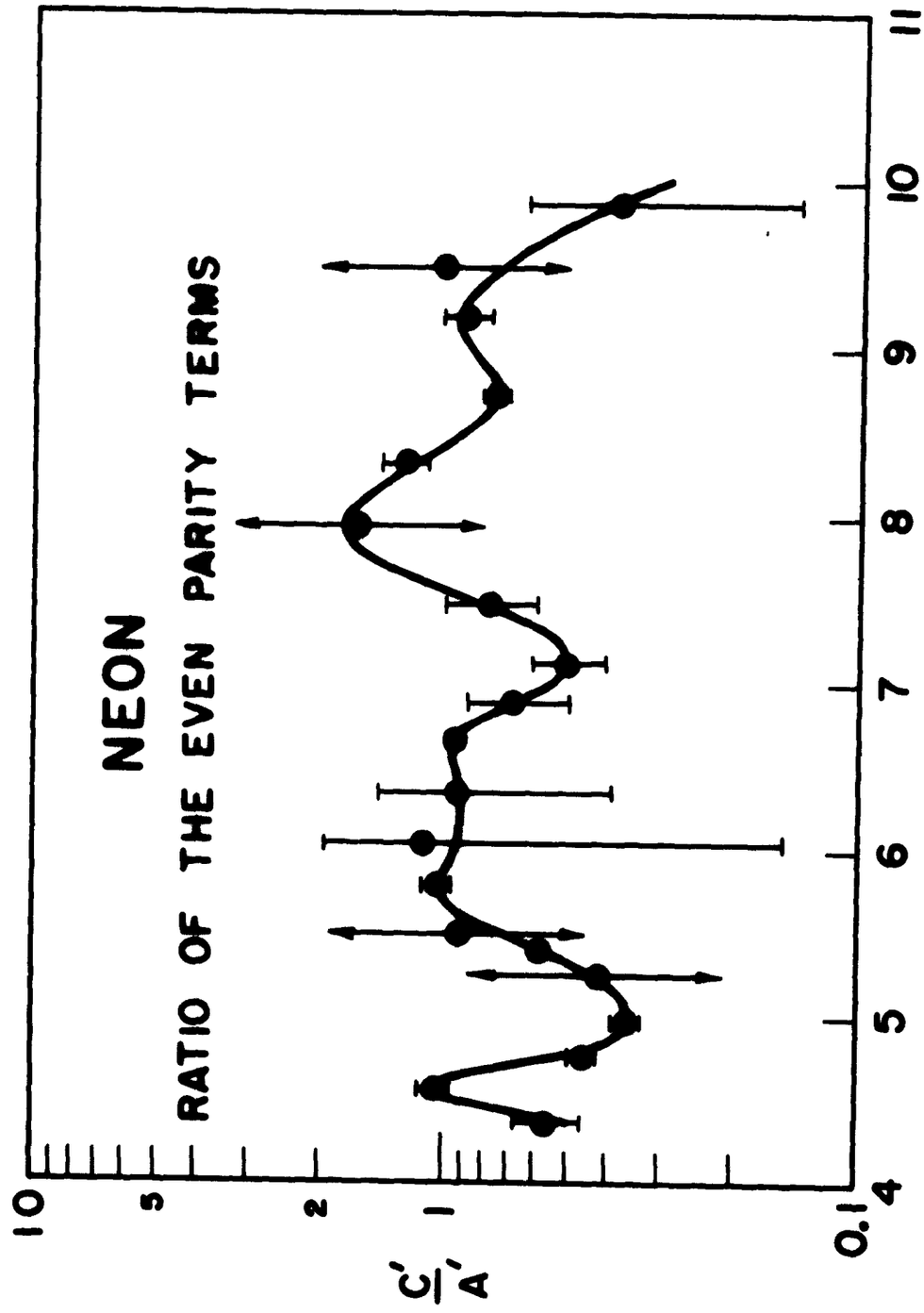
NEON
RATIO OF THE EVEN PARITY TERMS
C/A
10
5
2
1
0.1
4
5
6
7
8
9
10
11
PROTON ENERGY (MEV)

FIGURE 38

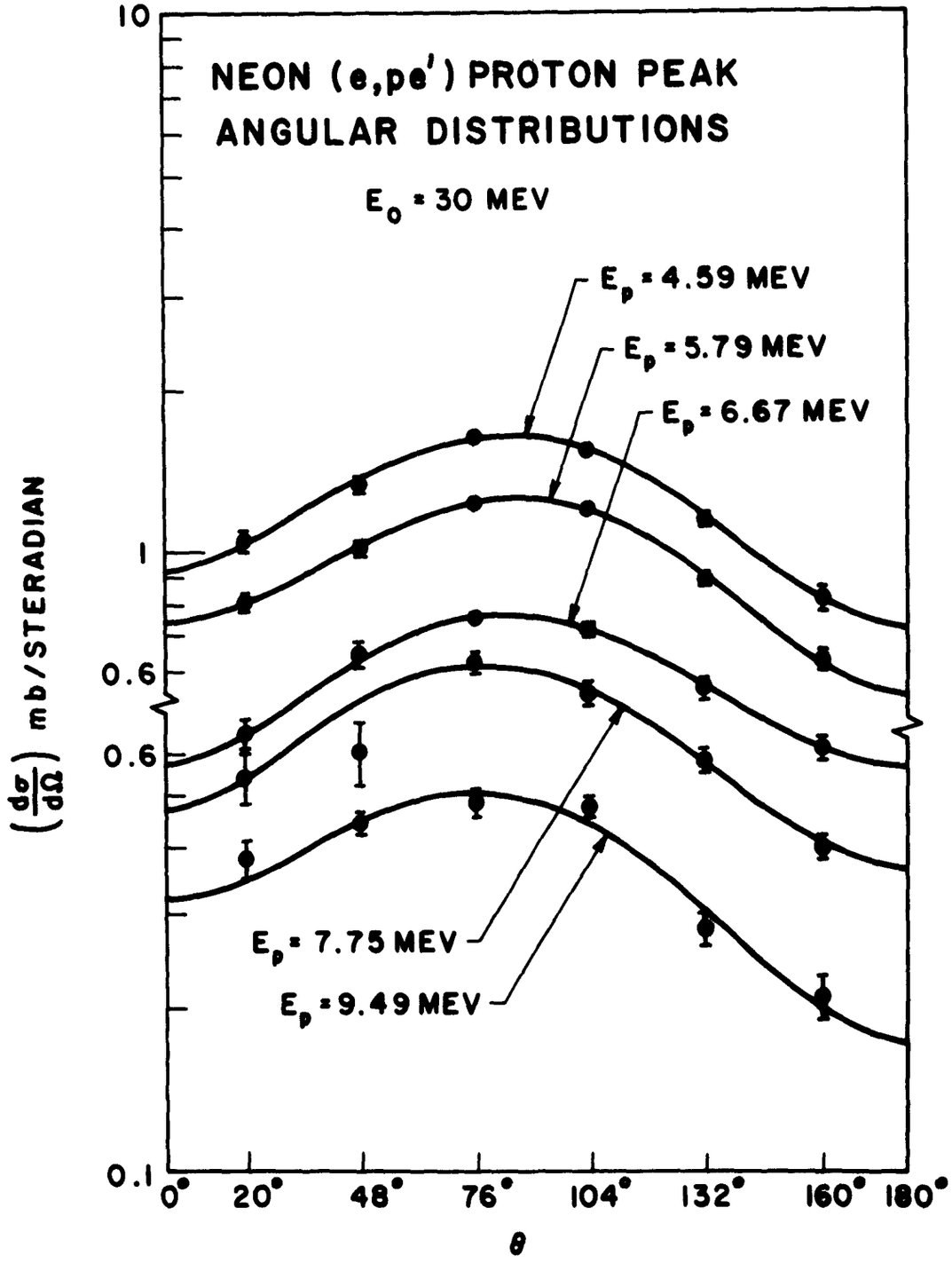
NEON (e,pe') PROTON PEAK
ANGULAR DISTRIBUTIONS
E0 = 30 MEV
Ep = 4.59 MEV
Ep = 5.79 MEV
Ep = 6.67 MEV
Ep = 7.75 MEV
Ep = 9.49 MEV
(dσ/dΩ) mb/STERADIAN
10
1
0.6
0.6
0.1
0°
20°
48°
76°
104°
132°
160°
180°
θ

FIGURE 39

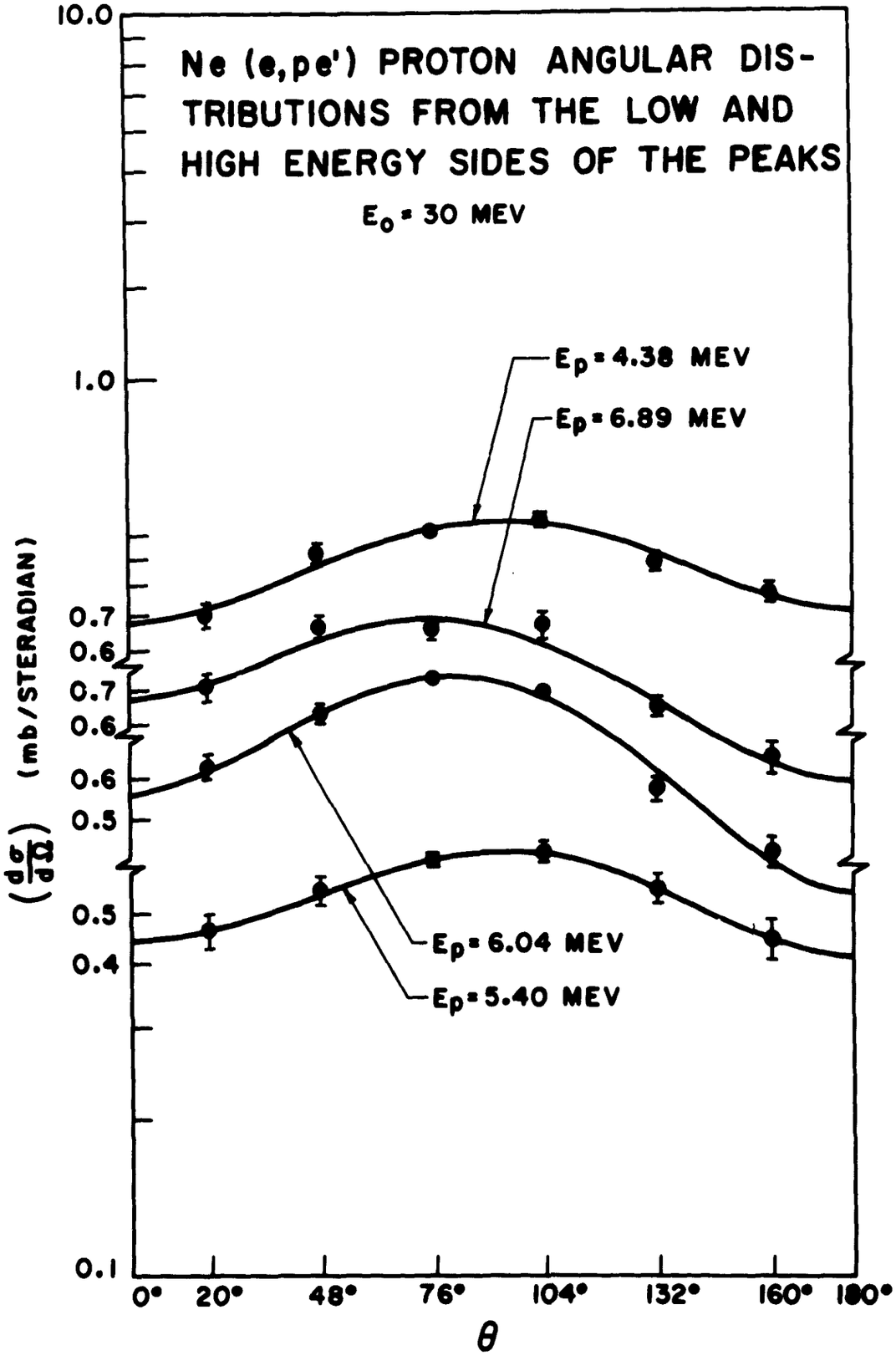
Ne (e,pe') PROTON ANGULAR DISTRIBUTIONS FROM THE LOW AND HIGH ENERGY SIDES OF THE PEAKS
E_0 = 30 MEV
E_p = 4.38 MEV
E_p = 6.89 MEV
E_p = 6.04 MEV
E_p = 5.40 MEV
$\left(\frac{d\sigma}{d\Omega}\right)$ (mb/STERADIAN)
10.0
1.0
0.7
0.6
0.7
0.6
0.6
0.5
0.5
0.4
0.1
0°
20°
48°
76°
104°
132°
160°
180°
θ

FIGURE 40

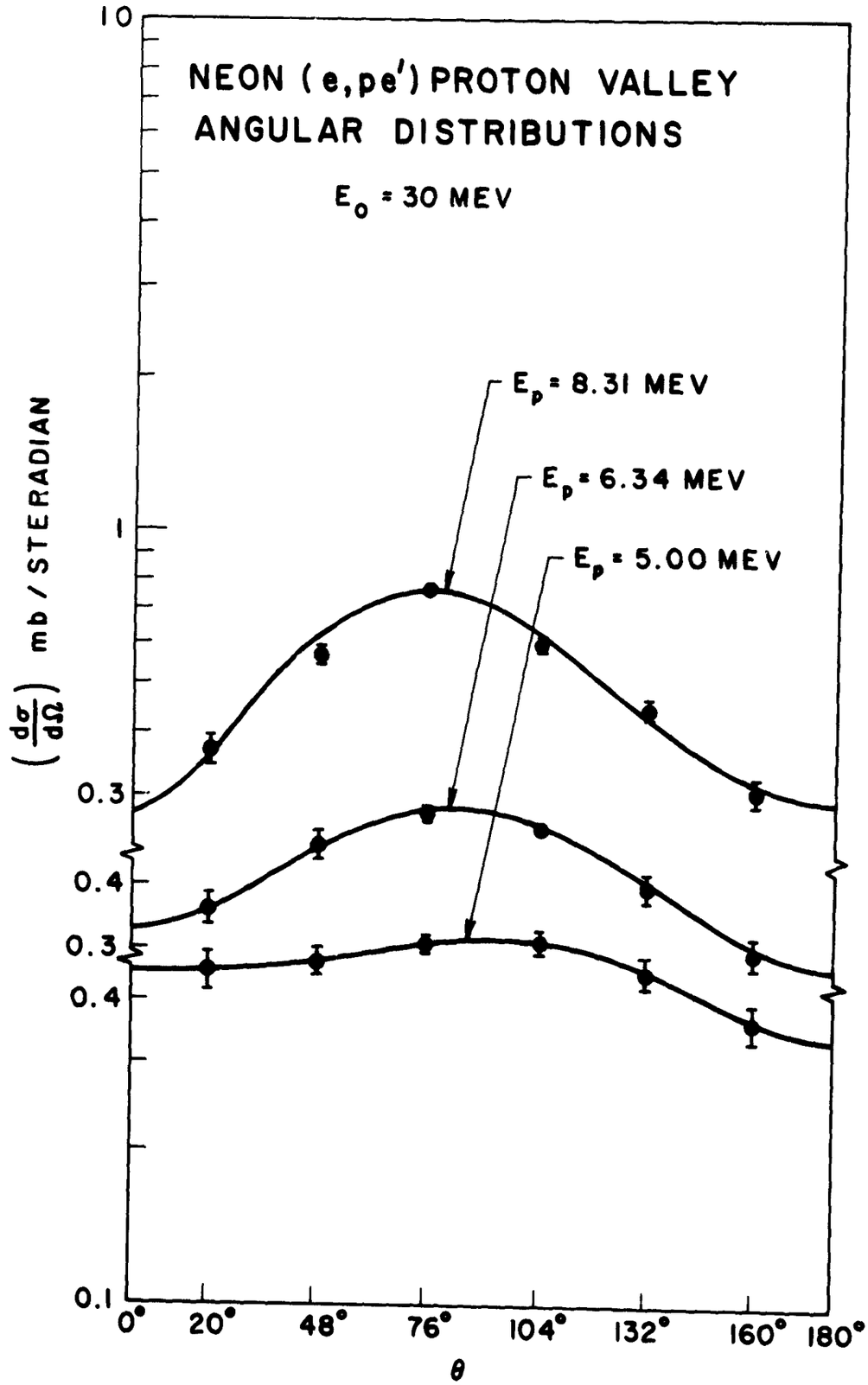
NEON (e,pe') PROTON VALLEY
ANGULAR DISTRIBUTIONS
E_0 = 30 MEV
E_p = 8.31 MEV
E_p = 6.34 MEV
E_p = 5.00 MEV
$\left(\frac{d\sigma}{d\Omega}\right)$ mb / STERADIAN
10
1
0.3
0.4
0.3
0.4
0.1
0°
20°
48°
76°
104°
132°
160°
180°
θ

FIGURE 41

for $E_p < 6.00$ Mev are shown in Fig. 42. Proton angular distributions from both sides of σ_{max} are shown in Fig. 43; the C'/A' values for C are plotted in Fig. 44. The resonance direct prediction with LS coupling is $C/A = 3/2$.

TABLE XVI. Comparison of the direct and inverse $C^{12}(\gamma,p)$ angular distribution coefficients. The errors of this experiment are standard deviations.

Experiment	E_γ	C_0	C_1	C_2	C_3
Ref.59. $C^{12}(e,pe')$	22-23	1	.14 ± .02	-.50 ± .03	———
Ref.60. $C^{12}(\gamma,p_0)$	22.1	1 ± .02	.09 ± .02	-.56 ± .04	-.03 ± .05
Ref.62. $B^{11}(p,\gamma_0)$	22.5	1	.12 ± .03	-.69 ± .05	———
This experiment	22.4	1 ± .05	.16 ± .09	-.61 ± .04	.11 ± .06

(e) Aluminum. Al angular distributions are almost isotropic (Fig. 45). They have a slight forward asymmetry which suggests interference of states of opposite parity. The Al $d\sigma(\gamma,p)/d\Omega$ measurements of Hoffman and Cameron[76] at 30°, 60°, and 90° with $E_{\gamma\ max} = 25$ Mev suggest an isotropic angular distribution in agreement with our data. Our nearly isotropic angular distributions contradict Baglin et al.'s[67] hypothesis of a relative Al (γ,p) angular momentum of $\ell = 3$. The absolute values of the coefficients which were given in Table XIV were calculated from the Al $d\sigma(e,pe')/d\Omega$ shown in Fig. 31. Equation (33) shows that multiple scattering of the

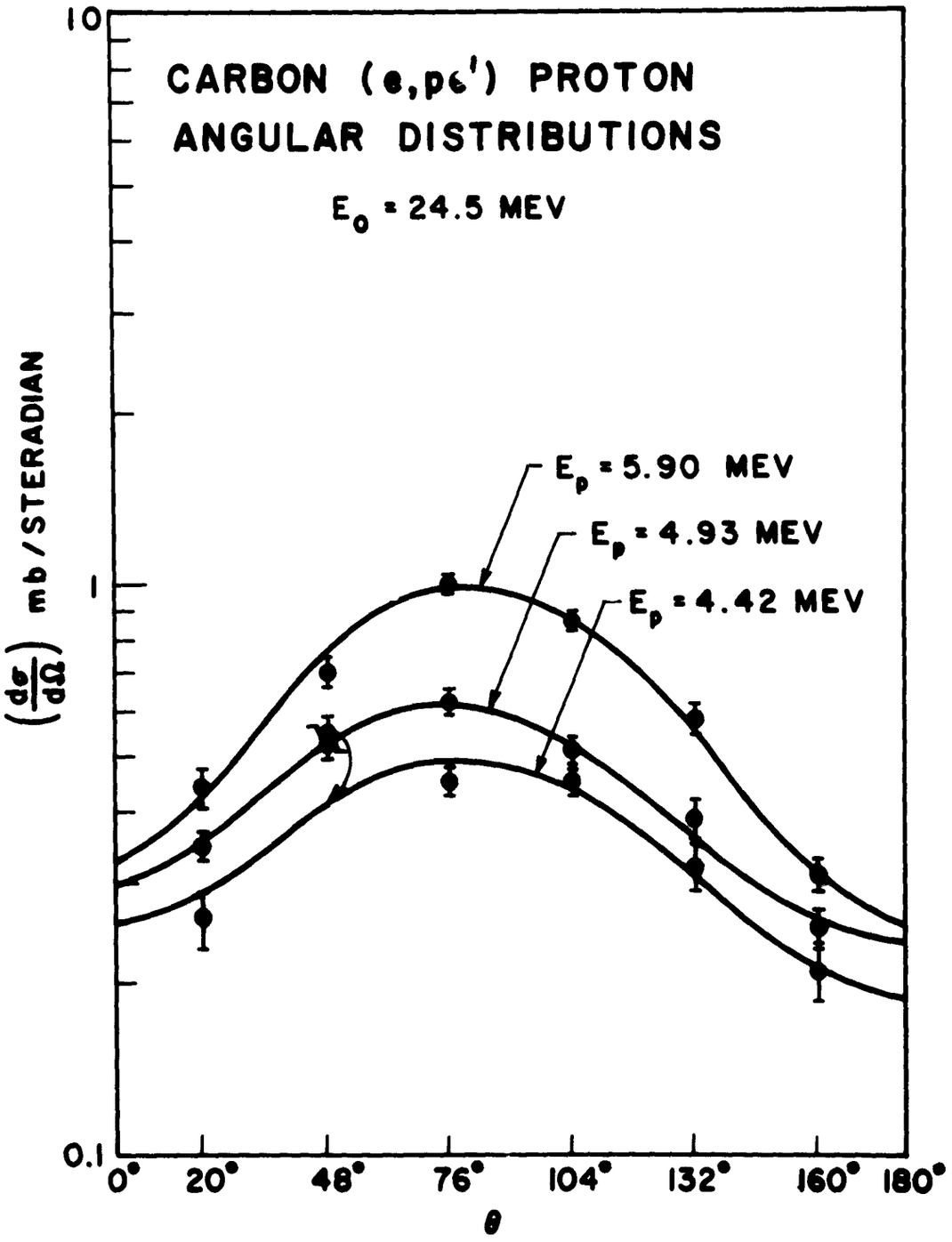
CARBON (e,pc') PROTON
ANGULAR DISTRIBUTIONS
E_0 = 24.5 MEV
E_p = 5.90 MEV
E_p = 4.93 MEV
E_p = 4.42 MEV
$\left(\frac{d\sigma}{d\Omega}\right)$ mb / STERADIAN
10
1
0.1
0°
20°
48°
76°
104°
132°
160°
180°
θ

FIGURE 42

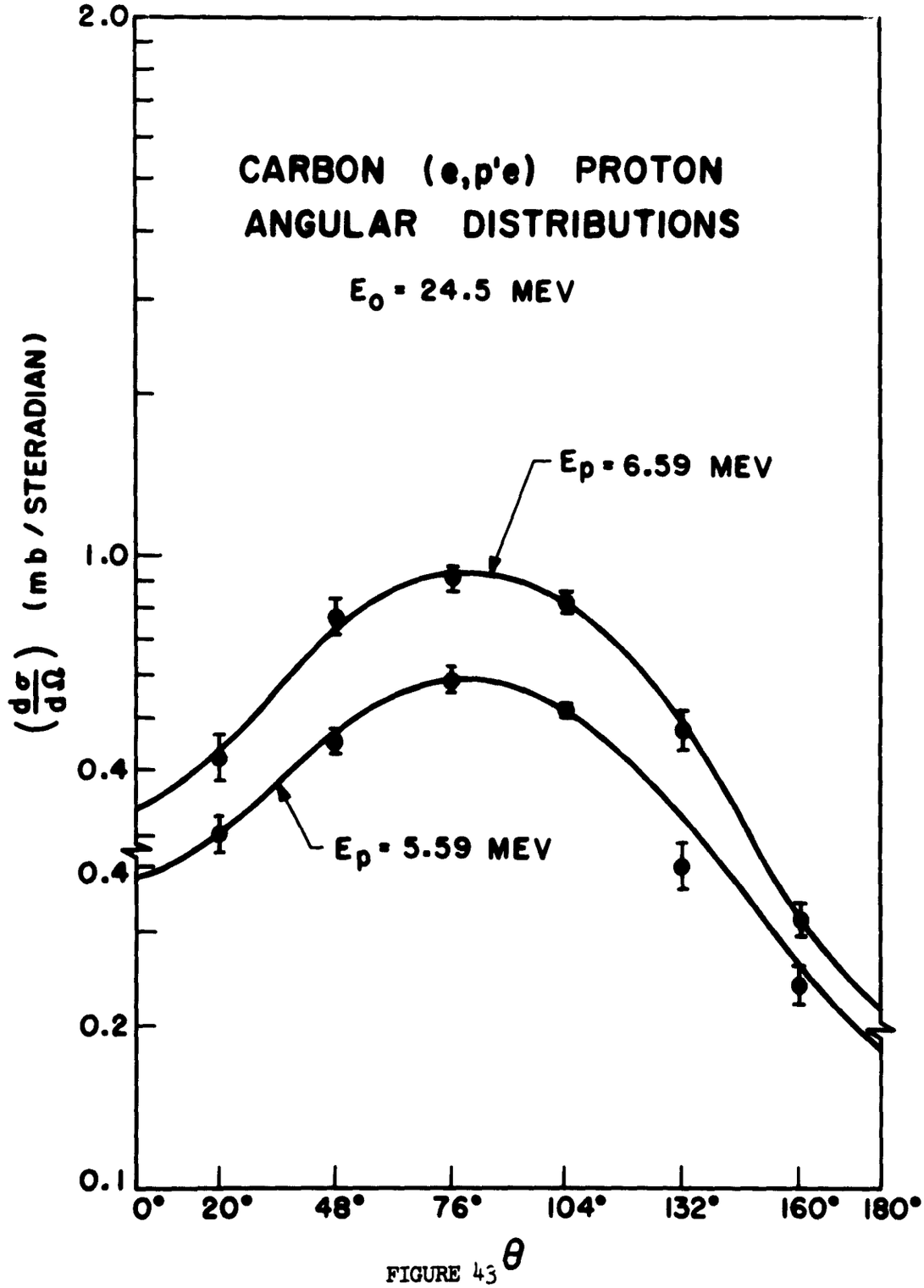
CARBON (e,p'e) PROTON
ANGULAR DISTRIBUTIONS
E_0 = 24.5 MEV
E_p = 6.59 MEV
E_p = 5.59 MEV
$\left(\frac{d\sigma}{d\Omega}\right)$ (mb / STERADIAN)
2.0
1.0
0.4
0.4
0.2
0.1
0°
20°
48°
76°
104°
132°
160°
180°
θ

FIGURE 43

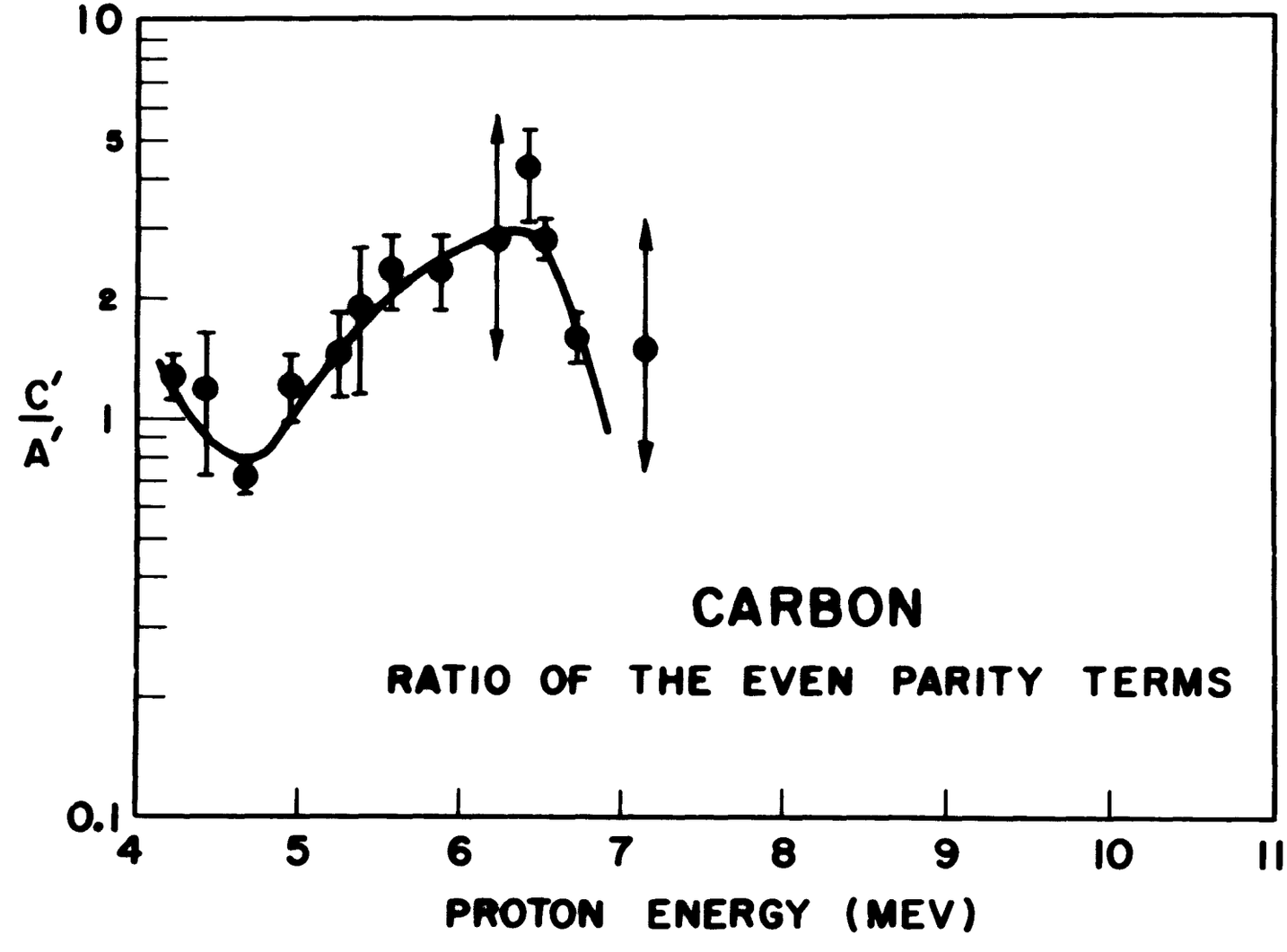
10
5
2
1
0.1
C'/A'
CARBON
RATIO OF THE EVEN PARITY TERMS
4
5
6
7
8
9
10
11
PROTON ENERGY (MEV)

FIGURE 117

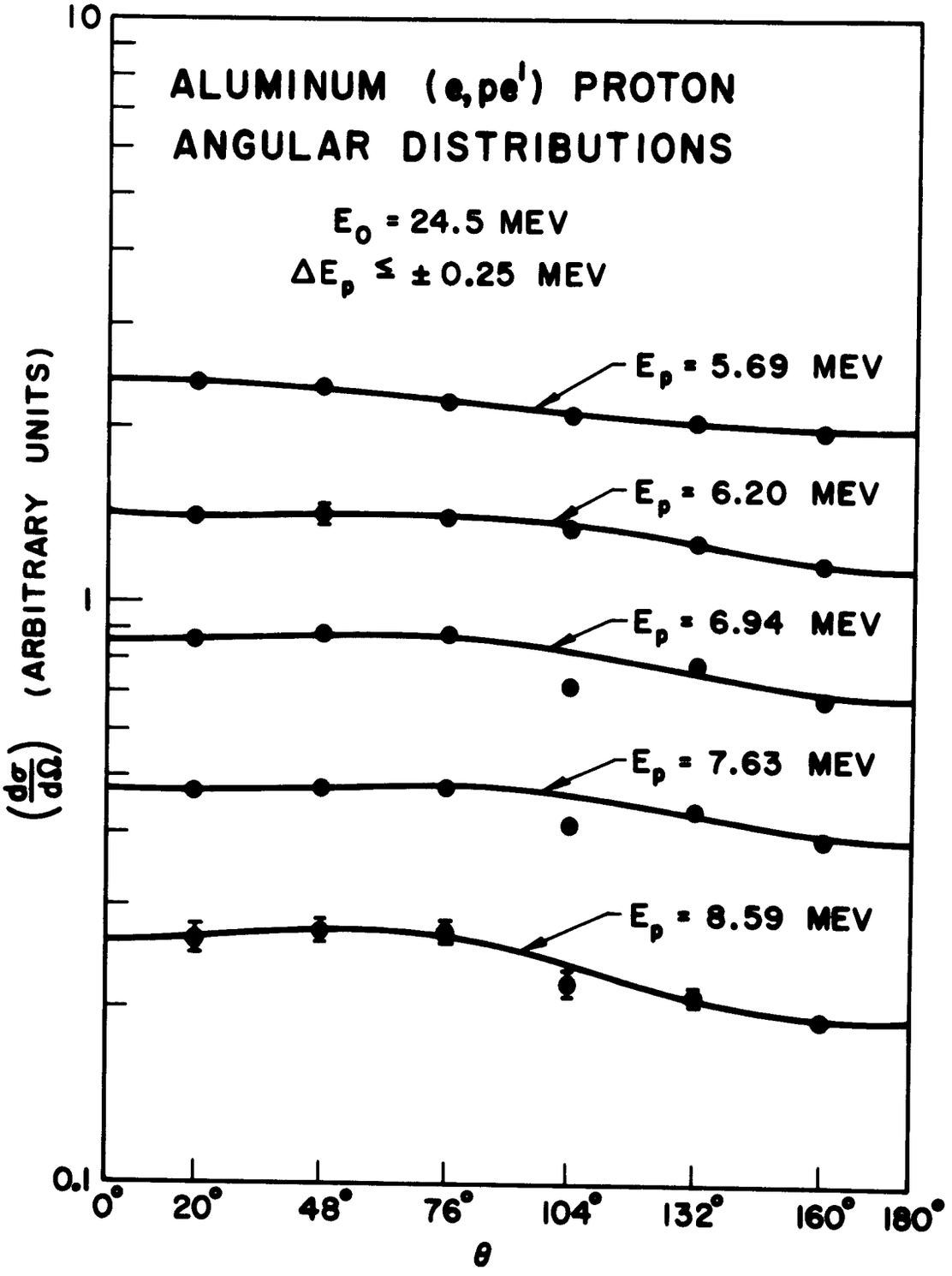
ALUMINUM (e,pe') PROTON
ANGULAR DISTRIBUTIONS
E_0 = 24.5 MEV
$\Delta E_p \leq \pm 0.25$ MEV
E_p = 5.69 MEV
E_p = 6.20 MEV
E_p = 6.94 MEV
E_p = 7.63 MEV
E_p = 8.59 MEV
$\left(\frac{d\sigma}{d\Omega}\right)$ (ARBITRARY UNITS)
10
1
0.1
0°
20°
48°
76°
104°
132°
160°
180°
θ

FIGURE 45

primary electron beam (σ_{max} = 2.1° for cases in which the electron beam traversed ~ 41.6 mg/cm^2 of Al) had a negligible effect on the Al angular distributions.

CHAPTER IV

CONCLUSIONS

Our experiments provide information about the (e,pe') reaction, and as a consequence of the correspondence between electron and photon-induced reactions, about the (γ,p) reaction in O, F, Ne, C, Al, and to a lesser extent in A and B. This information is of sufficient precision to motivate the expenditure of the considerable amount of theoretical labor which will be necessary to obtain quantitative understanding of our results. The following observations summarize the important implications of our work.

Our (e,pe') energy-distribution experiments have shown that gross structure of multiplicity greater than two does occur in the giant-resonance region in the (e,pe') reaction in O, F, and Ne. The occurrence of structure in F and Ne contradicts the predictions of the strong-correlation models of the photonuclear effect.[2,3] The quasi-agreement of the independent-particle model (IPM) calculations[7] with our O $\sigma(\gamma,p)$ and the mere occurrence of the structure in the F and Ne $\sigma(\gamma,p)$ are strong arguments for the validity of the independent-particle approach to the photonuclear effect in this region of Z . On the other hand, the O (γ,p) IPM calculations of Elliot and Flowers,[7] while not comprehensive enough to predict all the structure in the O $\sigma(\gamma,p)$ (their calculations only semi-quantitatively account for the location and relative $\int \sigma dE_\gamma$'s of the 9.5 and 11.5 Mev peaks), do not seem to predict the proper (γ,p) branching ratios to the 6.33-Mev (probably $3/2^-$) state and the ground ($1/2^-$) state of N^{15}. Their branching-ratio prediction of 3.3 to 1 in favor of the $3/2^-$ state would imply that the

region of the O (γ,p) cross section from 20 to 26 Mev would contain an anomalously high 39% of the dipole sum-rule integrated cross-section prediction of 360 Mev-mb, compared with our value $0^{16} \int_{20}^{26} \sigma(\gamma,p)dE_\gamma$ of 32.4 Mev-mb. This serious and important discrepancy warrants further experimentation to determine the ratio of the ground to the excited states of N^{15} populated by the 0^{16} (γ,p) reaction for proton energies of less than 8 Mev.

As stated in the Introduction (Chapter I) detailed IPM calculations with which to compare our experimental results are not available; however, the following qualitative conclusions can be stated. Since one of the fundamental hypotheses of Wilkinson's IPM of the giant resonance is that the largest E-1 contributions come from closed-shell transitions (transitions involving the O core in the case of F and Ne), the IPM predicts the giant resonance proton-energy spectra of O, F, and Ne should be nearly the same: the presence of the F and Ne valence nucleons should merely broaden the peaks[8] observed in the O $\sigma(\gamma,p)$. In particular, since Ne has only one more valence nucleon than F, their energy spectra should be nearly indentical. By the same reasoning the O, F, and Ne $d\sigma/d\Omega$'s should be similar. Experiment shows that none of these detailed IPM expectations are fulfilled. Thus while the collective model's photonuclear predictions are not realized in this region of Z , the IPM predictions are not correct either. The occurrence of narrow resonances does seem to indicate, however, that the crude IPM wave functions should provide the better basis for a more accurate perturbation calculation of the photonuclear effect.

One additional remark may be made. Carbon, O, and Ne are α-particle nuclei, and our experiments have shown that these nuclei have smaller giant resonance "widths" than their non-α-particle neighbors, B and F.

This condition seems to prevail in photonuclear reactions in heavy α-particle nuclei. Before extensive conjecture on this subject is made, more experiments are advisable. However, our angular distributions data provide an argument for O and Ne being more symmetric than F. This would be expected on the basis of the higher spacial symmetry which an α-particle nucleus would attain.

REFERENCES

1. D. H. Wilkinson, Ann. Rev. Nuclear Sci. 9, 1 (1959).

2. D. H. Wilkinson, Ibid. p. 18.

3. B. M. Spicer, Australian J. Phys. 11, 490 (1958).

4. M. Danos, Nuclear Phys. 5, 23 (1958).

5. G. Rakavy, Nuclear Phys. 4, 375 (1957).

6. D. H. Wilkinson in Proceedings of the 1954 Glasgow Conference on Nuclear and Meson Physics (Pergamon Press, London, 1955) pp. 161 - 167.

7. J. P. Elliot and B. H. Flowers, Proc. Roy. Soc. (London) A-242, 57 (1957).

8. G. E. Brown, L. Castillejo, and J. A. Evans in Contributions to the Karlsruhe Conference 1960 (Erstes Physikalisches Institut der Universität Heidelberg, Heidelberg, 1961), p. B-4.

9. B. H. Flowers and J. P. Elliot, Proc. Roy. Soc. (London) A-229, 537 (1955).

10. D. H. Wilkinson, Physica 22, 1149A (1956); and Phil. Mag. 3, 567 (1958).

11. A. S. Davydov and G. F. Filippov, Nuclear Phys. 8, 237 (1955); 12, 58 (1959).

12. W. E. Stephens, A. K. Mann, B. J. Patton, and E. J. Winhold, Phys. Rev. 98, 839 (1955).

13. A. E. Sven Johansson and B. Forkman, Arkiv Fysik 12, 359 (1957).

14. U. Hegel and E. Finckh, Z. Physik 162, 142 (1961).

15. G. C. Thomas and N. W. Tanner in Contributions to the Karlsruhe Conference 1960 (Erstes Physikalisches Institut der Universität Heidelberg, Heidelberg, 1961), p. P-6 (post deadline paper).

16. E. Guth and C. J. Mullin, Phys. Rev. 76, 234 (1949).

17. R. H. Dalitz and D. R. Yennie, Phys. Rev. 105, 1598 (1957); and elsewhere in the same article.

18. K. L. Brown and R. Wilson, Phys. Rev. 93, 443 (1954).

19. R. L. Hines, Phys. Rev. 105, 1534 (1957).

20. B. Bosco and S. Fubini, Nuovo cimento 9, 350 (1958).

21. K. L. Brown, Rev. Sci. Instr. 27, 959 (1956).

22. G. W. Tautfest and H. R. Fechter, Rev. Sci. Instr. 26, 229 (1955).

23. W. C. Barber and V. J. Vanhuyse, Nuclear Phys. 16, 381 (1960).

24. G. Peterson (private communication).

25. A. O. Hanson, L. H. Lanzl, E. M. Lyman, and M. B. Scott, Phys. Rev. 84, 634 (1951).

26. D. L. Judd, Rev. Sci. Instr. 21, 213 (1950).

27. A. Whetstone and J. Halpern, Phys. Rev. 109, 2072 (1958).

28. M. Rich and R. Madey, "Range-Energy Tables", UCRL report 2301 (AEC, Technical Information Service, Oak Ridge, Tenn. - W45050, March 1954).

29. Hamilton Watch Co., Precision Metals Division, Lancaster, Pennsylvania.

30. Pilot Chemicals Inc., 36 Pleasant Street, Watertown, Massachusetts.

31. W. C. Barber and W. D. George, Phys. Rev. 116, 1551 (1960).

32. W. C. Barber, Phys. Rev. 111, 1642 (1958).

33. J. S. Blair, Phys. Rev. 75, 907 (1949).

34. M. Elaine Toms, Bibliography of Photonuclear Reactions (Naval Research Laboratory, Washington, D. C., August 1958), pp. 31 - 33.

35. K. N. Geller, Phys. Rev. 120, 2147 (1960).

36. C. Milone and A. Rubbino, Nuovo cimento 13, 1035 (1959).

37. W. E. Stephens, A. K. Mann, B. J. Patton, and E. J. Winhold, Phys. Rev. 98, 839 (1955).

38. F. Ajzenberg-Selove and T. Lauritsen, Ann. Rev. Nuclear Sci. 10, 419 (1960).

39. E. G. Fuller and Evans Hayward in Proceedings of the International Conference on Nuclear Structure, Kingston, Canada, edited by D. A. Bromley and E. W. Vogt (University of Toronto Press, Toronto, Canada, (1960), pp. 711 - 712.

40. N. W. Tanner, G. C. Thomas, and W. E. Meyerhof, Nuovo cimento 14, 257 (1959).

41. S. G. Cohen, P. S. Fisher, and E. K. Warburton, Phys. Rev. Letters 3, 433 (1959).

42. H. Fuchs and C. Salander in Contributions to the Karlsruhe Conference 1960 (Erstes Physikalisches Institut der Universität Heidelberg, Heidelberg, 1961), p. A-11.

43. J. H. Carver and K. H. Lokan, Australian J. Phys. 30, 312 (1957).

44. B. Forkman and I. Wahlström, Arkiv Fysik 18, 339 (1960).

45. J. G. V. Taylor, L. B. Robinson, and R. N. H. Haslam, Can. J. Phys. 32, 238 (1954).

46. J. Goldemberg and L. Katz, Phys. Rev. 95, 471 (1954).

47. W. B. Lasich, E. G. Muirhead, and G. G. Shute, Australian J. Phys. 8, 456 (1955).

48. G. A. Ferguson, J. Halpern, R. Nathans, and P. F. Yergin, Phys. Rev. 95, 776 (1954).

49. J. R. Atkinson, I. Crawford, D. R. O. Morrison, I. Preston, and I. F. Wright, Physica 22, 1145A (1956).

50. A. P. Komar and I. P. Iavor, J. Exptl. Theoret. Phys. (U.S.S.R.) 32, 614L (1957).

51. J. B. Warren and H. J. Hay, Bull. Am. Phys. Soc. No. 2, 178A (1957).

52. D. S. Gemmell, A. H. Morton, and W. I. B. Smith, Nuclear Phys. 10, 45 (1959).

53. G. K. Farney, H. H. Givin, B. D. Kern, and T. M. Hahn, Phys. Rev. 97, 720 (1955).

54. I. P. Iavor, Soviet Phys. – JETP 7, 983 (1958).

55. V. Emma, C. Milone, R. Rinzivillo, Nuovo cimento 14, 62 (1959).

56. A. S. Penfold and E. L. Garwin, Phys. Rev. 114, 1139 (1959).

57. F. Gudden and J. Eichler, Z. Physik 150, 1139 (1959).

58. P. Erdös, P. Scherrer, and P. Stoll, Helv. Phys. Acta 26, 207 (1953).

59. L. Cohen, A. K. Mann, B. J. Patton, K. Reibel, W. E. Stephens and E. J. Winhold, Phys. Rev. 104, 108 (1956).

60. V. J. Vanhuyse and W. C. Barber, Nuclear Phys. 26, 233 (1961).

61. S. Penner and J. E. Leiss, Phys. Rev. 114, 1101 (1959).

62. D. S. Gemmell (private communication).

63. H. E. Gove, A. E. Litherland, and R. Batchelor, "Proton Capture Gamma Rays in the Giant Resonance Region in Light Nuclei", Atomic Energy of Canada, Ltd. preprint, 1961.

64. B. C. Diven and G. M. Almy, Phys. Rev. 80, 407 (1950).

65. W. K. Dawson, Can. J. Phys. 34, 1480 (1956).

66. J. Halpern and A. K. Mann, Phys. Rev. 83, 370 (1951).

67. J. E. E. Baglin, M. W. Thomas, and B. M. Spicer, Nuclear Phys. 22, 207 (1961).

68. K. L. Brown, Rev. Sci. Instr. 27, 959 (1956).

69. C. Milone, S. Milone-Tamburino, R. Rinzivillo, A. Rubbino, and C. Tribuno, Nuovo cimento 7, 729 (1958).

70. P. Brix and E. R. Mascke, Z. Physik 155, 109 (1959).

71. E. D. Courant, Phys. Rev. 82, 703 (1951).

72. J. Eichler and H. A. Weidenmüller, Z. Physik 152, 261 (1958).

73. H. E. Gove (private communication).

74. D. Isabelle (private communication).

75. G. E. Brown and L. S. Levinger, Proc. Phys. Soc. (London) 71, 733 (1958).

76. M. M. Hoffman and A. G. W. Cameron, Phys. Rev. 92, 1184 (1953).

APPENDIX I.

CALCULATION OF THE EFFECTIVE GAS-TARGET THICKNESS AS A FUNCTION OF SPECTROMETER ANGLE

The effective thickness of the gas target is equal to the spectrometer lateral efficiency function $E(x,y)$ integrated over the area defined by the gas-chamber geometry and the primary electron beam and divided by the width of the primary electron beam. The calculation is conveniently divided up into two regions for which $R \tan \theta_q - \delta_- \sec \theta_q$ is smaller or greater than W, where W is the primary electron beam half-width, R the target radius, and θ_q is the angle between the spectrometer and the primary electron beam as defined previously; other restrictions on the parameters are self-evident. The target geometries at 20°, 48°, and 76° are shown in Fig. AI-1a, b, and c. The gas chamber was axially symmetric to an excellent approximation, and therefore we assumed equal target thickness for equivalent angles in the foreward and backward hemispheres.

For $R \tan \theta_q - \delta_- \sec \theta_q < W$, the effective target thickness

$$\frac{1}{2W} \int E(x',y')dA' = \frac{1}{W}\left(\int_0^{x'_+} dA' + \int_{\delta_-}^{x'_+} \frac{\delta_- - x'}{\delta_+ - \delta_-} dA' \right)$$

$$= \frac{R^2}{2W}\left\{ 2\left(\sin^{-1}\frac{W}{R} + \frac{W}{R}\left[1 - \left(\frac{W}{R}\right)^2 \right]^{1/2} \right) + \frac{\delta_-}{\delta_+ - \delta_-}\left(\sin^{-1}\frac{x_+}{R} - \sin^{-1}\frac{\delta_-}{R} \right) \right\}$$

$$+\frac{R}{3(\delta_+ - \delta_-)}\left\{\left[1-\left(\frac{x_+}{R}\right)^2\right]^{1/2}\left(2-2\frac{x_+^2}{R^2}-\frac{\delta_- x_+}{R^2}\right)\right.$$

$$-\left[1-\left(\frac{x_-}{R}\right)^2\right]^{1/2}\left(2+\frac{\delta_-^2}{R^2}\right)$$

$$\left.+\csc\theta_q\frac{(x_+-\delta_-)^2}{R^3}\left[(\delta_-+2x_+)\cos\theta_q-\frac{3W}{R}\right]\right\}\Bigg\}. \quad \text{(AI-1)}$$

For $R\tan\theta_q - \delta_- \sec\theta_q > W$, the effective target thickness

$$\frac{1}{2W}\int E(x',y')dA' = \frac{1}{W}\left(\int_0^{\delta_-} dA' + \int_{\delta_-}^{x_-}\frac{\delta_+ - x'}{\delta_+ - \delta_-}dA' + \int_{x_-}^{x_+}\frac{\delta_+ - x'}{\delta_+ - \delta_-}dA'\right)$$

$$= \frac{R^2}{2W}\left\{\frac{4W}{R}\csc\theta_q\left[\frac{x_-}{R}-\frac{1}{2}\frac{(x_- - \delta_-)^2}{R(\delta_+ - \delta_-)}\right]\right.$$

$$+\frac{\delta_+}{\delta_+ - \delta_-}\left(\sin^{-1}\frac{x_+}{R}-\sin^{-1}\frac{x_-}{R}\right)$$

$$+\frac{R}{3(\delta_+ - \delta_-)}\left\{\left[1-\left(\frac{x_+}{R}\right)^2\right]^{1/2}\left(2-2\frac{x_+^2}{R^2}+3\frac{\delta_+ x_+}{R^2}\right)\right.$$

$$-1\left[1-\left(\frac{x_-}{R}\right)^2\right]^{1/2}\left(2-2\frac{x_-^2}{R^2}+3\frac{\delta_+ x_-}{R^2}\right)$$

$$\left.+\csc\theta_q\frac{(x_+ - x_-)^2}{R^3}\left\{3(2\delta_+ - x_+ - x_-)\right.\right.$$

$$- [3\delta_+(x_+ + x_-) - 2(x_+^2 + x_+x_- + x_-^2)]\cos\theta_q \Big\} \Big\} \Big\} . \quad \text{(AI-2)}$$

In the case where $x_+ = \delta_+$, the above expression becomes

$$\frac{1}{2W}\int E(x',y')dA' = \frac{R^2}{2W}\left\{\frac{4W}{R}\csc\theta_q\left[\frac{x_-}{R} - \frac{1}{2}\frac{(x_- - \delta_-)^2}{R(\delta_+ - \delta_-)}\right]\right.$$

$$+ \frac{\delta_+}{\delta_+ - \delta_-}\left(\sin^{-1}\frac{x_+}{R} - \sin^{-1}\frac{x_-}{R}\right)$$

$$+ \frac{R}{3(\delta_+ - \delta_-)}\left\{\left[1 - \left(\frac{\delta_+}{R}\right)^2\right]^{1/2}\left(2 + \frac{\delta_+^2}{R^2}\right)\right.$$

$$- \left[1 - \left(\frac{x_-}{R}\right)^2\right]^{1/2}\left(2 - 2\frac{x_-^2}{R^2} + 3\frac{\delta_+x_-}{R^2}\right)$$

$$\left.\left. + \csc\theta_q\frac{(\delta_+ - x_-)^2}{R^3}[3W - (\delta_+ + 2x_-)\cos\theta_q]\right\}\right\} . \quad \text{(AI-3)}$$

For $x_- = \delta_+ + \delta_-$, the effective target thickness is independent of W and

$$\frac{1}{2W}\int E(x',y')dA' = R\csc\theta_q(\delta_+ + \delta_-) , \quad \text{(AI-4)}$$

where $x_\pm$ is the smaller of $\pm W\cos\theta_q + [R^2 - W^2]^{1/2}\sin\theta_q$ or δ_+ .

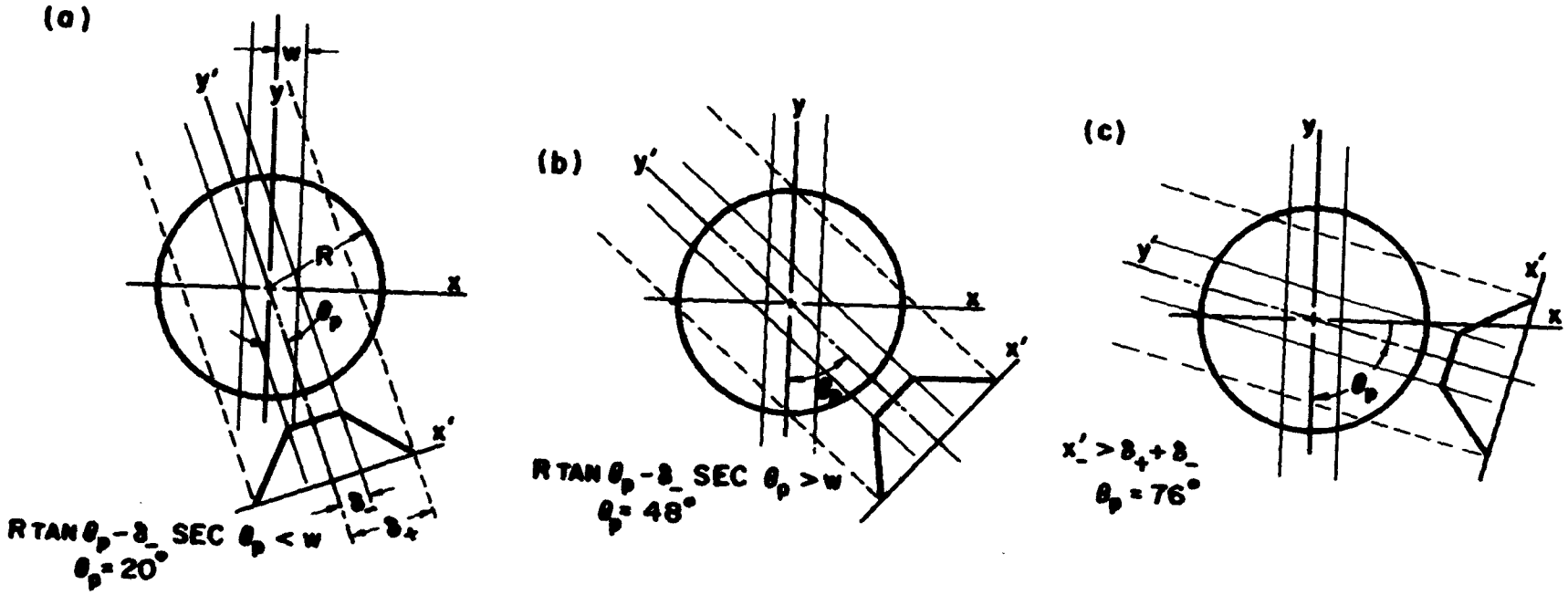

FIGURE AI-1

Gas target geometries at 20°, 48°, and 76°.

APPENDIX II

THE RELATIONSHIP BETWEEN THE LABORATORY AND THE CENTER-OF-MASS SYSTEMS FOR THE (γ,p) REACTION

The cross section measured in the laboratory coordinate system is usually expressed in the center-of-mass system to facilitate comparison with theoretical predictions. The cross sections are related by the following expressions

$$\left[\frac{d\sigma(\theta_o)}{d\Omega}\right]_o = \left[\frac{d\sigma(\theta_{lab})}{d\Omega}\right]_{lab} \frac{(1 - \beta_{cm}^2)(1 + \Gamma \cos\theta_o)}{[\Gamma^2 + 2\Gamma \cos\theta_o + 1 - \beta_{cm}^2 \sin^2\theta_o]^{3/2}} \quad ,(AII\text{-}1)$$

where $\Gamma = \beta_{cm} / (E_o/P_o)$ is the ratio of the center-of-mass velocity to the proton velocity in the center-of-mass system, and the subscript o refers to center-of-mass quantities.

Explicitly,

$$\beta_{cm} = \frac{k}{M_A + k} \quad , \qquad (AII\text{-}2)$$

$$E_o = \frac{1}{[1 + (2k/M_A)]^{1/2}}[k + M_p - Q(M_A - M_p)/M_A + \tfrac{1}{2}(Q^2/M_A)] \quad , \qquad (AII\text{-}3)$$

For photoprotons from the giant resonance region $Q < k \ll M_A$, and

$$\Gamma = \frac{k}{[2M_p\, A(A-1)(k-Q)]^{1/2}} \ll 1 \quad , \qquad (AII\text{-}4)$$

$$\Gamma = \frac{k}{A[2M_p\, T_p]^{1/2}} \quad \text{(for ground state transition)}$$

therefore,

$$\left[\frac{d\sigma(\theta_o)}{d\Omega}\right]_o = \left[\frac{d\sigma(\theta_{lab})}{d\Omega}\right]_{lab} (1 - 2\Gamma \cos\theta_o) \quad , \qquad (AII\text{-}5)$$

Table AII-I summarizes the relationships between $\left[\frac{d\sigma(\theta_o)}{d\Omega}\right]_o$ and $\left[\frac{d\sigma(\theta_{lab})}{d\Omega}\right]_{lab}$ for alternate forms of the angular distributions. Use of the relationships

$$\sin \theta_{lab} = \sin \theta_o \sum_{\ell=0}^{\infty} (-\Gamma)^{\ell} P_{\ell}(\cos \theta_o)$$

and

$$\cos \theta_{lab} = \sum_{\ell=0}^{\infty} (-\Gamma)^{\ell-1}\left[\frac{\ell}{2\ell - 1} - \Gamma^2 \frac{\ell}{2\ell + 3}\right]P_{\ell}(\cos \theta_o) ,$$

valid for energies where the relativistic contraction of angles may be neglected ($\beta_{cm} \ll 1$), and

$$P_{\ell}(\cos \theta_{lab}) = P_{\ell}(\cos \theta_o) + \frac{\ell(\ell + 1)}{2\ell + 1} \Gamma[P_{\ell-1}(\cos \theta_o) - P_{\ell+1}(\cos \theta_o)] ,$$

valid for $\beta_{cm} \ll 1$, $\Gamma \ll 1$, has been made.

TABLE AII-I. Relationship between the laboratory and center-of-mass differential cross section for $\Gamma \ll 1$.

Laboratory System	Center-of-Mass System
$\frac{d\sigma(\theta_{lab})}{d\Omega}_{lab}$	$\frac{d(\theta_o)}{d\Omega}_o$
$\sum_{\ell=0}^{N} C_\ell \cos^\ell \theta_{lab}$	$\sum_{\ell=0}^{N} [C_\ell + \Gamma(\ell+1)(C_{\ell+1} - C_{\ell-1})] \cos^\ell \theta_o$
$\sum_{\ell=0}^{N} C'_\ell P_\ell(\cos\theta_{lab})$	$\sum_{\ell=0}^{N} \left[C'_\ell + \Gamma\ell(\ell+1)\left(\frac{C'_{\ell+1}}{2\ell+3} - \frac{C'_{\ell-1}}{2\ell-1}\right) P_\ell(\cos\theta_o)\right]$
$A + B\cos\theta + C\sin^2\theta + D\sin^2\theta\cos\theta$	$A - \Gamma(2B+5D) + (B - 2\Gamma A)\cos\theta_o$ $+ [C + 3\Gamma(B+2D)]\sin^2\theta_o + (D - 4\Gamma C)\sin^2\theta_o \cos\theta_o$

DISTRIBUTION LIST

Contract N6onr-25116 (NR 022 026)

Professional

Dr. M. Pomerantz
Bartol Research Foundation
Franklin Institute
Whittier Place
Swarthmore, Pennsylvania

Professor C. D. Anderson
Norman Bridge Laboratory of Physics
California Institute of Technology
Pasadena 4, California

Professor W. A. Fowler
Kellogg Radiation Laboratory
California Institute of Technology
Pasadena 4, California

Professor R. B. Brode
Department of Physics
University of California
Berkeley 4, California

Professor J. R. Richardson
Department of Physics
University of California
Los Angeles 24, California

Professor Mark Inghram
Department of Physics
University of Chicago
5801 Ellis Avenue
Chicago 37, Illinois

Professor H. L. Anderson
Department of Physics
University of Chicago
5801 Ellis Avenue
Chicago 37, Illinois

Professor J. Rainwater
Columbia University
Nevis Cyclotron Laboratories
P. O. Box 117
Irvington-on-Hudson, New York

Professor R. R. Wilson
Laboratory of Nuclear Studies
Cornell University
Ithaca, New York

Professor Hans Bethe
Laboratory of Nuclear Studies
Cornell University
Ithaca, New York

Professor M. M. Block
Department of Physics
Duke University
Durham, North Carolina

Professor R. W. Hickman
Department of Physics
Harvard University
Cambridge, Massachusetts

Professor F. Seitz
Department of Physics
University of Illinois
Urbana, Illinois

Professor A. G. C. Mitchell
Department of Physics
University of Indiana
Bloomington, Indiana

Professor J. A. Van Allen
Department of Physics
State University of Iowa
Iowa City, Iowa

Dr. P. T. Demos
Laboratory for Nuclear Science
Massachusetts Institute of Technology
Cambridge, Massachusetts

Professor W. E. Hazen
Department of Physics
University of Michigan
Ann Arbor, Michigan

Professor A. O. C. Nier
Depatment of Physics
University of Minnesota
Minneapolis 14, Minnesota

Professor E. P. Ney
Department of Physics
University of Minnesota
Minneapolis 14, Minnesota

Dr. Ugo Fano
National Bureau of Standards
Commerce Department
Washington 25, D. C.

Professor S. A. Korff
Department of Physics
New York University
University Heights
New York 53, New York

Professor B. Waldman
Nuclear Physics Laboratory
University of Notre Dame
Notre Dame, Indiana

Professor W. E. Stephens
Department of Physics
University of Pennsylvania
Philadelphia 4, Pennsylvania

Professor A. J. Allen
Department of Physics
University of Pittsburgh
Pittsburgh 13, Pennsylvania

Professor W. E. Meyerhof
Department of Physics
Stanford University
Stanford, California

Professor E. M. Barth
Syracuse University Research Institute
Syracuse 10, New York

Professor W. K. H. Panofsky
Department of Physics
Stanford University
Stanford, California

Professor R. D. Sard
Department of Physics
Washington University
St. Louis 5, Missouri

Professor G. Reynolds
Department of Physics
Princeton University
Princeton, New Jersey

Professor S. Neddermeyer
Department of Physics
Princeton University
Princeton, New Jersey

Professor L. W. Jones
Department of Physics
University of Michigan
Ann Arbor, Michigan

Professor C. L. Cowan
Physics Department
Catholic University
Washington 17, D. C.

Professor K. Wildermuth
Department of Physics
Florida State University
Tallahassee, Florida

Professor F. E. Steigert
Sloane Physics Laboratory
Yale University
New Haven 11, Connecticut

Physics Library
c/o N. M. Hintz
University of Minnesota
Minneapolis 14, Minnesota

Department of Physics
Brookhaven National Laboratory
Upton, L. I., New York
Attn: Alice Whittemore

Governmental

[5] Armed Services Technical Information Agency
Arlington Hall Station
Arlington 12, Virginia

[2] Chief of Naval Research
Attn: Nuclear Physics Branch
Department of the Navy
Washington 25, D. C.

[6] Director, Naval Research Laboratory
Attn: Technical Information Officer
Washington 25, D. C.

Commanding Officer
Office of Naval Research Branch Office
John Crerar Library Building
86 East Randolph Street
Chicago 1, Illinois

Commanding Officer
Office of Naval Research Branch Office
1030 East Green Street
Pasadena 1, California

Office of Technical Services
Department of Commerce
Washington 25, D. C.

U. S. Atomic Energy Commission
Patent Branch
Washington 25, D. C.

U. S. Atomic Energy Commission
New York Operations Office
Attn: Records Management Branch
70 Columbus Avenue
New York 23, New York

Chief, Physics Branch
U. S. Atomic Energy Commission
Washington 25, D. C.

U. S. Atomic Energy Commission
Technical Information Service Extension
Attn: Document Processing Branch
P. O. Box 62
Oak Ridge, Tennessee

Commander
Air Force Office of Scientific Research
ARDC, Attn: SRYM
Washington 25, D. C.

[10] Commanding Officer
Office of Naval Research Branch Office
Navy No. 100
Fleet Post Office
New York, New York

Governmental (continued)

Chief of Research and Development
Department of the Army
Washington 25, D. C.

Commanding Officer
Office of Naval Research Branch Office
1000 Geary Street
San Francisco 9, California

Librarian
U. S. Naval Postgraduate School
Monterey, California

Chief, Bureau of Ships
Attn: Code 1500
Department of the Navy
Washington 25, D. C.

Chief, Bureau of Ships
Attn: Code 300
Department of the Navy
Washington 25, D. C.

Chief, Bureau of Naval Weapons
Attn: RRSY-3
Department of the Navy
Washington 25, D. C.

Commander, U. S. Naval Ordnance Test Station
Code 753
China Lake, California

Office of Ordnance Research
U. S. Army
Attn: Physical Sciences Division
Box CM, Duke Station
Durham, North Carolina

Brookhaven National Laboratory
Research Library
Attn: Reference Section
Upton, Long Island, New York

Ames Laboratory
Iowa State College
P. O. Box 14-A, Station A
Ames, Iowa

Commanding Officer and Director
U. S. Naval Radiological Defense Laboratory
Attn: Library Branch, Code 3-222A
San Francisco 24, California

Superintendent, Nucleonics Division
Naval Research Laboratory
Anacostia
Washington, D. C.

Chief, Bureau of Naval Weapons
Attn: RR-12
Department of the Navy
Washington 25, D. C.

National Bureau of Standards Library
Room 301, Northwest Building
Washington 25, D. C.

Commanding General
Air Force Cambridge Research Center
Attn: CROOTR
L. C. Hanscom Field
Bedford, Massachusetts

Oak Ridge National Laboratory
Attn: Head, Physics Division
P. O. Box P
Oak Ridge, Tennessee

Exchange and Gift Division
Library of Congress
Washington 25, D. C.

Mr. J. R. King
ONR Resident Representative
Electronics Research Laboratory
Stanford University
Stanford, California

Library and Record Center
Mound Laboratory
Monsanto Chemical Company
P. O. Box 32
Miamisburg, Ohio

Argonne National Laboratory
Attn: Hoylande D. Young
9700 South Cass Avenue
Argonne, Illinois

Knolls Atomic Power Laboratory
Attn: Document Librarian
P. O. Box 1072
Schenectady, New York

Dr. Howard A. Robinson
Special Assistant to the Ambassador
American Embassy
2, Av. Gabriel
Paris VIII, France

Union Carbide Nuclear Company
P. O. Box P
K-25 Plant Records Department
Building K-1034
Oak Ridge, Tennessee

Sandia Corporation
Sandia Base
Classified Document Division
Albuquerque, New Mexico

Union Carbide Nuclear Company
Oak Ridge National Laboratory
Laboratory Records Department
P. O. Box P
Oak Ridge, Tennessee

Los Alamos Scientific Laboratory
Attn: Report Library
P. O. Box 1663
Los Alamos, New Mexico

Foreign

*Professor Denys Wilkinson
Cavendish Laboratory
Cambridge University
Free School Lane
Cambridge, England

*Dr. Herbert Uberall
Department of Theoretical Physics
University of Liverpool
Liverpool, England

*Professor F. C. Chapman
Department of Physics
University of London King's College
London, W. C. 2, England

*CERN
Scientific Information Service
Geneva 23, Switzerland
Attn: Mrs. L. Goldschmidt-Clermont

*University di Pisa
Instituto di Fisica
Pisa, Italy
Attention: M. Conversi
L. A. Radicati

*Dr. Erik Sears
Royal Institute of Technology
Stockholm, Sweden

*Professor J. L. Verhaeghe
Linear Accelerator Laboratory
University of Ghent
Coupure
Ghent, Belgium

*Dr. J. L. Delcroix
Ecole Normale Superieure
Laboratoire de Physique
24, Rue Lhomond
Paris V, France

*Dr. B. Milman
Laboratoire des Hautes Energies
B. P. No. 2
Orsay (S. et O.)
France

Library
Institute for Nuclear Study
University of Tokyo
Tanashi-Machi, Kitatama-Gun
Tokyo, Japan

Professor L. Katz
Department of Physics
University of Saskatchewan
Saskatoon, Saskatchewan
Canada

*Via Officer-in-Charge
Office of Naval Research
London Branch Office
Navy No. 100
Fleet Post Office
New York, New York